2024-09-17

# Mechanisms of Mycophenolic Acid-Induced Gastrointestinal Toxicity and Potential Therapeutic Interventions in Primary Mouse Colonic Organoids

Mack-Bowles, Brenan

UNIVERSITY OF CALGARY

# Mechanisms of Mycophenolic Acid-Induced Gastrointestinal Toxicity and Potential Therapeutic Interventions in Primary Mouse Colonic Organoids

by

Brenan Mack-Bowles

A THESIS

SUBMITTED TO THE FACULTY OF GRADUATE STUDIES

IN PARTIAL FULFILMENT OF THE REQUIREMENTS FOR THE

DEGREE OF MASTER OF SCIENCE

GRADUATE PROGRAM IN MEDICAL SCIENCE

CALGARY, ALBERTA

SEPTEMBER, 2024

# Abstract

Mycophenolate Mofetil (MMF) is a commonly prescribed immunosuppressant that demonstrates important clinical relevance. However, MMF therapy is linked to frequent gastrointestinal (GI) side effects that limit its use. Little is known about the mechanisms underlying MMF-induced GI injury. Using a primary mouse colon organoid model, we have found that mycophenolic acid (MPA), the pharmacologically active metabolite of MMF, significantly alters intestinal barrier function and permeability through modulation of tight junctions. RNA sequencing revealed that MPA significantly disrupted pathways related to cell cycle regulation, DNA replication, cytoskeleton dynamics, and suppression of senescence. MPA was observed to significantly reduce cellular proliferation, which was ameliorated through guanosine supplementation. Addition of exogenous guanosine was also observed to significantly restore barrier function back to control levels. The guanosine studies presented in this thesis suggest MPA's inhibition of nucleotide metabolism is not selective for lymphocytes but is broader than originally described. This work represents one of the first investigations of MPA using a colon organoid model, providing critical insights into the intracellular mechanisms of MPA-induced GI toxicity.

***Keywords**:* Mycophenolate mofetil, Mycophenolic acid, Immunosuppressive therapy, *in vitro* modelling, Cell culture, Organoids, Colonoid culture, Colonoid monolayer culture, Gastrointestinal toxicity, Intestinal barrier function, Transepithelial resistance, FITC-dextran permeability, Tight junctions, Total RNA-sequencing, Differential gene expression, Ingenuity Pathway Analysis, Guanosine supplementation

# Preface

This thesis is original, unpublished, work by the author, Brenan Mack-Bowles.

# Acknowledgements

I would like to express sincere gratitude for my supervisor, Dr. Steven Greenway, who offered his expertise and guided my project to completion; his commitment to medicine inspired this research greatly. This work was further supported by the Human Organoid Innovation Hub (HOIH) in the Snyder Institute at the University of Calgary with the generous support of the Cumming Medical Research Fund and the office of the Vice President of Research. I would also like to thank Grace Baruta and Hong Zhang for their invaluable contributions and collaborations throughout my time working with the HOIH, as well as my fellow graduate lab-mates for their advice and ongoing support over the past couple years.

# Dedication

I dedicate this thesis to my mother. Her strength and resilience inspire me everyday. This work would not have been possible without her encouragement and sacrifices. This thesis is a testament to the values she has instilled in me. I also dedicate this thesis to the rest of my family and friends who have supported me during this time.

# Table of Contents

# List of Tables

# List of Figures and Illustrations

plated for expansion. Scale bars annotated in black represent a scale of 50 µm. *Created with BioRender.com*

**Figure 4.3 Bright-field microscopy images demonstrating different characteristics of colonoid culture, illustrating a range of conditions and organoid morphology.** (A) Open colonoid characteristic. (B) Closed colonoid characteristic. (C) High density organoid culture. (D) Low density organoid culture. (E) Clean culture conditions. (F) Dirty culture conditions. (G) High accumulation of cellular debris. (H) Low accumulation of cellular debris. (I) Colonoids left in depleted/low pH media for an extended period. (J) Presence of biological contaminates in colonoid culture. Each row represents a desirable or undesirable trait critical for assessing quality and determining readiness for passaging and monolayer generation. Each characteristic has two representative images to highlight variability across different passages and stages of growth. Black scale bars represent 100µm. *Created with BioRender.com*

**Figure 4.4 Digital image showing coloration changes in 3D-MCM.** Cells expel acidic waste products such as lactic acid and carbon dioxide as they metabolize nutrients in the medium. pH indicators change color corresponding to changes in the pH. When the media becomes more acidic the media transitions to a yellow color. At a neutral pH (≈ 7.4) the medium appears red/pink. Observing shifts in color was used to inform timely media changes.

**Figure 4.5 Illustration depicting the workflow for establishing 2D colonoid monolayers from 3D primary mouse colon organoids.** (A) Simplified step-by-step process of generating primary mouse colon organoid monolayers. First, 3D colonoids are grown to 4-6 days of maturity to obtain suitable organoids for subsequent digestion and crypt stem cell isolation. Once isolated, the cell suspension is pelleted, collected, and uniformly plated onto the porous membrane of trans-well inserts pre-incubated with Matrigel. Within 1-2 weeks, the isolated cells proliferate to form a confluent monolayer recapitulating the polarized physiology of the colon tissue it was derived from. (B panel 1) Representative bright-field images of 3D colonoids ready for processing into monolayers. (B panel 2) Organoids displaying early-stage trypsin digestion. (B panel 3) Organoids demonstrating late-stage trypsin digestion. (B panel 4) Bright-field image showcasing uniform plating of dissociated colonoids on the porous membrane of a trans-well insert. Black scale bars represent 50 µm. *Created with BioRender.com*

**Figure 4.6 Bright-field microscopy images exhibiting different characteristics of colonoid monolayer culture, illustrating a range of culture conditions and monolayer morphology.** (A) Freshly plated dissociated colonoids with uniform plating distribution. (B) Poorly plated monolayers, with low density of single cells. (C) Presence of 3D structures in monolayers. (D) Ideal monolayer characteristics, clean and confluent with no 3D structures present. (E) Dirty culture conditions with exogenous fibers/microplastics present. (F) High accumulation of cellular debris. (G) Poor dissociation of colonoids before monolayer plating with high prevalence of clumped cells. (H) Images illustrating the difficulty of determining confluency through bright-field microscopy. The porous membrane of trans-well inserts produces visual noise making it hard to distinguish the presence of gaps in growing monolayers. (I) Presence of biological contaminates in monolayer culture. These images display desirable and undesirable traits critical for assessing monolayer quality and determining readiness for experimentation. Each panel represents various passages and stages of growth. *Created with BioRender.com*

**Figure 4.7 Primary mouse colonoid monolayers fixed and stained for ZO-1 (green) and DAPI (blue) to visualize monolayer morphology and confluency.** (A) ZO-1 stain of a non-confluent monolayer. (B) DAPI stain of a non-confluent monolayer. (C) Channel merge of ZO-1 and DAPI in non-confluent monolayer. (D) ZO-1 stain of a confluent monolayer. (E) DAPI stain of a confluent monolayer. (F) Channel merge of ZO-1 and DAPI in a confluent monolayer. Images were processed and merged using ImageJ. White scale bars represent 100 µm. *Created with BioRender.com*

**Figure 4.8 Measurement of transepithelial resistance in primary mouse colonoid monolayers exposed to increasing concentrations of MPA and a vehicle control (methanol) over a 24-hour period.** The y-axis corresponds to the mean resistance change (%) compared to baseline measurements taken at time 0. Values represent mean ± SEM. Data passed Shapiro-Wilk test of normality and was assessed using a one-way ANOVA followed by Tukey's post-hoc test. All MPA treatments induced significant changes in monolayer resistance (**** $P < 0.0001$) compared to the control ($n = 3$).

**Figure 4.9 Primary mouse colonoid monolayers fixed and stained for ZO-1 (yellow) and DAPI (blue) to visualize monolayer morphology and confluency after treatment with MPA and a vehicle control over a 24-hour period.** Each treatment condition includes two representative images to highlight variability noted within each treatment. Images were processed and merged using ImageJ. White scale bars represent 50 µm. *Created with BioRender.com*

**Figure 4.10 Measurement of transepithelial resistance in primary mouse colonoid monolayers exposed to MPA and a vehicle control (methanol) over a 24-hour period.** The y-axis corresponds to the mean percentage change in resistance compared to baseline measurements at time 0. Values represent mean ± SEM. Data passed Shapiro-Wilk test of normality and was assessed using a one-way ANOVA followed by Tukey's post-hoc test. All MPA treatments induced significant changes in monolayer resistance (**** $P < 0.0001$) compared to the control ($n = 15$).

**Figure 4.11 4 kDa FITC-Dextran permeability assay conducted on primary mouse colonoid monolayers exposed to physiological concentrations of MPA and a vehicle control (methanol) over 24 hours.** The y-axis represents monolayer permeability which is determined by the ratio of basolateral to apical relative fluorescent units (basolateral/apical RFUs). Values are presented as mean RFUs ± SEM. Data passed Shapiro-Wilk test of normality and was assessed using a one-way ANOVA followed by Tukey's post-hoc test. A scatterplot is superimposed to highlight individual permeability values. Only the 31.22 µM MPA treatment demonstrated significance (* $P = 0.0172$) compared to the control ($n = 3$).

**Figure 4.12 Concentration changes in 24 different cytokines and chemokines in colonoid monolayers treated with physiological concentrations of and a vehicle control (methanol) after 24 hours.** Each graph represents the mean observed concentration ± SEM ($n = 6$) of the labelled cytokines/chemokines in control and MPA-treated conditions. Concentrations are

expressed in pg/mL. Significant differences between vehicle control and MPA exposed groups were assessed using a non-parametric Kruskal-Wallis test, followed by Dunn's multiple comparisons test. No significant differences were observed ($P > 0.05$).

**Figure 4.13 FastQC report plot showing quality score distribution across all sequenced reads.** The x-axis represents the mean sequence quality (Phred score) ranging from 2 to 37, and the y-axis represents the number of sequences at each quality score. Scores above 30 indicate high-quality reads. The sharp increase past 30 indicates that the data meets quality expectations for downstream analyses.

**Figure 4.14 Graphical representations of differential expression analysis conducted through Rstudio.** (A) Expression profile heatmap illustrating expression differences across different MPA treatment groups (7.81, 15.61, 31.22 µM MPA) and a vehicle control. Each row and column represent the various treatment conditions. The heatmap represents rlog-transformed normalized count values (rlog values). Rlog values indicate the degree of transcript expression, with higher values corresponding to greater differences relative to the conditions being compared. An rlog value of 0 is represented in blue, indicating no difference between the groups being compared. Fading of the blue intensity corresponds to higher rlog values (greater difference). (B) Volcano plot demonstrating the relationship between Log2 fold change (x-axis) and statistical significance (y-axis) of gene expression differences between MPA treatment and vehicle control. The volcano plot does not distinguish between different MPA concentrations and is an averaged representation of treatment vs control.

**Figure 4.15 Pathway analysis of MPA-induced gene expression changes.** (A) Canonical pathway bubble chart revealing pathways significantly affected by MPA treatment. Each bubble corresponds to a distinct pathway, with the size of the bubble representing the number of genes affected in that pathway. The color indicates z-score, with blue representing a negative score (downregulated), orange representing a positive score (upregulated), and grey representing no activity pattern. The x-axis corresponds to the -log(p-value), which indicates significance of the pathway enrichment, with larger values suggesting higher significance. The y-axis categorizes each pathway by their biological function. (B) Overlapping pathway network map displaying the connections between the significantly affected pathways from panel A. Each node represents a pathway, with lines connecting nodes signifying shared genes or functional relationships.

**Figure 4.16 Graphical summary of the sequencing dataset generated by IPA.** The diagram illustrates the complex web of molecular networks and pathways affected by MPA treatment in primary mouse colonoid monolayers. Each node represents a specific function (octagon), transcriptional regulator (oval), disease (plus sign) or other (circle). Blue lines indicate inhibition and orange lines indicate activation, with solid lines representing direct interactions and dashed lines representing indirect interactions. The color of each node reflects the activation (orange) or inhibition (blue) of that specific node.

**Figure 4.17 Transepithelial resistance of primary mouse colonoid monolayers after 24 hours of exposure to 4 different treatments: Vehicle control (methanol), 7.81 µM MPA, 7.81 µM MPA + 1 mM Guanosine, and 1 mM Guanosine.** The y-axis corresponds to the mean percent change in TER compared to baseline measurements taken at time 0. Values represent mean ± SEM. Data passed Shapiro-Wilk test of normality and was assessed using a one-way

ANOVA followed by Tukey's post-hoc test. Co-treatment with guanosine significantly restored TER (*** P = 0.0002, ** P = 0.0032) when compared to 7.81 µM MPA treatment (n = 9).

**Figure 4.18 Assessment of 3D colonoid growth after 48 hours of exposure to 4 different treatments: Vehicle control, 7.81 µM MPA, 7.81 µM MPA + 1 mM guanosine, and 1 mM guanosine.** (A) Time-lapse bright-field microscopy imaging of colonoid cultures over a 48-hour period. The first three rows depict colonoid growth at different time points (0 hours, 24 hours, 48 hours). The final row consists of representative images from CellProfiler software analysis. Bright-field microscopy images taken at the 48-hour timepoint were processed through CellProfiler for quantification of organoid growth and count. (B) Graphical representation of the CellProfiler analysis, illustrating the average cross-sectional area of the organoids. The average cross-sectional area was calculated for each treatment condition at the 48-hour time point to evaluate changes in growth. (C) Number of organoids detected by CellProfiler for each treatment at the 48-hour time point. Data was assessed using a Kruskal Wallis test followed by Dunn's post hoc test. Values are presented as means ± SEM. (**** P < 0.0001). *Created with BioRender.com*

# List of Symbols, Abbreviations, and Nomenclature

| Symbol | Definition |
|---|---|
| 2D | Two-dimensional |
| 2D-MCM | 2D Mouse Complete Media |
| 3D | Three-dimensional |
| 3D-MCM | 3D Mouse Complete Media |
| ABCC2 | ATP-binding cassette subfamily C member 2 |
| AcMPAG | Acyl-mycophenolic acid β-D-glucuronide |
| ADF | Advanced DMEM |
| ANOVA | Analysis of Variance |
| BSA | Bovine serum albumin |
| Caco-2 | Human colon adenocarcinoma |
| CHGI | Centre for Health Genomics and Information |
| DEGs | Differentially expressed genes |
| EC-MPS | Enteric-coated mycophenolate sodium |
| EGF | Epidermal growth factor |
| FBS | Fetal bovine serum |
| GA | Glucuronic acid |
| G-CSF | Granulocyte colony stimulating factor |
| GI | Gastrointestinal |
| GUS | β-Glucuronidase |
| HOIH | Human Organoid Innovation Hub |
| HIEC-6 | Human intestinal epithelial cells |
| IL-15 | Interleukin-15 |
| IMPDH | Inosine-5′-monophosphate dehydrogenase |
| IPA | Ingenuity Pathway Analysis |
| LIF | Leukemia inhibitory factor |
| MLCK | Myosin light-chain kinase |
| MMF | Mycophenolate mofetil |
| MIP-2 | Macrophage inflammatory protein-2 |
| MPA | Mycophenolic acid |
| NAC | N-acetylcysteine |
| PFA | Paraformaldehyde |
| PBS | Phosphate buffered saline |
| RFUs | Relative fluorescent units |
| RT | Room temperature |
| SEM | Standard error of the mean |
| TDM | Therapeutic drug monitoring |
| TER | Transepithelial resistance |
| TNFα | Tumor necrosis factor alpha |
| UGT | Uridine diphosphate glucuronosyltransferase |

# 1.1 INTRODUCTION

## 1.2 Immunosuppressive Therapy

The immune system consists of two main components: The innate immune system and the adaptive immune system. These components interact with each other through various cell types, utilizing signaling molecules such as cytokines and chemokines to mediate a range of extracellular and paracrine effects. While fundamentally protective, the immune system can exhibit maladaptive responses that contradict its intended purpose[2]. In recent years, there has been extensive investigation into these complex processes, significantly improving our understanding of their mechanisms[3]. For instance, research has identified B cell antibody production, and the activation and proliferation of T cells as key facilitators of allograft rejection[4,5]. These complex immunological processes involving B and T lymphocytes can lead to detrimental outcomes for transplant patients, such as antibody-dependent cellular cytotoxicity and chronic tissue rejection[6].

Immunosuppressants are a class of medications that function to decrease or significantly inhibit the strength of immunological processes within the body. Clinically used immunosuppressive drugs target distinct stages in signaling cascades, limiting the immune response at intracellular and extracellular levels[3]. Immunosuppressive therapy refers to the utilization of these drugs across various medical fields to manage conditions involving pathological immune system activation, such as autoimmune diseases, and to prevent transplant rejection in solid organ transplantation[7]. However, immunosuppressive drugs are associated with adverse side effects including, increased risk of infections, increased risk of malignancy, cardiovascular complications, gastrointestinal (GI) issues, and nephrotoxicity[8–11]. These adverse

side effects may be further influenced by underlying disease, host factors, and concurrent treatments[7]. Each immunosuppressive drug has its own intrinsic toxicity and underlying side effects commonly coinciding with its main therapeutic mechanism of action or through secondary off-target interactions[3].

While immunosuppression is critical for prevention of organ rejection and managing autoimmune disorders, numerous adverse side effects can limit their use. However, personalization of immunosuppressant treatment based on an individual's different contexts – diet, lifestyle, and genetic characteristics – represents a promising approach to mitigating the risks associated with immunosuppressant drugs[12].

## 1.3 Mycophenolate Mofetil

### 1.3.1 Therapeutic Uses and Mechanisms of Immunosuppression

Transplantation is a life-saving therapy for thousands of critically ill patients, however, the practice encounters limitations due to activation of the recipient's immune system. Immune-mediated rejection damages transplanted cells, tissues, and organs, leading to severe complications, including death[13]. Immune-mediated injury is also responsible for autoimmune diseases, a diverse group of illnesses that affect around 50 million North Americans[14]. To prevent damage facilitated by the immune system, potent immunosuppressive drugs, such as Mycophenolate Mofetil (MMF), play a critical role.

Commonly prescribed, MMF is an effective and relatively safe medication, particularly for those with compromised renal function[15]. MMF has important advantages over other immunosuppressants, commonly attributed to its mechanism of inhibition. MMF is a pharmacologically inactive medication, commonly referred to as a prodrug. After consumption

MMF is metabolically hydrolyzed into an active compound called mycophenolic acid (MPA). The active component, MPA, operates primarily by inhibiting the enzyme inosine monophosphate dehydrogenase (IMPDH). IMPDH is crucial for the *de novo* synthesis of guanosine monophosphate – an essential precursor for purine biosynthesis (Figure 1.1). This mechanism of inhibition is particularly impactful on B and T lymphocytes, which rely almost exclusively on the de novo pathway for purine synthesis[16] (Figure 1.1). It is suggested that through this mechanism MPA selectively, and effectively suppresses B and T lymphocyte proliferation and function[17,18]. Unlike other immunosuppressant such as cyclosporine and tacrolimus, MMF does not induce nephrotoxicity, or elevate blood pressure, cholesterol, or triglyceride levels[17]. The distinct process through which MMF elicits its effects contributes to the drug's utility in patients who may be resistant or intolerant to other immunosuppressants. Moreover, MMF has been shown to exert anti-inflammatory actions by inhibiting glycosylation and expression of adhesion molecules[17].

The immunosuppressive properties of MPA makes MMF an effective agent in preventing allograft rejection and treating autoimmune disorders. However, MMF does not escape the risks associated with immunosuppressive therapy. Similar to other immunosuppressants, MMF presents a profile of its own adverse side effects, which can ultimately lead to dosage reduction, drug discontinuation, and decreased patient quality of life[19].

### 1.3.2 Gastrointestinal Toxicity

MMF demonstrates clinical importance, but toxic side effects often limit its use and can decrease patient quality of life. The prevalence of GI toxicity associated with MMF is a significant concern. For example, while MMF is known to cause a range of side effects, GI complications

are seen in approximately 45% of patients[20]. Diarrhea is particularly common, affecting up to 51% of patients[21,22]. Other GI complications include nausea (29%), constipation (38%), vomiting (23%) and colitis (9%)[22]. Clinically, GI toxicity has been noted in different areas of the GI tract, as evidenced by villous atrophy in the duodenum and erosive enterocolitis throughout the intestines, presenting analogously to that of Crohn's disease[23,24]. According to available data, the severity of GI toxicity appears to be influenced partly by dosage, necessitating adjustment to treatment plans and prompting clinicians to consider dosage reduction and even discontinuation of the drug[11,12]. Dosage changes can compromise graft protection and long-term graft survival, potentially leading to fatal outcomes[25]. The mechanisms behind MMF toxicity is not fully understood; however, previous work has implicated alterations in gut microbiota and increased bacterial β-glucuronidase (GUS) activity, with findings suggesting that an intact microbiome is necessary for MMF-induced GI toxicity[26,27].

Given the complications associated with MMF therapy, why is there not more attention on innovating an alternative with better tolerability? In short, the process of developing a new medication is a lengthy and arduous journey. Encompassing everything from basic research to lengthy human clinical trials and regulatory clearance, it takes an average of 10 to 15 years and hundreds of millions of dollars to bring a new drug into the market[28]. Drug discovery and development is largely acknowledged as one of the greatest hurdles in the biomedical field[28]. Due to the urgent needs of patients, and the challenges of bringing a new drug to market, understanding and improving the shortcomings of presently available drugs represents a critical avenue of modern research. Given the extensive process of developing new drugs and the current clinical importance of MMF, it is imperative that further research into MMF-induced GI toxicity is conducted to further improve patient tolerability and quality of life.

### 1.3.3 Mechanisms of Gastrointestinal Toxicity

The mechanisms underlying MMF-induced gastrointestinal toxicity are not fully elucidated, but recent studies have highlighted new insights into the basis for toxicity. Currently, MPA, the active metabolite of MMF, is the most widely discussed culprit for induction of GI injury. Previously, it was widely suggested that systemic MPA exposure was a determinant of GI toxicity[29]. However, recent literature indicates that local exposure to MPA may be more relevant to GI toxicity than systemic exposure[29]. Fortunately, the primary metabolic pathway for MMF has been comprehensively characterized, thus, informing possible mechanisms of GI toxicity.

Literature has shown the main metabolic pathway for MMF involves the inactivation of the active compound MPA through glucuronidation by uridine diphosphate glucuronosyltransferase enzymes (UGTs)[30]. UGTs catalyze the conversion of MPA into an inactive phenolic glucuronide known as MPAG and a small amount of acyl-MPAG (Figure 1.2). Glucuronidation of MPA improves water solubility, promoting elimination of the metabolites (MPAG, Acyl-MPAG) from the body[31]. Data suggests that while MPA glucuronidation takes place predominantly in the liver, this process can partially occur within the intestines and kidneys[32]. MPAG and acyl-MPAG from the liver are primarily excreted in the urine, however, a small portion (~10%) is transported into the GI tract via the ATP-binding cassette subfamily C member 2 (ABCC2) protein[26]. Inside of the GI tract, bacterial GUS enzymes cleave the glucuronic acid (GA) moiety from MPAG, releasing free MPA and GA back into the intestinal lumen[31]. Free MPA is subsequently reabsorbed by the intestines and undergoes enterohepatic recirculation[33]. Recirculation of MPA is associated with multiple concentration peaks and an increased half-life, leading to further systemic MPA exposure as well as local exposure to active MPA in the intestines[33]. As mentioned previously, the extent of GI toxicity in patients appears to

be influenced by increased local exposure to MPA in the intestines. The activity of bacterial GUS enzymes indicates that MMF toxicity is dependent on the presence of an intact gut microbiota[26,27]. Yet, the intracellular mechanism through which MPA produces local toxicity is not known.

### 1.3.4 Role of Commensal Microbiota in MMF-induced GI Toxicity

Previous work has demonstrated that mice treated with MMF exhibit significant weight loss and colonic inflammation; however, this observation was absent in germ-free mice and in those treated with antibiotics[26,27]. Additionally, it was found that MMF altered gut microbial composition, with increases in Proteobacteria and lipopolysaccharide biosynthesis genes[27]. Such data suggests the presence of an important relationship between the gut microbiome and the perpetuation of MPA-induced GI toxicity. Metagenomic and proteomic analysis have also identified specific GUS enzymes responsible for reactivation of MPA, with flavin mononucleotide-binding GUS enzymes being particularly effective at MPA reactivation within the intestines[34]. Reactivation of MPA within the gut alters therapeutic concentrations, intensifying adverse side effects such as vomiting, diarrhea and ulcers[34]. Studies into sex-related differences in MMF toxicity, show that female rats have greater susceptibility to GI toxicity when compared to males[35]. Differences between male and female rats was theorized to result from lower rates of MPA glucuronidation in the intestines, highlighting the role of intestinal enzymatic activity in modulating MPA-induced GI toxicity[35]. Together these results indicate a complex relationship between glucuronidation and bacterial metabolism in MPA-induced GI toxicity. Though this relationship does not explain the exact mechanism through which local intestinal MPA exposure produces deleterious effects.

Since MMF is commonly prescribed as a long-term medication[36], an antibiotics-focused strategy may not represent a feasible option. This is because the gut microbiome plays an essential role in metabolic and homeostatic processes within the body[37]. Destroying microbiota diversity and populations has been linked to development of inflammatory bowel disease, irritable bowel syndrome, and systemic diseases[37]. Considering the importance of the microbiome, and its role in MPA-induced toxicity, identifying the mechanism through which MPA induces toxicity and developing strategies to mitigate these effects is pertinent.

### 1.3.5 Current Strategies to Mitigate GI Toxicity

Comprehensive assessment of current literature suggests that there are few strategies to alleviate MMF-induced GI toxicity. Presently, there are three main mitigation categories. These categories can be broken down into pharmacological interventions, personalized monitoring, and lifestyle adjustments.

Pharmacological interventions involve alternative formulations, dose adjustments, and adjunctive medications. Enteric-coated mycophenolate sodium (EC-MPS) is an alternative formulation of MMF that was developed to promote patient tolerability and to protect the upper GI tract from MPA toxicity[38]. EC-MPS is considered therapeutically equivalent to MMF, and has demonstrated similar efficacy and safety[39]. However, while EC-MPS was designed to reduce adverse GI side effects, cases of EC-MPS induced colitis and other typical MMF-related deleterious effects have been reported[40]. EC-MPS side effects were ameliorated only after discontinuation, suggesting that the alternative formulation does not eliminate the risk of GI injury[40]. As mentioned previously, dosage reduction and discontinuation of MMF therapy does markedly improve GI injury, however, making these adjustments can significantly threaten the health and safety of patients requiring immunosuppressive therapy[41]. Thus, dose adjustments do

not represent a safe and feasible strategy for mitigating toxicity. Adjunctive MMF therapy with immunosuppressants such as tacrolimus has proven effective in achieving adequate immunosuppression and reducing certain side effects[42]. However, this benefit is not universally observed, as research has demonstrated that MMF may also amplify the negative effects of tacrolimus and sirolimus[43].

Therapeutic drug monitoring (TDM) of MMF aims to optimize immunosuppressive efficacy while minimizing toxicity. This process is particularly relevant in transplantation and autoimmune disease treatments, where precise dosing can significantly impact outcomes. Literature suggests that TDM of MMF is recommended to manage interpatient variability and drug interactions that affect MPA levels[44]. Studies have shown that TDM assists in achieving personalized target MPA levels, improving clinical outcomes after transplantation[45]. However, the relationship between MPA exposure and MMF dose is complex, and the predictive value of MPA trough levels for toxicity is not consistently supported[46,47]. Furthermore, TDM of MMF is vulnerable to intra-patient variability, with no correlation between MPA pharmacokinetics and adverse side effects[46]. Unfortunately, while TDM of MMF has potential applications in improving patient outcomes, the evidence is not unequivocal. Until further research is published, the use of TDM for MMF therapy remains a contradictory topic, with no clear consensus on routine application in clinical practice. Though, individualized dosing based on patient contexts does represent a valuable area of exploration to improve patient outcomes.

Interestingly, dietary and lifestyle interventions may show promise in alleviating some MMF-induced side effects. For example, studies have shown that dietary fiber can be protective against abdominal pain and diarrhea, both of which are common side effects of MMF[48,49]. Additionally, consumption of probiotic yogurt has the potential to positively influence gut

microbiota and aid in the management of GI ailments. One study found that probiotic yogurt consumption alters microbiota diversity and decreases the relative abundance of LPS-producing bacteria in hamsters[50]. Though no specific diet studies looking at dietary fibers or probiotic yogurt have been conducted on patients during MMF therapy, therefore, nothing conclusive can be said about the efficacy of these approaches. However, probiotic supplementation does demonstrate potential to improve MMF tolerability. When patients taking MMF were provided a multistrain probiotic formula there was a 71.6% reduction in the risk of diarrhea, suggesting that probiotics may alleviate some of the negative effects associated with MMF[51].

### 1.3.6 Research Gap: Current Experimental Models for MMF-Induced GI Toxicity

At present, research gaps exploring MMF toxicity are related to limitations of existing experimental models and the need for more comprehensive and translational studies, especially with studies focused on exploring inter- and intra-patient variability. As mentioned previously, there remains a critical lack of understanding for the intracellular mechanisms underlying MMF-induced GI toxicity. While certain areas have been clarified, such as the role of the microbiome, there is insufficient evidence as to why localized MPA exposure leads to intestinal injury.

Published literature has made use of various experimental models, and while impactful, some of models lack the specificity and reproducibility required to comprehensively elucidate the molecular mechanics behind localized MPA toxicity. For example, most studies investigating MPA-induced GI toxicity utilize human colon adenocarcinoma (Caco-2) monolayers to model intestinal barrier function [52–55]. Some of these studies have found that MPA-induced toxicity is not mediated through apoptosis and that MPA compromises tight junction integrity via midkine modulation and MLC-2 regulation[52,53]. Others have reported contradictory results, with barrier

dysfunction occurring through mitochondrial reactive oxygen species and apoptosis[54]. Of the limited studies conducted, some have also been retracted[56]. The apparent lack of studies, and the existence of contradictions between studies emphasizes the need for additional investigations.

Notably, reproducibility problems with caco-2 models has already been discussed in literature [55]. Caco-2 monolayers are derived from a single cell type, which poorly captures the complexity and diversity present in the intestinal epithelium. The lack of cell type representation means that goblet cells, enteroendocrine cells, paneth cells, and transit amplifying cells, are not considered in these studies. Moreover, Caco-2 models are derived from colorectal adenocarcinoma cells, suggesting that these models do not accurately reflect normal, healthy intestinal epithelia due to intrinsic genetic and phenotypic alterations[57]. Caco-2 monolayers also do not produce a mucus layer, which is a vital feature of intestinal barrier function *in vivo*[58]. While Caco-2 cells have demonstrated meaningful applicability in the past, it is important to consider the limited physiological relevance of the model. Studies have also shown the potential of utilizing human intestinal epithelial cells (HIEC-6) as an alternative *in vitro* model, however, while more physiologically relevant, HIEC-6 monolayers still lack cell type diversity, and do not produce a mucus layer[57].

Animal models have a strong proven background in science. Mouse models are frequently used due to their physiological similarities to humans and well-established protocols. Mice have been used extensively in MMF studies and were a critical aspect in the preclinical trials for MMF applicability and tolerability in humans[59–61]. Whole animal models introduce systemic effects and interactions between organs. In the case of studying MMF-induced toxicity, systemic interactions proved beneficial for elucidating the relationship between the microbiome and MPA toxicity in the gut[26,27]. However, while mice have been pivotal in studying human

disease, their ability to fully replicate the complexity of human physiology is limited due to intrinsic genetic and physiological differences[62]. Whole animal studies also raise ethical issues regarding the use of living creatures for research. How many animals are required to establish tangible results, and do the outcomes outweigh the multitude of sacrificed lives? Furthermore, the presence of secondary pathological processes can restrict measurement of toxicity mechanisms *in vivo*[63]. Using an *in vitro* cell model permits more precise control of local concentrations while avoiding these secondary pathological processes[63]. Given that this thesis is predominately focused on understanding the mechanisms behind local MPA toxicity in the intestines, an isolated model of intestinal physiology using primary mouse organoids was decided upon.

## 1.4 Organoid Model System

### 1.4.1 Colonic Organoids – An Overview

Utilizing relevant biological models is crucial for robust examination of cellular mechanisms and organization. The development of increasingly complex systems has expanded significantly in the last decade due to the limitations of traditional two-dimensional (2D) cell models [64]. Traditional 2D models inadequately represent *in vivo* conditions and therefore lack accurate predictivity of real-world therapeutic applications in humans[57]. The hunt for improved models led to the creation of three-dimensional (3D) cell cultures that, unlike 2D models, allow cells to grow in 3D space analogous to how they would *in vivo*[65]. Development of these models has facilitated the establishment of cultures composed of self-organizing masses of cells called organoids[66]. Organoids model the complexity of specific organs of interest with enhanced physiological relevance, mimicking the key structural, functional, and biological components[65].

Organoids provide an appropriate platform for translational research without the need for animal models and can be utilized for personalized research as the cells possess the intrinsic characteristics of the tissue they were derived from[67]. While organoids represent an effective alternative to whole animal models, a source of stem cells is still required to generate organoid culture[66].

Throughout the intestines are invaginations of the intestinal wall, these contiguous pockets are called intestinal crypts. Crypts possess Lgr5+ stem cells that are constantly dividing to maintain the ever-shedding intestinal epithelium[68]. The identification of these stem cells and subsequent discovery of the factors required to maintain their niche made it possible to establish self-organizing intestinal organoids[69]. Organoids generated from the isolation of colonic crypts are called colonoids. The ability to accurately and comprehensively model colon physiology makes colonoids a desirable biological model for clinical investigations of pharmacokinetics, and drug toxicity[70]. Based on these characteristics, we determined that a colonoid model would best suit our goals to investigate the mechanisms of MPA exposure in the GI tract.

While colonoids represent an effective model for studying GI physiology, 3D culture limits the study of barrier interactions because the lumen is not directly accessible to the external environment[71]. Previous studies have demonstrated positive results using 3D culture for epithelial barrier function analysis[72,73], however, there exists methods to improve lumen accessibility. For example, colonoids can be processed and subsequently plated onto permeable membrane inserts to generate polarized monolayers permitting assessment of both apical and basolateral compartments. Adapting 3D colonoid cultures into monolayers presents the opportunity to conduct additional techniques such as transepithelial electrical resistance (TER) measurement, allowing quantification of epithelial barrier integrity and permeability[71].

### 1.4.2 Advantages and Limitations

Although colonoids (2D and 3D) provide utility as an advanced, cutting-edge *in vitro* model, there is a distinct set of advantages and disadvantages that can affect experimental outcomes.

Colonoids exhibit strong self-renewal capabilities and can be maintained in culture for extended periods, facilitating long-term studies and repeated experimentation[74]. Additionally, colonoids maintain a high degree of genotypic consistency with the original tissue, ensuring reliability over longer periods[75]. Their complex composition consisting of stem cells, enterocytes, goblet cells, paneth cells, and enteroendocrine cells provide crucial representation for studying interactions within the epithelial barrier[76]. As mentioned above, the closed structure of colonoids limits access to the luminal compartment, posing challenges for studies seeking to investigate luminal interactions[76]. However, these accessibility issues can be overcome with monolayer production. Colonic organoids are also technically demanding and costly, requiring the use of specialized media and matrix components which can complicate reproducibility due to variability in protocol and reagent compositions[77]. Furthermore, colonoids are typically cultured within matrices of poorly defined composition, and are provided media saturated with growth factors, which may lead to inconsistencies compared to the natural *in vivo* environment[78].

In contrast, colonoid monolayers offer enhanced accessibility to both the apical and basolateral surfaces, thereby facilitating studies involving barrier function and drug interactions[79]. Colonoid monolayers may also be adjusted through modulation of differentiating factors, altering the culture to study specific target cells and associated mechanisms of action[79]. Compared to single-cell monolayers, the complexity of organoid monolayers better represent *in vivo* functionality, and can be used to demonstrate interpatient heterogeneity based on the

intrinsic characteristics of donor tissue[79]. However, monolayers do lack 3D architecture, which may limit their ability to fully replicate the *in vivo* environment[78]. Static monolayer models are also not subjected to physical forces present *in vivo* such as mechanical stresses from peristalsis and fluid shear stress from movement in the intestines[71]. Additionally, the monolayer model chosen for this thesis does not possess *in vivo* components such as the vasculature, neurological networks, immune system, and more[80]. Most notably, the gut microbiome, which was previously discussed as a facilitator of MMF-induced GI toxicity is also absent. It is important to consider that the observations in this model are limited to the physiological processes of the intestinal epithelium alone. Though these limitations may be mitigated through the employment of co-culture systems, improving *in vivo* representation in exchange for increased technical requirements and cost[80].

## 1.5 Significance and Impact

The research conducted in this thesis holds potential for advancing our understanding of the intracellular mechanisms underlying MPA-induced GI toxicity. Despite the clinical importance of MMF, the precise mechanisms of toxicity remain poorly understood. This thesis seeks to fill that critical knowledge gap by leveraging a cutting-edge colonoid model.

To our current knowledge, this work represents the first investigation of MPA-induced GI toxicity using a colonoid model. This model offers a more physiologically relevant platform compared to previous studies using traditional *in vitro* approaches. We aspire for the results of this thesis to help guide future study aimed at enhancing patient tolerability, quality of life, and outcomes.

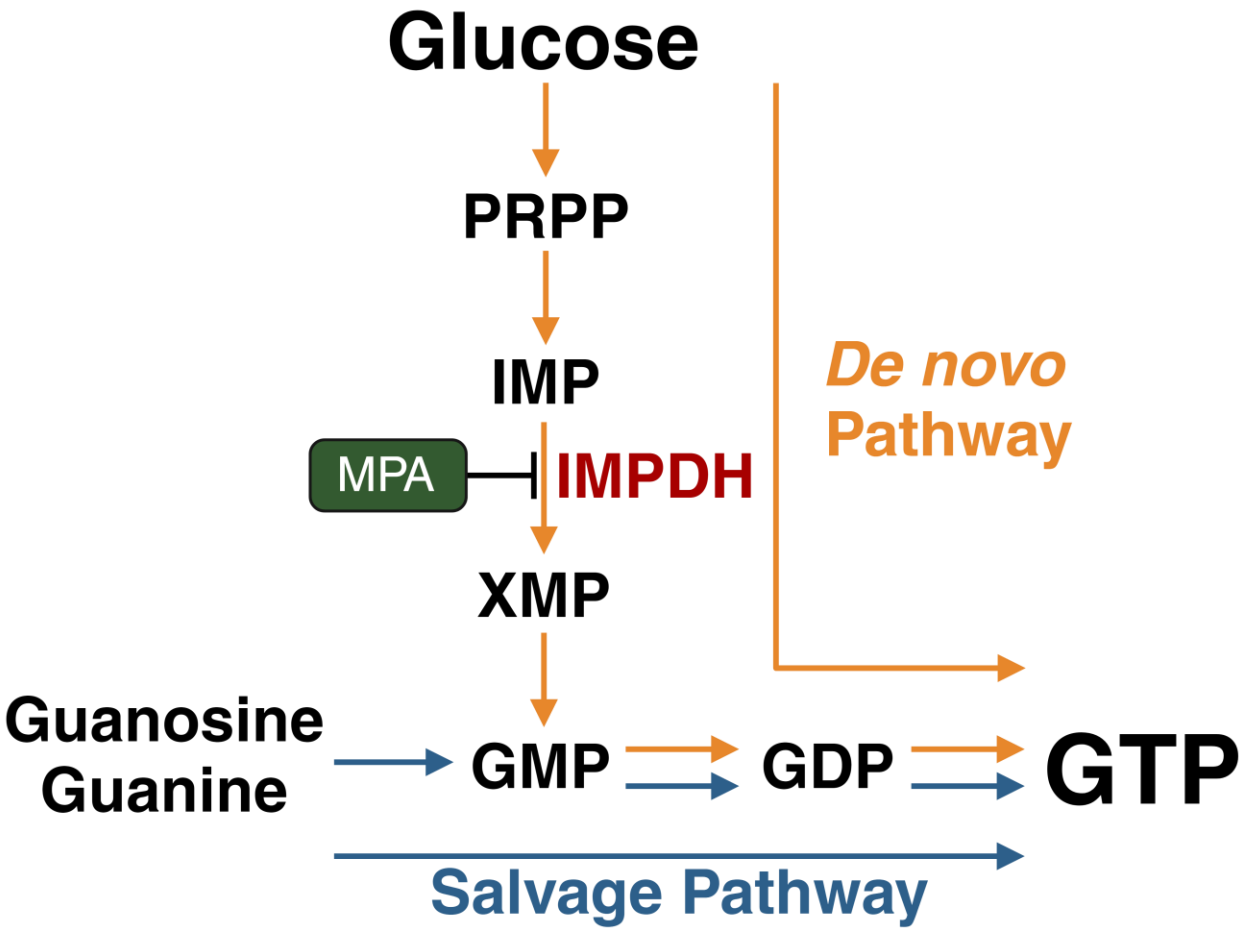


**Figure 1.1** Effect of MPA on Purine Metabolism. MPA inhibits IMPDH activity in lymphocytes. IMPDH is a key enzyme in the *de novo* synthesis (orange) of guanine nucleotides. Many cell types may utilize a separate salvage pathway (blue) to regulate cellular nucleotide levels. Available data suggests that activated lymphocytes almost exclusively rely on the *de novo* pathway for nucleotide synthesis[16]. It is through this mechanism that MPA inhibits lymphocyte proliferation leading to an immunosuppressive effect. *Created with BioRender.com*

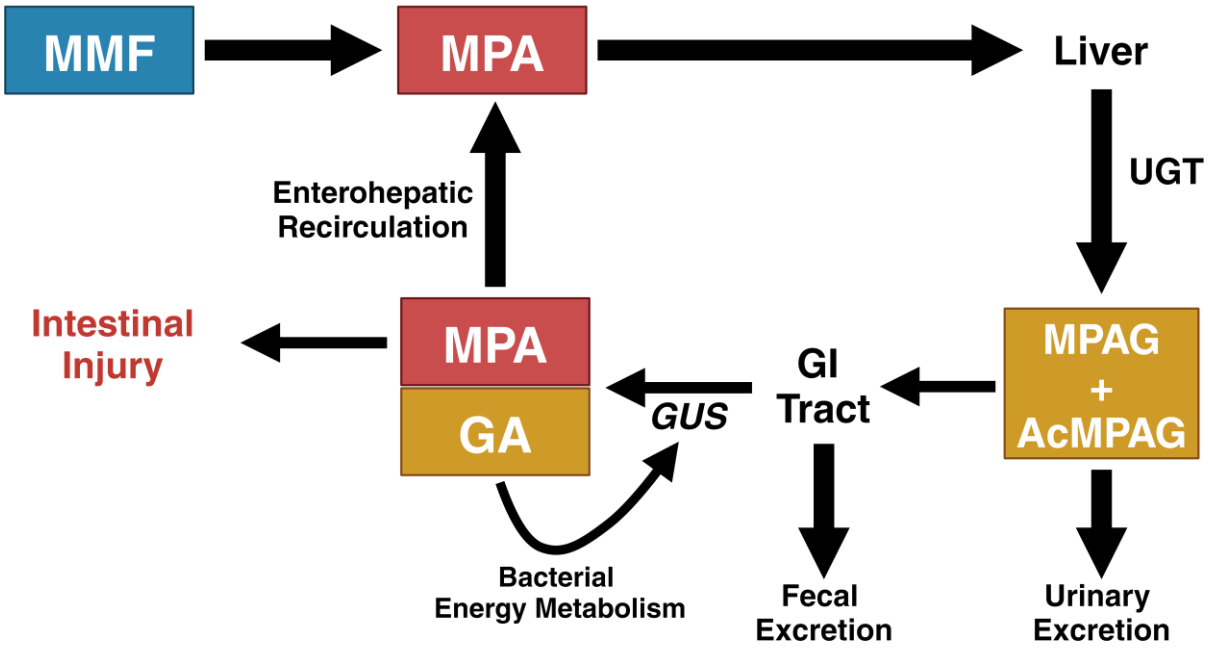


**Figure 1.2** Pathway of MMF metabolism and MPA-induced colonic injury. After consumption, MMF is hydrolyzed to active MPA. MPA exerts an immunosuppressive effect and is subsequently inactivated through glucuronidation via UGTs. UGTs catalyze the conversion of MPA into MPAG and Acyl-MPAG (AcMPAG). MPAG and AcMPAG are primary excreted through the urine, however, some molecules are transported into the GI tract. Inside the GI tract, bacterial GUS enzymes cleave the GA moiety from MPAG, releasing free MPA back into the intestinal lumen. Active MPA within the intestines is associated with adverse GI side effects. MPA in the intestines can be reabsorbed, undergoing enterohepatic recirculation. *Created with BioRender.com*

# 2.1 HYPOTHESIS AND PROJECT AIMS

## 2.2 Project Aims

To analyze the mechanisms behind MPA-induced GI toxicity, we sought to develop a model system using primary mouse colon organoids to investigate MPA exposure at physiological concentrations. After generating colonic organoids, our aim was to evaluate the model system during and after MPA exposure using a variety of assays and functional analyses. Our final aim was to leverage the data from our model to reveal affected pathways and to elucidate the mechanisms behind MPA-induced GI toxicity.

## 2.3 Hypothesis

We hypothesize that localized exposure to active MPA within the intestines induces cellular damage, inflammation, and diminished proliferation, leading to intestinal injury, increased barrier permeability and tight junction dysfunction.

# 3.1 MATERIALS AND METHODS

## 3.2 Materials, Reagent Compositions, and Equipment

**Table 3.1** Summary of materials used.

| Material | Brand/Supplier | Catalog Number/Code |
|---|---|---|
| 0.25% Trypsin-EDTA | Gibco | 25200072 |
| 0.4% Tryphan Blue Solution | Gibco | 15250061 |
| 0.4 µm Thincert trans-well insert | Greiner Bio-One | 662641 |
| 4% Paraformaldehyde (PFA) | Thermo Scientific | CAAAJ61899-AP |
| Advanced DMEM (ADF) | Gibco | 12491023 |
| Alexa Fluor™ 555 ZO-1 Monoclonal Antibody | Invitrogen | MA3-39100-A555 |
| Bovine Serum Albumin (BSA) | VWR | K719 |
| B27 supplement | Gibco | 17504044 |
| Cell culture multiwell plate, 24 well | Greiner Bio-One | 662160 |
| Cell culture multiwell plate, 48 well | Greiner Bio-One | 677180 |
| CHIR99021 | Sigma-Aldrich | SML1046 |
| Crypt isolation buffer | HOIH | In-house preparation |
| DAPI | Invitrogen | D1306 |
| Epidermal growth factor (EGF) | Amsbio | GF-010-8 |
| Fetal bovine serum (FBS) | Sigma-Aldrich | F1051 |
| Freezing media | HOIH | In-house preparation |
| Glutamax | Gibco | 35050061 |
| Goat anti-Mouse IgG1 Secondary Antibody, Alexa Fluor™ 488 | Invitrogen | A-21121 |
| Hanks' balanced salt solution (HBSS) | Gibco | 14175095 |
| HEPES | Gibco | 15630080 |
| Matrigel matrix | Corning | 354230 |
| Minigut medium | HOIH | In-house preparation |
| Mr. Frosty™ Freezing Container | Thermo Scientific | 5100-0001 |
| Mycophenolic acid | Sigma-Aldrich | M5255 |
| N-acetylcysteine (NAC) | Sigma-Aldrich | A9165 |
| N2 supplement | Gibco | 17502048 |
| Penicillin-Streptomycin | Sigma-Aldrich | P4333 |
| Phosphate Buffered Saline (PBS) | Gibco | 10010023 |
| Primocin | Invivogen | ant-pm-1 |
| Recovery Media | HOIH | In-house preparation |
| RNeasy Mini Kit | Qiagen | 74104 |
| SB431542 | Tocris | 1614 |
| Sucrose | Fisher Chemical | S5-500 |
| Thiazovivin | Sigma-Aldrich | SML1045 |

| | | |
|---|---|---|
| TriReagent | Sigma-Aldrich | T9424 |
| TritonX | Millipore | TX1568 |
| Tween-20 | Sigma-Aldrich | 9005645 |
| WRN Conditioned Media | HOIH | In-house preparation |
| Y-27632 dihydrochloride | Tocris | 1254 |
| ZO-1 Monoclonal Antibody | Invitrogen | 33-9100 |

### 3.2.1 Reagent Compositions

**Table 3.2** Compositions of in-house prepared reagents**.**

| Reagent | Composition |
|---|---|
| 2D Mouse Complete Medium (2D-MCM) | For ≈ 40 mL total:<br>20 mL Minigut medium<br>20 mL Mouse WRN Conditioned Medium<br>4 µL EGF (500 µg/mL stock)<br>80 µL Primocin (50 mg/mL stock)<br>40 µL Y27632 (10 mM stock) |
| 3D Mouse Complete Medium (3D-MCM) | For ≈ 40 mL total:<br>20 mL Minigut medium<br>20 mL Mouse WRN Conditioned Medium<br>4 µL EGF (500 µg/mL stock)<br>80 µL NAC (0.5 M stock)<br>80 µL Primocin (50 mg/mL stock)<br>*40 µL Y27632 (10 mM stock)<br>* Added after plating, not during routine media changes |
| Crypt isolation buffer | For ≈ 8 mL total:<br>8 mL PBS<br>1.5g Sucrose<br>32 µL EDTA (0.5M stock)<br>2 µL DTT (2M stock) |
| Freezing media | For 10 mL total:<br>8 mL DMEM<br>1 mL FBS (10% of total volume)<br>1 mL DMSO (10% of total volume) |
| Minigut medium | For 500 mL total:<br>470 mL ADF<br>5 mL Glutamax (200 mM stock)<br>5 mL HEPES (1 M stock)<br>5 mL Pen/strep solution (100x stock)<br>5 mL N2 supplement (1x stock)<br>10 mL B27 supplement (1x stock) |
| PBS2 | For 40 mL total:<br>39.2 mL PBS |

| | |
|---|---|
| | 0.8 mL FBS (2% of total volume) |
| Recovery media | For 40 mL total:<br>39.930 mL 3D-MCM<br>10 µL Thiazovivin (10 mM stock)<br>4 µL SB431542 (10 mM stock)<br>16 µL CHIR99021 (10mM stock)<br>40 µL Y27632 (10 mM stock) |
| Washing media | For 40 mL total:<br>36 mL ADF<br>4 mL FBS (10% of total volume) |

### 3.2.2 Equipment

**Table 3.3** Summary of equipment used

| Equipment Type | Product/Model |
|---|---|
| Benchtop centrifuge | Sorvall ST8R |
| Biological safety cabinet | Thermo Scientific™ 1300 Series Class II, A2 |
| $CO_2$ incubator | Heracell™ VIOS 160i CO2 Incubator |
| Epithelial voltohmmeter | World Precision Instruments EVOM2 |
| Fluorescence microplate reader | Spectramax i3x |
| High-throughput RNA sequencing system | Illumina NovaSeq 6000 |
| Inverted cell culture microscope | Olympus CKX53 |
| Confocal microscope | Nikon Eclipse Ti2/Nikon A1+ |
| Microvolume spectrophotometer | NanoDrop 2000c |
| Voltohmmeter electrodes | World Precision Instruments STX2 |

## 3.3 Establishing and Maintaining Primary Mouse Colonoid Culture

Methods and materials for establishing, growing, and maintaining 3D colonoid culture were provided through the HOIH. The following methods have been adapted from the HOIH protocols and have been optimized to fit the aims of this thesis.

### 3.3.1 Colon Crypt Isolation

Male C57BL/6 mice were ethically sacrificed in preparation for tissue sample collection. Sacrificed mice were abdominally incised, and a scalpel was used to cut out a section of the large intestine after the cecum and before the anus. The resulting fragment of colon tissue was removed and placed into an ice bucket containing a petri dish filled with 30-50 mL of ice-cold PBS. The tissue was trimmed to remove as much excess fat as possible. A pipette containing 1 mL of PBS was inserted into one end of the colon to flush out loose debris. Tissue with excess debris was placed on paper towel pre-wet with PBS and slowly compressed with sterile forceps to remove stuck material. The colon was then cut longitudinally using sterile surgical scissors to form a flat sheet. The resulting tissue was washed thoroughly in the petri dish containing ice-cold PBS using a continuous figure-eight motion until all visible debris was removed. The washed tissue was then moved to a 1.5 mL tube containing 1 mL of ice-cold PBS. Sterile mincing scissors were submerged into the tube and used to process the colon tissue into small fragments ($\leq$ 1mm). Pre-cut 1 mL pipette tips coated with PBS2 (Table 3.2) were then used to transfer the tissue fragments into a 50 mL tube containing 20 mL of fresh PBS. The 50 mL tube was vigorously shaken by hand for approximately 30 seconds before being left to settle for another 30 seconds on ice. Once settled, the tube was placed into a centrifuge (Table 3.3) and pulse spun at 300 x g for 30 seconds at room temperature (RT). Supernatant was aspirated, and the PBS

wash was repeated two more times. After the final wash, excess PBS was removed so that less than 1 mL remained in the tube.

After extensive washing, 30 mL of ice-cold crypt isolation buffer (Table 3.2) was added to the tube. The tube was subsequently placed on a rocker (speed 12-20 RPM) and incubated at 4°C for 30 minutes. Following this, all work was conducted in a bio safety cabinet to maintain sterile conditions. After the 30-minute isolation process, the tube was placed upright so that the tissue would settle. 10 mL of ice-cold PBS was then added. The settled tissue was pipetted up and down several times (x6) using a pre-cut 1mL pipette tip (larger opening to prevent clogging). During this process, the pipette tip was held closely against the bottom of the tube to help dislodge cells. Following mechanical disruption, the pieces were briefly left to settle. The supernatant was then collected and placed into a separate 50mL tube labelled “A” (on ice). An additional 10 mL of ice-cold PBS was added to the settled pellet, and the tissue was again mechanically disrupted via pipetting several more times (6x). The resulting supernatant was removed and placed into tube “A”. Again 10 mL of ice-cold PBS was added to the tube containing the tissue fragments. The sample was pipetted up and down several times (6x). The pieces were left to settle, and the supernatant was removed and placed into a separate 50 mL tube labelled “B” (on ice). This washing process was repeated 5x using fresh PBS for each wash. Supernatant from washes 3-7 were transferred to the tube labelled “B”. Next, a 100 µm cell strainer was pre-coated PBS2. All contents from tube “B” were filtered through the pre-coated cell strainer into a new 50 mL tube labelled “C”. Tube C was then spun at 300 x g for 5 minutes at 4°C. After centrifugation, supernatant was removed, and the resulting cell pellet was resuspended in 1 mL of ice-cold washing media (Table 3.2). The cell suspension was then transferred to a fresh 1.5 mL microtube. The 1.5 mL tube was subsequently pulse spun for 15-30

seconds at RT to form a dense pellet. After spinning the supernatant was aspirated to remove as much liquid as possible without disrupting the pellet. Here the pellet contained the isolated crypt structures. These crypts could either be frozen for later use or suspended into Matrigel (Table 3.1) domes to form colonoid culture. At this stage, the contents of tube "A" could either be discarded or kept as backup depending on the outcome of the protocol.

### 3.3.2 Establishing Colonoid Culture

Following crypt isolation, crypt cells were resuspended into a small volume of Matrigel on ice (20 µL Matrigel per organoid dome). Matrigel was kept on ice to minimize premature polymerization. The size of the crypt pellet was used to inform the amount of Matrigel, with 160 µL being needed on average per colon sample. Before plating, cells were extensively mixed with the Matrigel to promote uniform distribution. 20 µL of the Matrigel cell suspension was applied to the center of each well in either a 24-well or 48-well culture plate (Table 3.1). To promote adhesion and polymerization of the Matrigel domes, culture plates were pre-heated to 37°C before plating. To avoid creating bubbles during plating, pipettes were pressed to the first stop, leaving a small amount of material in the pipette tip. Due to this, a pipette setting of 22-23 µL was used to account for the remaining Matrigel. After all the Matrigel was plated, the droplets were left to rest for approximately 2-4 minutes at RT. Quickly afterwards, the plate was inverted and placed into an incubator (37°C, 5% $CO_2$) for 30 minutes to encourage formation of 3D domes. After 30 minutes each organoid dome was provided with 500 µL of 3D-MCM (Table 3.2) and the plate was placed back into the incubator.

### 3.3.3 3D Mouse Complete Medium Preparation

3D-MCM was purchased from the HOIH in weekly batches. 3D-MCM was formulated and prepared by the HOIH (Table 3.2). For primary mouse colon organoids, 3D-MCM was prepared by adding equal parts Minigut Medium and Mouse WRN Conditioned Medium (Table 3.2). This preparation was supplemented with EGF (Table 3.1) at a final concentration of 50 ng/mL and with NAC (Table 3.1) at a final concentration of 1 mM. Before media changes, 3D-MCM was freshly supplemented with Primocin (Table 3.1) at a final concentration of 10 µg/mL. 3D-MCM was also supplemented with 10µM Y27632 (Table 3.1) when feeding immediately after crypt isolation or passaging. Subsequent media changes did not contain Y27632.

### 3.3.4 Monitoring Mouse Colonoids

Primary mouse colonoids were observed daily using bright-field microscopy (Table 3.3) at 4x, 10x, 20x and 40x magnifications. Images and videos of the colonoids were captured regularly with a Olympus EP50 WLAN microscope camera attachment, using EPview software. Colonoids were assessed and characterized using bright-field microscopy to determine culture conditions and suitability for passaging, monolayer generation, and experimentation.

### 3.3.5 3D-MCM Maintenance

3D-MCM changes typically took place every 1-2 days, depending on colonoid culture density and maturity. Media changes were conducted when media color started to change from red to yellow (Figure 4.4). Formulation of 3D-MCM media varied based on circumstance. For example, during typical media changes 3D-MCM was not supplemented with Y27632; however, after new plating (crypt isolation or passaging) 3D-MCM was supplemented with 10µM

Y27632. Before replacing the old media, fresh 3D-MCM was pre-warmed in a hot water bath (37°C).

Briefly, 3D-MCM changes were conducted in the sterile environment of a biosafety cabinet (Table 3.3). Culture plates were tilted at a 45° angle and the old media was removed using a vacuum aspirator. Aspiration was preformed cautiously to mitigate disruption of the Matrigel domes. Following removal of the old media, 500 µL of pre-warmed 3D-MCM was dispensed into each well. To reduce Matrigel disruption media was added slowly down the side of each well to minimize splashing and displacement of the Matrigel dome.

### 3.3.6 Passaging Mouse Colonoids

To maintain optimal culture conditions colonoids were split every 4-6 days. Plates containing colonoids ready for passaging were transferred and processed in a biosafety cabinet. To start, 3D-MCM was aspirated from each well. After aspiration, 500µL of ice-cold ADF (Table 3.1) was added to each well containing colonoids. Unlike media changes, ADF was added directly on top of the Matrigel domes to promote breakdown of the structure. Following addition of ADF, a fresh 1 mL pipette tip was pre-wet with PBS2. Each Matrigel dome was then pipetted up and down vigorously and transferred to an appropriately sized tube (15 mL or 50 mL depending on number of Matrigel domes). Well bottoms were also scrubbed with the pipette tip to ensure full dislocation of the Matrigel structure. Scrubbing of the wells was only performed with ADF present to minimize cell damage. After collecting all the colonoids, an equal volume of trypsin-EDTA (Table 3.1) was added to the tube. For instance, if 12 mL of ADF was used to harvest the colonoids, then 12 mL of trypsin would be added. The ADF/trypsin solution was placed on ice

and left to incubate for 30 minutes. Every 5-10 minutes the tube was periodically swirled/shaken to help dissociate the organoids.

After 30 minutes, the tube was transferred into a hot water bath at 37°C. The organoids were trypsinized at 37°C for 10 minutes, again with periodic swirling and shaking of the tube to promote dissociation of the cells. After 10 minutes the solution was brought back into the biosafety cabinet, and a 1 mL pipette pre-wet with PBS2 was used to further disrupt the colonoids. The organoid suspension was extensively pipetted to ensure adequate dissociation of the cells and breakdown of the Matrigel matrix. This process was performed quickly to minimize damage from excessive trypsin digestion (< 1 min). Immediately after, trypsin was inactivated by the addition of ice-cold washing media (2x the volume of trypsin) and the tube was vigorously shaken for 30 seconds. The cell suspension was then centrifuged at 300 x g for 5 minutes at RT. After 5 minutes the tube was swapped to the opposing side of the centrifuge and the process was repeated. After centrifugation, a visible pellet would form at the bottom of the tube. If poor pelleting was observed, the tube was re-spun above 300 x g for 5 minutes (400-800 x g). The resulting supernatant was carefully aspirated to not disturb the pellet. The pelleted cells were subsequently suspended in 1 mL of fresh washing media and transferred to a new 1.5 mL microtube. Again, the cells were spun and pelleted following the same process as mentioned above. Depending on the presence of debris, an additional washing step would be conducted with fresh washing media. At this point the pelleted cells were either frozen for later use or resuspended in fresh Matrigel to establish new colonoid cultures.

Plating passaged colonoids follows the same process as plating isolated crypts. Briefly, the pellet of dissociated colonoids was resuspended into Matrigel on ice (20 µL Matrigel per organoid dome). The size of the pellet was used to inform the amount of Matrigel; with most

splitting being conducted at a 1:2 ratio. For example, if 10 Matrigel domes were collected for passaging, then 20 Matrigel domes would be plated after splitting. Though this decision often depended on overall culture density. If culture density was notably low, the ratio would be decreased so that 10 Matrigel domes would be passaged back into 10 Matrigel domes to promote higher density colonoid culture. Similarly, if culture density was too high, 10 Matrigel domes would be split into 30 domes after passaging to promote lower organoid density.

When plating, 20 µL of the Matrigel cell suspension was applied to the center of each well of a pre-warmed culture plate. Once all the Matrigel was plated, the droplets were left to rest for approximately 2-4 minutes at RT. Quickly afterwards, the plate was inverted and placed into an incubator for 30 minutes to promote the formation of 3D domes. After 30 minutes of polymerization, each organoid dome was provided with 500 µL of fresh warm 3D-MCM supplemented with Y27632, and the cells were placed back into the incubator (37°C, 5% $CO_2$).

### 3.3.7 Freezing 3D Mouse Colonoids

As mentioned in section 3.3.6, pelleted cells from the splitting process could either be treated for freezing or suspended in Matrigel for culture generation. When freezing, the pelleted cells were resuspended into freezing media (Table 3.2) instead of Matrigel. When resuspending in freezing media, a ratio of 3 Matrigel domes per 1 mL of freezing media was used. For example, if 21 Matrigel domes were collected during passaging, then 7 mL of freezing media was used. Once resuspended, the cells were then transferred into cryovials (1 mL per vial) and placed into a Mr. Frosty™ Freezing Container. The container was then placed into a freezer at -80°C. The cells were left to freeze for approximately 24 hours. The next day, cryovials were quickly transferred to a liquid nitrogen tank for long term storage, with the date and passage number being recorded.

### 3.3.8 Thawing 3D Mouse Colonoids

When additional colonoids were needed, previously cryopreserved samples were thawed and used for culture generation. To start, DMEM + 1% BSA (Table 3.1) was prewarmed (2.5 mL per cryovial) to 37°C. Cryopreserved colonoids were retrieved from liquid nitrogen storage and subsequently thawed in a hot water bath at 37°C for approximately 1-2 minutes. Typically, a small amount of ice remained after removing the vials. Next, 500 µL of the warm DMEM + 1% BSA was added drop wise to each cryovial. Following this, a PBS2 coated pipette was used to gently resuspend the freshly thawed cells. The resulting cells suspensions were slowly transferred into another 15 mL conical tube. Each cryovial was then washed with 1 mL of the warm DMEM + 1% BSA solution and the remnants were transferred into the conical tube containing the cell suspension. The cells were then spun down at 200 x g for 5 minutes at RT. Next, the supernatant was removed, and the resulting pellet of thawed cells were resuspended into 1 mL of fresh warm DMEM + 1% BSA. Using a PBS2 coated pipette the cells were transferred into a new 1.5 mL microtube. Again, the cells were pelleted at 200 x g for 5 minutes at RT. If the resulting pellet was loose, this process was repeated. After spinning, the supernatant was removed, and the cells were resuspended into Matrigel and subsequently deposited on a prewarmed 24-well or 48-well plate using the same guidelines as stated in the above methods. After 30 minutes of incubation, each well containing a Matrigel dome was provided with 500 µL of prewarmed (37°C) recovery media (Table 3.2). Media was changed 24 hours later with 500 µL of fresh recovery media (no Y27632 supplementation). Following this, each media change was treated as normal, using 3D-MCM instead of recovery media.

## 3.4 Establishing and Maintaining Primary Mouse Colonoid Monolayers

Methods and materials for establishing, growing, and maintaining 2D colonoid monolayers were provided by the HOIH. The following methods have been adapted from the HOIH protocols and have been optimized to fit the aims of this thesis.

### 3.4.1 Monolayer Plate and Insert Preparation

24-well cell culture plates and trans-well inserts (Table 3.1) were prepared one day before monolayer plating. 24-well plates containing trans-well inserts were pre-warmed to 37°C in an incubator (1-2 hours). During pre-warming, a 1:50 Matrigel:ADF solution was prepared on ice (200 µL per trans-well insert). The Matrigel/ADF solution was added to the apical well of trans-well inserts and the plate was gently tapped to promote uniform coating of the Matrigel solution. Plates were incubated (37°C, 5% $CO_2$) for 2 hours to allow the Matrigel to solidify on the trans-well membrane. Following incubation, the Matrigel/ADF solution was aspirated. Next, pre-warmed (37°C) ADF was added to the apical well (300 µL) and basolateral well (500 µL) and placed back into the incubator for later use. Before monolayer plating, TER measurements were conducted to collect blank measurements. TER measurement of the Matrigel-coated inserts was performed as outlined in section 3.6.

### 3.4.2 Colonoid Collection and Single Cell Isolation

Colonoids were screened using bright-field microscopy (Table 3.3). Cultures of suitable density, maturity (Between day 4-6), and quality were selected for monolayer generation. Colonoids intended for processing into monolayers were managed simultaneously during routine passaging. Following the same process as highlighted in section 3.3.6, colonoids were collected from

Matrigel domes using ADF. Colonoids designated for monolayer preparation were placed in a separate tube during the collection process. Organoids were trypsinized and mechanically disrupted with a pipette according to a modified version of the procedure outlined in section 3.3.6. In this modified version, pipetting of the digested colonoids was closely observed. Mechanical disruption (pipetting) of cell clumps was performed until clumps were no longer visually distinguishable. The suspension was then trypsinized for an additional 5 minutes at 37°C to promote dissociation into individual cells. After digestion, the cells were once more disrupted using a fresh 1 mL PBS2 coated pipette (30 seconds – 1 minute). Immediately after, a 100 µL suspension sample was collected and transferred into a 1.5 mL microtube. The sample was stained with 0.4% Trypan Blue (Table 3.1) using a 1:1 ratio. Viable cells were counted on a hemocytometer, and the total amount of cells in suspension was calculated. Analysis of the cells on the hemocytometer indicated whether adequate digestion had taken place. If the cells demonstrated substantial clumping, the suspension was placed back into the hot water bath for 2-5 minutes for further digestion. Ideally, the collected sample would contain a substantial portion of individual cells suitable for plating. A cell count between $0.8 \cdot 10^6$ - $1 \cdot 10^6$ /mL was considered optimal for monolayer plating.

Once a feasible cell count was verified, washing media was added (2x the volume of trypsin-EDTA used) to the suspension to inactivate trypsin. The cells were then centrifuged at 300 x g for 5 minutes at RT. After spinning, the tube was moved to the opposing side of the centrifuge, and the process was repeated. Following centrifugation, the supernatant was carefully aspirated, leaving behind a pellet of cells. 1 mL of fresh washing media was added to the tube. The cells were resuspended using a PBS2 coated pipette and transferred into a new 1.5 mL

microtube. The cells were then pulse spun between 3000 – 4000 x g for approximately 30 seconds. The resulting pellet of cells were deemed ready for monolayer plating.

### 3.4.3 Plating Colonoid Monolayers

Monolayer inserts were pre-prepared as outlined in section 3.4.1. Following single cell isolation (section 3.4.2), washing media supernatant was carefully aspirated from the pelleted cells. Pre-warmed (37°C) 2D-MCM (Table 3.2) was added to the pelleted cells (300 µL per insert being plated). The pellet was re-suspended in the 2D-MCM using a PBS2 pre-coated pipette. Resuspension was carefully observed to ensure that no clumps were visually distinguishable. Before plating, inserts were removed from the incubator and ADF in the apical and basolateral compartments was aspirated. 300 µL of the 2D-MCM cell suspension was added to the apical well of each trans-well insert. This process was performed cautiously to avoid disruption of the Matrigel coated membrane. After adding all the 2D-MCM cell suspension, plates were gently tapped and swirled to promote uniform distribution of the single cells. Following this, 500 uL of pre-warmed (37°C) 2D-MCM was added to the basolateral compartment (plate wells) of each trans-well insert. After plating, the inserts were observed using bright-field microscopy to determine distribution of the cells. If non-uniform distribution was observed, plates were gently tapped and swirled. This process was repeated until cell distribution was satisfactory. Plates were then transferred into an incubator (37°C, 5% $CO_2$). Monolayers were cultured with routine media changes (section 3.4.6) over the next 7-14 days. Monitoring of monolayer development and confluency was performed as outlined in section 3.4.4.

### 3.4.4 Monitoring Colonoid Monolayers

Primary mouse colonoid monolayers were observed daily using bright-field microscopy (Table 3.3) at 4x, 10x, 20x and 40x magnifications. Images and videos of the monolayers were captured with a Olympus EP50 WLAN microscope camera attachment, using EPview V1.4 software. To determine confluency and suitability for experimentation monolayers were assessed using TER as outlined in section 3.6.

### 3.4.5 2D Mouse Complete Medium Preparation

2D-MCM was purchased from the HOIH in weekly batches. 2D-MCM was formulated and prepared by the HOIH. For primary mouse colonoid monolayers, 2D-MCM was prepared by adding equal parts Minigut Medium and Mouse WRN Conditioned Medium. This preparation was supplemented with EGF (50 ng/mL). Before media changes, 2D-MCM was freshly supplemented with Primocin (10 µg/mL) and Y27632 (10µM). Unlike 3D culture, monolayers were provided with fresh Y27632 for each media change.

### 3.4.6 2D-MCM Maintenance

2D-MCM changes were conducted every 1-2 days. Media changes were routinely scheduled, however, media color transitions from red to yellow would inform whether earlier changes were required. Unlike 3D-MCM, formulation of 2D-MCM did not vary based on circumstance. During typical media changes, 2D-MCM was always supplemented with Y27632.

## 3.5 MPA Exposure Experiments

MPA (Table 3.1) was prepared by dissolving 5 mg of MPA in 1mL of fresh methanol, yielding an initial stock concentration of 15.6084 mM. This stock solution was serially diluted with methanol to create a range of MPA stock solutions with the following concentrations: 15.61 mM, 7.80 mM, 3.90 mM, 1.95 mM, and 0.98 mM. To achieve the desired final MPA concentrations, 2.4 µL of each MPA stock solution was added to 297.6 µL of 2D-MCM to produce MPA working solutions at the following concentrations: 7.81 µM, 15.61 µM, 31.22 µM, 62.43 µM, and 124.87 µM. A vehicle control working solution was also prepared by adding 2.4 µL of methanol to 297.6 µL of 2D-MCM.

Colonoid monolayers were plated and cultured to confluence as outlined in section 3.4.3. For MPA exposure, 300 µL of each MPA working solution was added to the apical compartment of the trans-well inserts. For the vehicle control condition, 300 µL of the vehicle control solution was added to the apical compartment. Monolayers were incubated over 24 hours (37°C, 5% $CO_2$). The barrier function of the monolayers was assessed by measuring TER at 0 hours (immediately before MPA exposure), 12 hours, and 24 hours-post exposure. TER measurements were taken as outlined in section 3.6. TER values were compared across the different treatment conditions to assess the effect of MPA on monolayer integrity. Changes in TER were calculated relative to the baseline measurement as described in section 3.6.

## 3.6 Transepithelial Resistance Measurements

Colonoid monolayers were assessed for confluency and barrier function using an epithelial voltohmmeter and chopstick electrodes (Table 3.3). First, voltohmmeter electrodes were sterilized in a 50mL tube containing 25mL of 70% ethanol for 5-10 minutes. Next, the electrodes

were placed into a 50mL tube containing 20 mL of sterile PBS. The electrodes were swirled to remove excess ethanol. The electrodes were then transferred into 20 mL of HBSS (Table 3.1). Here, the electrodes were plugged into the epithelial voltohmmeter, and three baseline TER measurements were collected in Ω. These values were averaged and recorded for later reference. The electrodes were then moved to a final tube containing 15 mL of ADF. Again, three baseline measurements were averaged and recorded.

24-well plates (Table 3.1) containing colonoid monolayers inserts were removed from the incubator and transferred into the biosafety cabinet for TER measurement. Voltohmmeter electrodes were placed into each trans-well insert. The shorter end of the electrode was placed on the inside of the trans-well insert (apical compartment). The longer end of the electrode remained outside and was held against the bottom of the plate well (basolateral compartment) at a 90° angle. For each insert, three different measurements were taken (2, 6, and 10 o'clock positions). The three measurements were recorded and averaged to provide a single TER value for later comparison. This process was repeated for each monolayer insert.

TER measurement of monolayers treated with various experimental conditions were handled differently. In short, all monolayers of the same treatment conditions were measured as outlined above. When transitioning to monolayers of different treatment conditions, the voltohmmeter electrodes were briefly re-sterilized in a separate tube containing fresh 70% ethanol. The electrodes were then washed in PBS and placed back into the original tube containing ADF. This process was conducted to prevent cross-contamination of the different treatment conditions. Upon completion, the voltohmmeter electrodes were washed in the separate 70% ethanol tube using a swirling motion (20-30 seconds). After washing the electrodes, they were placed back into the original 25 mL of 70% ethanol and left to sterilize for

5-10 minutes. After sterilization, the electrodes were sprayed with freshly filtered 70% ethanol and dried before being placed back into storage.

TER measurements were recorded using Microsoft Excel software. Averaged TER measurements were multiplied by the culture surface area (0.336 $cm^2$) of the inserts to obtain a value expressed in Ω·cm². To omit background resistance from the Matrigel treated trans-well inserts, blank measurements were collected as outlined in section 3.4.1. Blank measurements were subtracted from the averaged monolayer measurements to calculate TER of the monolayers themselves. In this thesis, changes in monolayer TER are presented as mean resistance change (%). To calculate this, averaged measurements for each monolayer were collected at time 0 as a reference value. At each experimental timepoint, TER measurements were collected as described above. Measurements taken at each timepoint were then compared to the reference values as a percentage of change. For example, if a measurement of 600 Ω was collected at 24 hours, and a value of 1000 Ω at 0 hours, then the calculated change in resistance would be expressed as -40% ($\frac{24\ Hours - 0\ hours}{0\ hours}\ x\ 100\%$).

## 3.7 Immunofluorescence of Primary Mouse Colonoid Monolayers

Colonoid monolayer morphology and tight junction dynamics were visualized using confocal microscopy (Table 3.3). First, 2D-MCM was gently aspirated from the apical and basolateral compartments of monolayers. The monolayers were washed with 500 µL of PBS (3 x 5 minutes) After the final wash, PBS was aspirated, and the apical compartment of monolayers was fixed with 200 µL of 4% PFA (Table 3.1) for 15 minutes. After fixation, PFA was gently aspirated, and the monolayers were again washed with PBS (3 x 5 minutes). After washing, 500 µL of fresh PBS was added to each insert. The monolayers were stored at 4°C for 24 hours before staining.

To permeabilize the cells, the apical compartment was aspirated and incubated with 200 µL of 0.2% TritonX/PBS (Table 3.1) for 15 minutes at RT. Following this, TritonX/PBS was removed, and the apical compartment was washed with 200 µL of 0.2% Tween-20/PBS (Table 3.1) (3 x 5 minutes). Non-specific binding sites were then blocked by incubating the apical compartment of monolayers with 200 µL of 5% BSA/PBS (Table 3.1) for 1 hour at RT. The block solution was then aspirated, and the apical compartment of monolayers was incubated with 200 µL of primary ZO-1 antibodies (Table 3.1) diluted 1:200 in 5% BSA/PBS overnight. The following day, the primary antibody solution was aspirated, and the apical compartment was washed with 200 µL of 0.2% Tween-20/PBS 3x for 5 minutes at RT. After aspirating, the monolayers were incubated with 200 µL of secondary antibodies (Table 3.1) diluted 1:500 in 5% BSA/PBS for 1 hour in the dark at RT. Following incubation, the cells were washed with 200 µL of 0.2% Tween-20/PBS 3x for 5 minutes at RT. To visualize nuclei, the monolayers were counterstained with 200 µL of DAPI/PBS (Table 3.1), diluted 1:50,000, for 30 minutes in the dark at RT. DAPI was then aspirated, and the apical compartment of the monolayers was washed with 200 µL of PBS (3 x 5 minutes) at RT. The membranes of the trans-well inserts were cautiously removed using a razor and mounted apical side up on a coverslip. The prepared coverslips were stored at 4°C until imaging.

Note: two variations of staining were conducted in this thesis. Primary and secondary antibody staining (Alexa Fluor™ 488; Table 3.1) was used during initial monolayer visualization. Direct fluorescent staining using fluorescently conjugated ZO-1 monoclonal antibodies (Alexa Fluor™ 555; Table 3.1) was utilized in later analyses.

## 3.8 FITC-Dextran Permeability Assay

FITC-dextran permeability assays were conducted in conjunction with MPA exposure experiments as outlined in section 3.5. To start, a stock solution of 4 kDa FITC-dextran (Table 3.1) was prepared at a concentration of 10 mg/mL in PBS. The stock solution was diluted to a final working concentration of 100 μg/mL, which was achieved by adding the stock solution to 2D-MCM at a ratio of 1 uL per 1 mL of media.

First, the FITC-dextran solution (100 μg/mL) was added to the apical compartment of the trans-well inserts. After a 24-hour incubation period (37°C, 5% $CO_2$), both apical and basolateral media were collected. The collected media was transferred to a black 96-well microplate for fluorescence measurement. Each sample was measured in duplicate. Fluorescence intensity was measured using a microplate reader (Table 3.3) with excitation and emission wavelengths of 490 nm and 520 nm, respectively. Fluorescence readings were collected using Softmax Pro 7 software. Measurements from the basolateral compartment (bottom chamber) were compared to those from the apical compartment (top chamber) to determine the extent of FITC-dextran flux. Relative Fluorescent Units (RFUs) were used to quantify the amount of FITC-dextran that passed through the monolayer.

## 3.9 Cytokine and Chemokine Analysis

Cytokine and chemokine analysis was performed in monolayers following MPA exposure as described in section 3.5. After 24 hours of MPA treatment, media from both the apical and basolateral compartments of monolayers was collected. To ensure sufficient sample volume, media from monolayers within the same treatment condition were pooled. The pooled samples were immediately frozen at -80°C for storage. Frozen samples were shipped on dry ice to Eve

Technologies in Calgary, Alberta for multiplex cytokine and chemokine analysis. The samples were analyzed using the Mouse Cytokine/Chemokine 32-Plex Discovery Assay ® Array. Results were returned in the form of concentration values (pg/mL) for each of the 32 tested cytokines and chemokines.

## 3.10 Total RNA Sequencing

Total RNA was extracted from colonoid monolayers using Qiagen's RNeasy kit (Table 3.1), following the manufacturers guidelines. Total RNA extracts were pooled from 4 replicate monolayers of the same treatment condition (Vehicle control, 7.81 µM MPA, 15.61 µM MPA, and 31.22 µM MPA). RNA concentration and quality was measured using Nanodrop 2000 (Table 3.3) before submission to the Centre for Health Genomics and Information (CHGI) at the University of Calgary. RNA sequencing was conducted by the CHGI. NEB Ultra II RNA directional library preparation kit with rRNA depletion was used for library preparation, followed by sequencing on a NovaSeq S2 platform (Table 3.3) using a 100-cycle paired-end (2x50bp) configuration for at least 50M read pairs per sample. Initial quality assessment of the raw sequencing data was performed using FastQC software (version 0.12.1)[81].

Total RNA-seq data was processed using the usegalaxy.eu platform. Adapter trimming and filtering were carried out using FastP to remove low-quality reads and adapters. Cleaned reads were then aligned to the mouse comprehensive gene annotation M35 (GRCm39) from GENCODE and quantified using Salmon. The resulting quantification files were used as input for subsequent differential expression analysis in Rstudio version 2023.03.0 (Boston, MA: Posit Software). Differential expression analysis was conducted using DESeq2 in Rstudio. $Log_2$ fold change values and false discovery rates (FDR) were calculated to assess the magnitude and

significance of the expression changes. Expression data was visualized using the ‘pheatmap’ and ‘Enhancedvolcano’ functions in Rstudio. A list of differentially expressed genes (DEGs) was obtained through Rstudio differential expression analysis. A list of DEGs, along with their associated $Log_2$ fold changes and FDRs, was uploaded to Ingenuity Pathway Analysis (IPA, Qiagen, Redwood City, CA, USA, version 111725566) software. In IPA DEGs were filtered using a FDR $\leq 0.05$ and a $Log_2$ fold change $\geq |1|$. Filtered DEGs and their associated pathways were assessed using IPA’s integrated prediction algorithms and toolsets.

## 3.11 Guanosine Supplementation

### 3.11.1 Guanosine Supplementation in Colonoid Monolayers

Confluent colonoid monolayers were established and treated with the following conditions: Vehicle control (methanol), 7.81 µM MPA, 7.81 µM MPA + 1 mM guanosine, and 1 mM guanosine. 7.81 µM MPA and vehicle control working solutions were prepared as outlined in section 3.5. For the guanosine-containing conditions, guanosine (Table 3.1) was dissolved in either the 7.81 µM MPA working solution or untreated 2D-MCM at a final concentration of 1 mM. 300 µL of each working solution (control, MPA, MPA + guanosine, and guanosine) was added to the apical compartment of colonoid monolayers. Monolayers were then incubated over 24 hours (37°C, 5% $CO_2$). TER was measured at 0 hours (immediately before treatment) and 24 hours post-treatment. TER measurements were conducted as outlined in section 3.6.

### 3.11.2 Guanosine Supplementation in 3D Colonoid Cultures

3D colonoids were freshly passaged, plated in Matrigel domes, and treated with the following conditions: Vehicle control (methanol), 7.81 µM MPA, 7.81 µM MPA + 1 mM guanosine, and 1 mM guanosine. 7.81 µM MPA and vehicle control working solutions were prepared according to

a modified version of the procedure outlined in section 3.5. In this modified version, MPA and methanol were added to 3D-MCM instead of 2D-MCM, at the same final concentrations. For the guanosine-containing conditions, guanosine was dissolved in either the 7.81 µM MPA working solution or untreated 3D-MCM at a final concentration of 1 mM. 500 uL of each working solution (control, MPA, MPA + guanosine, and guanosine) was added to wells containing 3D colonoid Matrigel domes. Imaging of the 3D colonoids was conducted at 0 hours (immediately after plating), 24 hours, and 48 hours using bright-field microscopy. Images were analyzed using CellProfiler software to quantify colonoid growth.

## 3.12 Statistical Analysis

Statistical analyses were performed using GraphPad Prism version 8.0.2 (San Diego, CA: GraphPad Software) and Rstudio version 2023.03.0 (Boston, MA: Posit Software). Data are presented as means with error bars representing standard errors of the mean (SEM). Data were first assessed for normality using a Shaprio-Wilk test. Data passing normality testing were assessed parametrically through ordinary one-way Analysis of Variance (ANOVA) followed by Tukey's *post-hoc* multiple comparisons test. Data that were not normally distributed were assessed through a Kruskal Wallis test followed by Dunn's *post-hoc* multiple comparisons test. Sample size abbreviated as 'n' in the description of each figure represents the number of individual monolayers used for each treatment condition. Monolayers were cultured, measured, and treated independently of one another; therefore, each monolayer was considered a separate biological sample in this thesis.

# 4.1 RESULTS

## 4.2 Establishment of Primary Mouse Colonoid Culture

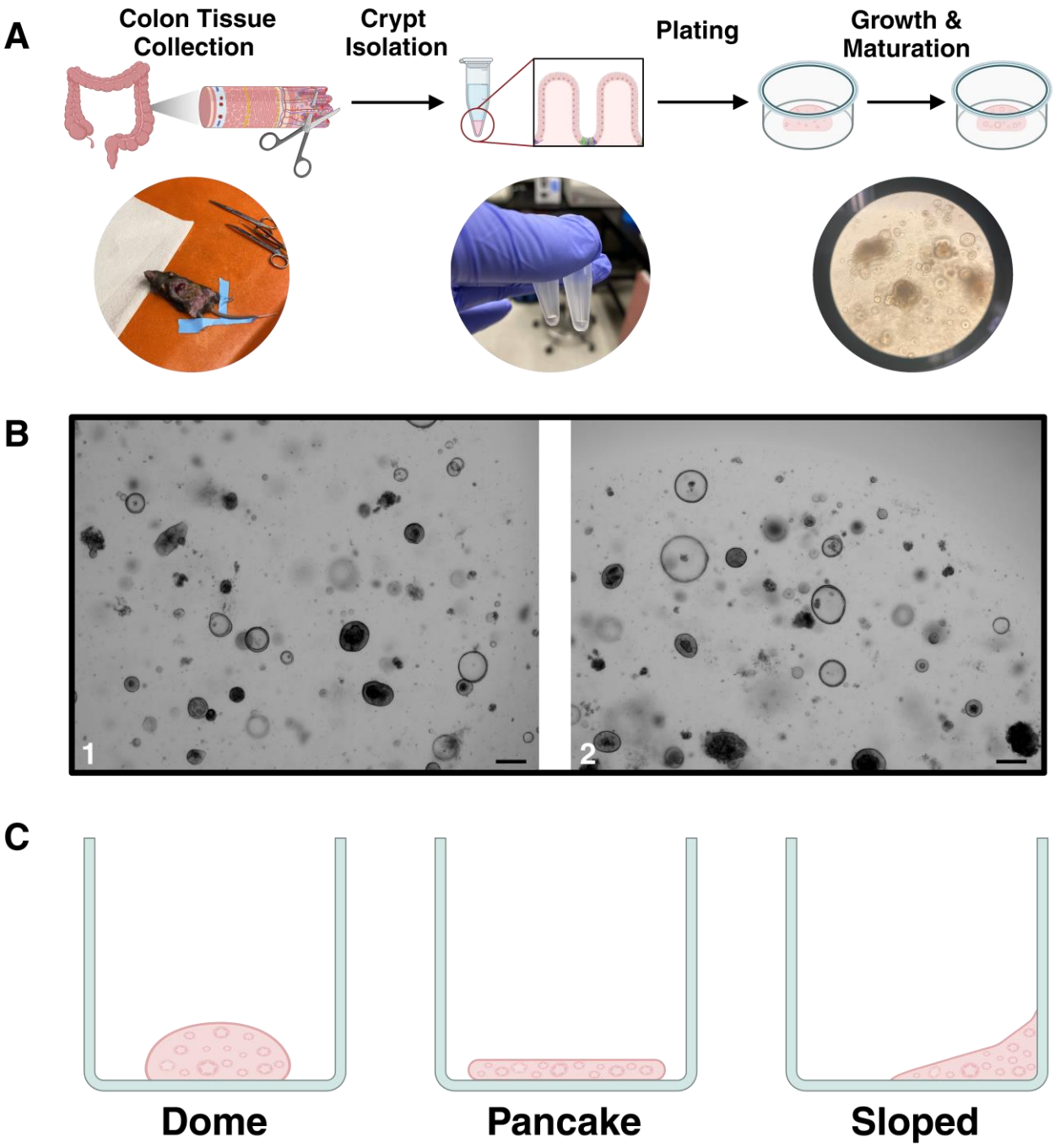


**Figure 4.1** Illustration depicting the workflow for establishing 3D colon organoids derived from C57BL/6 mice. (A) Simplified step-by-step process of generating primary mouse colon organoids. First, a colon sample is collected to obtain suitable colon tissue for subsequent

digestion and colonic crypt isolation. Once isolated, the crypt/stem cell suspension is pelleted, collected, and embedded into Matrigel domes. Within 4-6 days, the isolated crypts/stem cells proliferate and self-organize to form complex structures recapitulating the physiology of the tissue it was derived from. (B) Daily monitoring of colonoid cultures using bright-field microscopy. (B1) Colonoids on day 1 of passage 6, showcasing early-stage development. (B2) Colonoids on day 2 of passage 6, demonstrating slight growth and morphological changes. (C) Illustration demonstrating different Matrigel formations that occurred during the plating process. All scale bars represent 100 µm. *Created with BioRender.com*

### 4.2.1 Methodological Adaptions and Colonoid Culturing

Colon organoid cultures were generated using an adapted version of an established protocol from the HOIH at the University of Calgary (Figure 4.1 A). To establish and maintain colonoid cultures, a 3D specific L-WRN (Wnt3a, R spondin 3, Noggin) conditioned medium produced by the HOIH was utilized (Figure 4.2 A and Table 3.2). Monitoring the cultures and changing media timely were critical to adequately support the growth and maturation of the organoids. Typically, media changes were conducted every 48 hours, with alterations occurring with variations in colonoid density. During crypt isolation and plating, approximately 250-600 colon crypts were embedded in each Matrigel dome to establish quality cultures. The collection of one colon sample typically yielded an average of 5-7 Matrigel domes.

### 4.2.2 Colonoid Monitoring and Maturation

Organoid cultures were monitored daily using bright-field microscopy at various magnifications (4x, 10x, 20x, 40x) (Figure 4.1 B). Assessment of the cultures included evaluation of the Matrigel domes serving as the scaffold for growth. During plating, colonoids were suspended in Matrigel and incubated upside down to promote the formation of 3D hemispherical domelike structures (Figure 3.1 C). During the plating process, a low failure rate was observed in the formation of Matrigel domes. Failure led to the formation of “pancake” or “sloped” Matrigel

structures (Figure 3.1 C). Visual observation of colonoids in malformed Matrigel scaffolds indicated decreased growth and quality, deeming these cultures unsuitable for future passaging and experimentation. Low quality Matrigel scaffolds were marked and subsequently discarded to ensure consistency.

During monitoring, images of colonoids were captured and digitally recorded to track culture consistency and quality. Evaluation of organoid growth and maturation was utilized to inform scheduled passaging and monolayer generation. To ensure successful high-quality culture generation, passaging was typically performed every 4-6 days. Colonoid cultures suitable for passaging were primarily determined by the presence of cellular debris buildup. Specifically, colonoids were considered ready for passaging once the central lumens exhibited dark black masses, indicative of cellular debris accumulation (Figure 4.2 C). Assessment of colonoid maturity based on morphological changes also influenced routine passaging timelines. For instance, the emergence of budding around day 4 (Figure 4.2 panels A and B) signaled that passaging would be required within the next 24-48 hours to maintain culture quality. Failure to passage timely lead to noticeable increases in cellular debris buildup (Figure 4.3 G) and widespread cell death, subsequently diminishing overall culture quality and delaying monolayer generation.

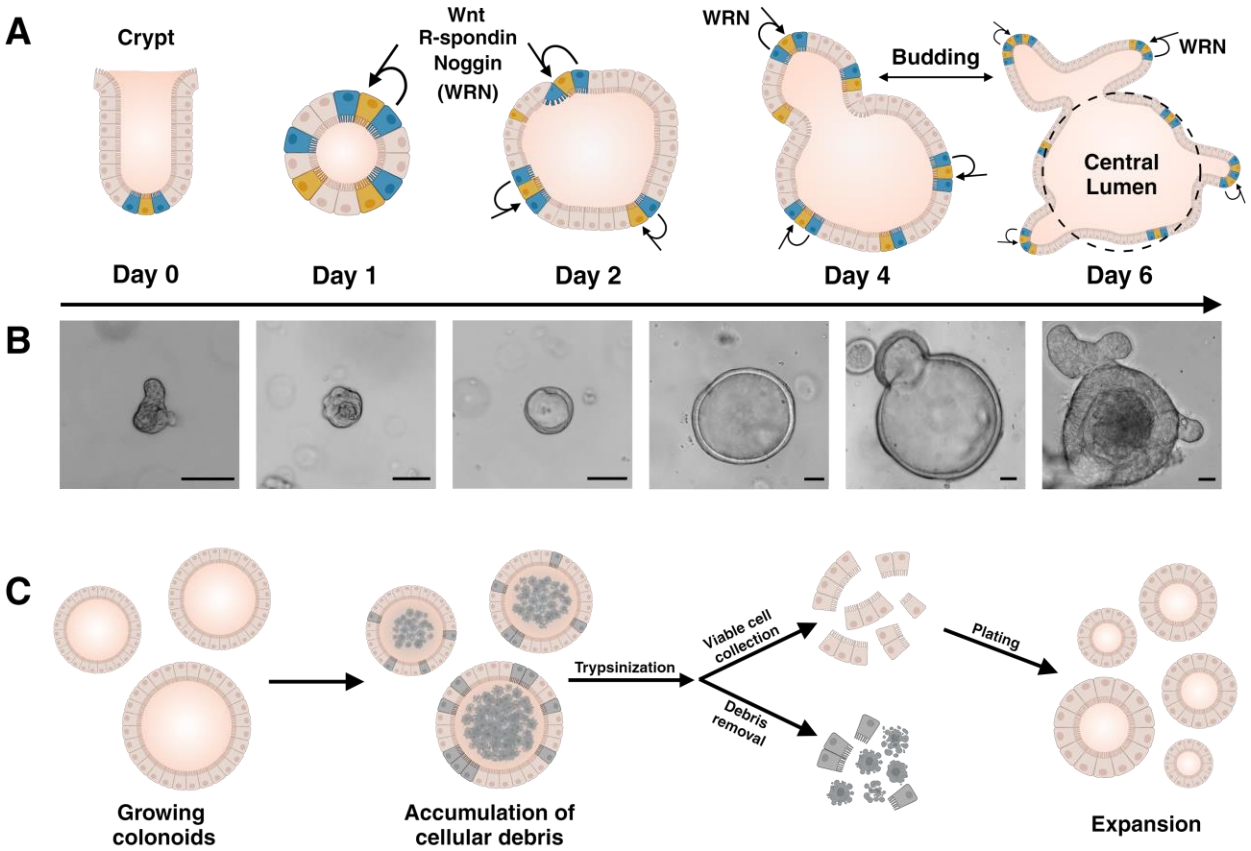


**Figure 4.2** Illustrative summary of colonoid growth, maturation and splitting. (A) Graphic visualization illustrating organoid maturation through progressive morphological changes in mouse colonoids over a 6-day period. Starting from an isolated crypt, intestinal stem cells (yellow) proliferate to produce progeny that self-organize into complex budded structures. Paneth cells (blue) produce Wnt3a and other signaling factors that support the crypt stem cell niche and promote proliferation[1]. Additional factors (Wnt3a, R spondin 3, and Noggin) promoting proliferation and undifferentiation of crypt stem cells are present in the provided 3D-MCM, stimulating sustained growth and budding of the colonoids. (B) Bright-field microscopy images demonstrating real-time visual evidence of colonoid development corresponding to the above stages in A. Images range from an isolated crypt to a late stage budding organoid with a distinct central lumen filled with cellular debris. (C) Illustration demonstrating how cellular debris buildup helps gauge colonoid passaging. During passaging, colonoids are trypsinized (dissociated) into fragments and debris is removed. Viable cells are resuspended in Matrigel and plated for expansion. Scale bars annotated in black represent a scale of 50 µm. *Created with BioRender.com*

### 4.2.3 Colonoid Culture Characterization

During routine monitoring, various characteristics were noted and recorded to maintain conditions for consistent organoid quality and growth. Circular organoids with unobstructed "open" central lumens (Figure 4.3 A) were indicative of desirable culture conditions. Observations of small deposits of cellular debris within the central lumen were classified as normal growth patterns, indicating healthy proliferation. The "open" characteristic was the most prevalent feature among colonoid cultures, representing a majority of the observed colonoids.

Closed colonoids were characterized by enclosed cyst-like structures. Closed colonoids possess an interior central lumen; however, accessibility to the lumen is obscured by the presence of epithelial cell layers (Figure 4.3 B). These organoids symbolized immature colonoid development, signifying the early stages of proliferation and cavitation processes. Interestingly, some colonoids remained closed depending on the intrinsic growth patterns of the cells forming the organoid, and by modulation by the culture environment. Nevertheless, continuous observations of growth suggested that most closed colonoids transitioned into larger "open" structures.

High density colonoid culture was determined primarily though qualitative visual assessment using bright-field microscopy. High density was characterized by the presence of numerous overlapping and closely arranged organoids as highlighted in Figure 4.3 panel C. High density culture was also notable through temporal changes in media coloration due to larger pH changes in comparison to lower density culture. Higher densities of colonoids were observed to expel waste at a greater rate leading to noticeable reductions in pH. Increased waste excretion between culture densities was distinguished through media color transitions from red/pink to yellow

(Figure 4.4). Yellow coloration was indicative of depleted media/low pH, prompting immediate action to maintain desirable culture conditions for optimal organoid health and growth. Counter to high density culture was low density, which was characterized by sparse organoid presence as shown in Figure 4.3 D. Similarly to high density culture, low density culture was ascertained through visual analysis using bright-field microscopy. Low density culture was deemed less suitable for monolayer generation, as successful monolayer plating required the isolation of millions of cells, which proved difficult with lower density cultures.

Colonoid culture environment was also categorized by the overall “cleanliness”. Clean culture was defined by the absence of exogenous materials such as fibrous materials and microplastics as illustrated in Figure 4.3 E. Clean characteristics implied higher quality culture conditions as the presence of exogenous materials may induce detrimental effects on organoid growth, introducing unexpected variations during experimentation. Dirty culture conditions were also observed, as depicted in Figure 4.3 F. Dirty conditions were distinguished by the presence of exogenous fibers and microplastics. Dirty Matrigel domes were considered poor quality and were marked and subsequently discarded to reduce re-introduction of unwanted materials during passaging and monolayer generation.

The presence of cellular debris was a primary factor dictating colonoid culture maintenance regime. High debris was characterized by the accumulation of cellular debris both within the luminal cavity of the organoids and within the surrounding Matrigel matrix. High levels of debris accumulation were discriminated through visual analysis using bright-field microscopy. Significant debris accumulation was classified by the presence of dark spots as shown in Figure 4.3 G. Significant debris buildup was indicative of worsening culture conditions, prompting immediate action within the next 24 hours. Low debris was characterized by the absence of

debris buildup. The lack of debris accumulation indicated that colonoid culture conditions were optimal and that passaging was not yet required.

As mentioned previously, consistent monitoring and maintenance of the growth media was key to establish high quality colonoids. Growth media depleted of resources prevents colonoids from acquiring key resources fundamental for consistent growth and development. Additionally, low pH conditions were observed to induce cell death and diminish growth. Figure 4.3 panel I illustrates the outcome of colonoids being left in depleted/low pH media for an extended period. Typical consequences present as mass cell death and significant debris accumulation. Such cultures were deemed unacceptable for passaging and monolayer generation and were discarded.

Biological contaminates were also observed in colonoid cultures as shown in Figure 4.3 J. Cultures were consistently examined for the presence of contamination. Contamination was characterized by the presence of unwanted biological specimens such as fibroblasts or bacterial cultures. Contamination was ascertained through various ways, such as bright-field microscopy, visual analysis of media coloration, and widespread culture death. In the presence of bacterial contamination, supplied media would transition to yellow much quicker than expected when colonoid density was taken into consideration. When yellowing of the media occurred suddenly, cultures were immediately examined for the presence of contaminants. Significant bacterial contamination as highlighted in Figure 4.3 J panel 1, was first identified visually without a microscope, presenting as prominent yellow colonies in the Matrigel matrix. Fibroblast contamination was also observed (Figure 4.3 J panel 2) and was initially discovered through unexpected changes in media coloration. Cultures with contamination were bleached and appropriately discarded to avoid contamination spread. Additional measures such as environmental sterilization was also conducted to prevent spread. Following identification of

contamination, all colonoid plates were extensively examined to detect unwanted contamination spread. Extensive monitoring was maintained for several days following contamination to ensure healthy culture conditions.

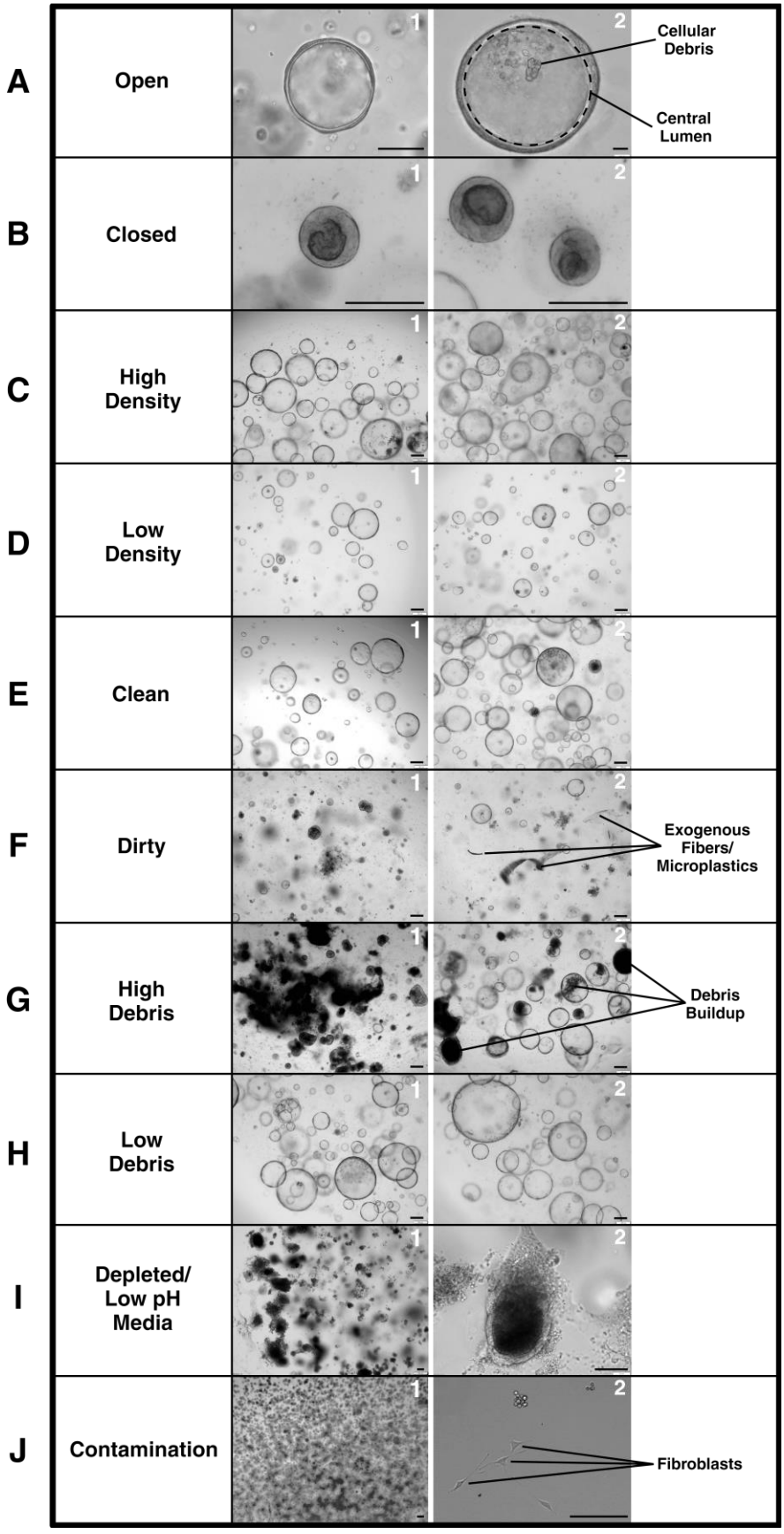
A
Open
Cellular Debris
Central Lumen
B
Closed
C
High Density
D
Low Density
E
Clean
F
Dirty
Exogenous Fibers/ Microplastics
G
High Debris
Debris Buildup
H
Low Debris
I
Depleted/ Low pH Media
J
Contamination
Fibroblasts

**Figure 4.3** Bright-field microscopy images demonstrating different characteristics of colonoid culture, illustrating a range of conditions and organoid morphology. (A) Open colonoid characteristic. (B) Closed colonoid characteristic. (C) High density organoid culture. (D) Low density organoid culture. (E) Clean culture conditions. (F) Dirty culture conditions. (G) High accumulation of cellular debris. (H) Low accumulation of cellular debris. (I) Colonoids left in depleted/low pH media for an extended period. (J) Presence of biological contaminates in colonoid culture. Each row represents a desirable or undesirable trait critical for assessing quality and determining readiness for passaging and monolayer generation. Each characteristic has two representative images to highlight variability across different passages and stages of growth. Black scale bars represent 100µm. *Created with BioRender.com*

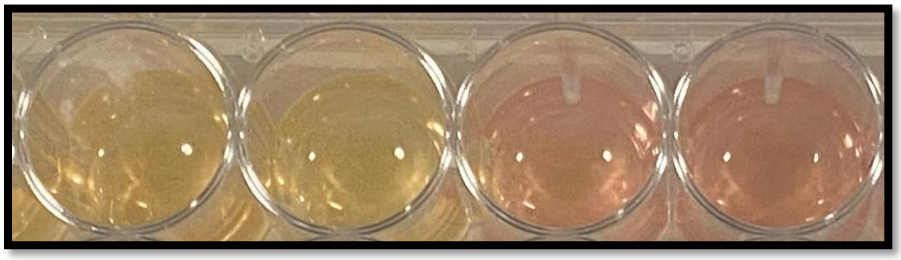

**Figure 4.4** Digital image showing coloration changes in 3D-MCM. Cells expel acidic waste products such as lactic acid and carbon dioxide as they metabolize nutrients in the medium. pH indicators change color corresponding to changes in the pH. When the media becomes more acidic the media transitions to a yellow color. At a neutral pH (≈ 7.4) the medium appears red/pink. Observing shifts in color was used to inform timely media changes.

## 4.3 Establishment of Primary Mouse Colonoid Monolayers

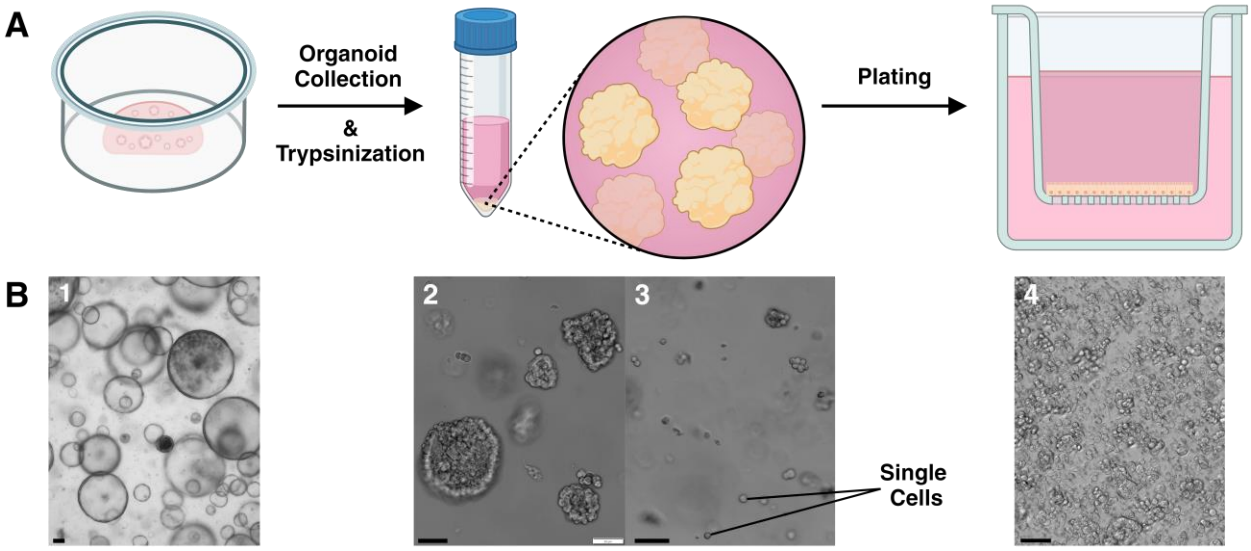


**Figure 4.5** Illustration depicting the workflow for establishing 2D colonoid monolayers from 3D primary mouse colon organoids. (A) Simplified step-by-step process of generating primary mouse colon organoid monolayers. First, 3D colonoids are grown to 4-6 days of maturity to obtain suitable organoids for subsequent digestion and crypt stem cell isolation. Once isolated, the cell suspension is pelleted, collected, and uniformly plated onto the porous membrane of trans-well inserts pre-incubated with Matrigel. Within 1-2 weeks, the isolated cells proliferate to form a confluent monolayer recapitulating the polarized physiology of the colon tissue it was derived from. (B panel 1) Representative bright-field images of 3D colonoids ready for processing into monolayers. (B panel 2) Organoids displaying early-stage trypsin digestion. (B panel 3) Organoids demonstrating late-stage trypsin digestion. (B panel 4) Bright-field image showcasing uniform plating of dissociated colonoids on the porous membrane of a trans-well insert. Black scale bars represent 50 µm. *Created with BioRender.com*

### 4.3.1 Methodological Adaptions and Colonoid Monolayer Culturing

Colonoid monolayers were generated using an adapted version of an established protocol from the HOIH at the University of Calgary (Figure 4.5 A). To establish and maintain colonoid monolayers, a 2D specific L-WRN conditioned medium produced by the HOIH was utilized (Table 3.2). Like the 3D colonoid cultures, daily monitoring and changing media timely were

critical to adequately support monolayer growth to confluency. Media changes were normally conducted every 48 hours, with alterations occurring during the initial plating process, in which a media change was conducted 24 hours after. When plating, a single cell count between $0.8 \cdot 10^6$ - $1 \cdot 10^6$ /mL was required to uniformly cover the porous membrane of the trans-well inserts (Figure 4.5 B panel 4). Uniform plating was observed to generate monolayers of high quality, reaching confluency within 7-14 days.

### 4.3.2 Colonoid Monolayer Monitoring and Confluency

Monolayers were also monitored daily using bright-field microscopy at various magnifications (4x, 10x, 20x, 40x). Routine visual assessment included evaluation of both the basolateral and apical chambers to ensure quality culture conditions. To track monolayer growth, TER measurements were taken every 2-3 days, with higher frequency 7-9 days after initial plating. TER measurements above 235 $\Omega \cdot cm^2$ indicated that monolayers had reached confluency, and TER values below 235 $\Omega \cdot cm^2$ suggested non-confluency. To supplement TER measurements, monolayers were also assessed by their ability to hold back liquid. To do this, 2D-MCM was added only to the apical compartment of the trans-well inserts. Flow of 2D-MCM across the monolayer was observed over 1-2 hours. If little to no liquid passed through the monolayer into the basolateral compartment, confidence in confluency was maintained. Unlike 3D colonoid culture, colonoid monolayers were not routinely passaged. Once confluency was determined, monolayers were prepared for experimentation. If left for too long, monolayers would exhibit substantial increases in TER, alluding to the formation of a bilayer, differentiation, or other undesirable characteristics such as the formation of 3D structures. Therefore, confluent monolayers were immediately used for experimentation to avoid introduction of extraneous variables.

### 4.3.3 Colonoid Monolayer Characterization

During routine monitoring, various characteristics were noted and recorded to maintain conditions for consistent monolayer quality and growth. Newly plated monolayers were observed to evaluate uniformity of the plated cells. Figure 4.6 A illustrates desirable plating uniformity and density. Monolayers demonstrating newly plated characteristics similar to Figure 4.6 A panels 1 and 2 were observed to produce clean confluent monolayers (Figure 4.6 D). To maintain consistency across monolayer generation, a dissociated colonoid cell suspension with a cell count between $0.8 \cdot 10^6$ - $1 \cdot 10^6$ /mL was used. Monolayers generated using a cell count lower than $0.8 \cdot 10^6$/mL (Figure 4.6 B) often did not reach confluence in an appropriate amount of time (within 7-14 days), with some monolayers not reaching confluency at all. Non-confluency was hard to determine visually since the thin layer of cells were difficult to distinguish against the background noise of the porous trans-well membrane (Figure 4.6 H). Monolayers generated using a cell count higher than $1 \cdot 10^6$ /mL, often demonstrated wide-spread cell death, leading to the accumulation of cellular debris (Figure 4.6 F) which was undesirable for barrier function analyses. Plating of poorly dissociated colonoids is depicted in Figure 4.6 G. Poorly trypsinized colonoids were observed to form 3D structures, rather than uniform monolayers (Figure 4.6 C). The presence of 3D structures produced inconsistent TER measurements and introduced undesirable characteristics for monolayer barrier function analyses. Monolayers with high prevalence of 3D structures were marked and subsequently discarded to ensure consistency across monolayer experiments.

Colonoid monolayers were also characterized by “cleanliness”. Clean culture was defined by the absence of exogenous materials such as fibrous materials and microplastics as illustrated in Figure 4.6 D. Clean characteristics were important for generation of high-quality monolayers

as the presence of exogenous materials may impact barrier function experiments by introducing gaps and TER measurement inconsistencies. Dirty monolayers were observed as depicted in Figure 4.6 E. Dirty conditions were distinguished by the presence of exogenous fibers and microplastics. Dirty monolayers were considered poor quality and were marked and subsequently discarded to maintain consistency.

Biological contaminates were also observed in colonoid monolayers as shown in Figure 4.6 I. Monolayers were consistently examined for the presence of contamination in both the apical and basolateral compartment. Contamination was characterized by the presence of unwanted biological specimens such as fibroblasts. Like the 3D colonoids, contamination was ascertained through various ways, such as bright-field microscopy monitoring, visual analysis of media coloration, and erratic changes in TER measurements. Fibroblast contamination was observed (Figure 4.6 I panels 1 and 2) and was initially discovered through unexpected changes in TER measurements. The presence of fibroblasts substantially increased TER measurements past values expected for confluent colonoid monolayers. Subsequent assessment using bright-field microscopy confirmed the existence of contamination. Contaminated monolayers were bleached and appropriately discarded to avoid contamination spread. A similar procedure as outlined in 4.2.3 was followed to reduce contamination spread and to ensure healthy culture conditions.

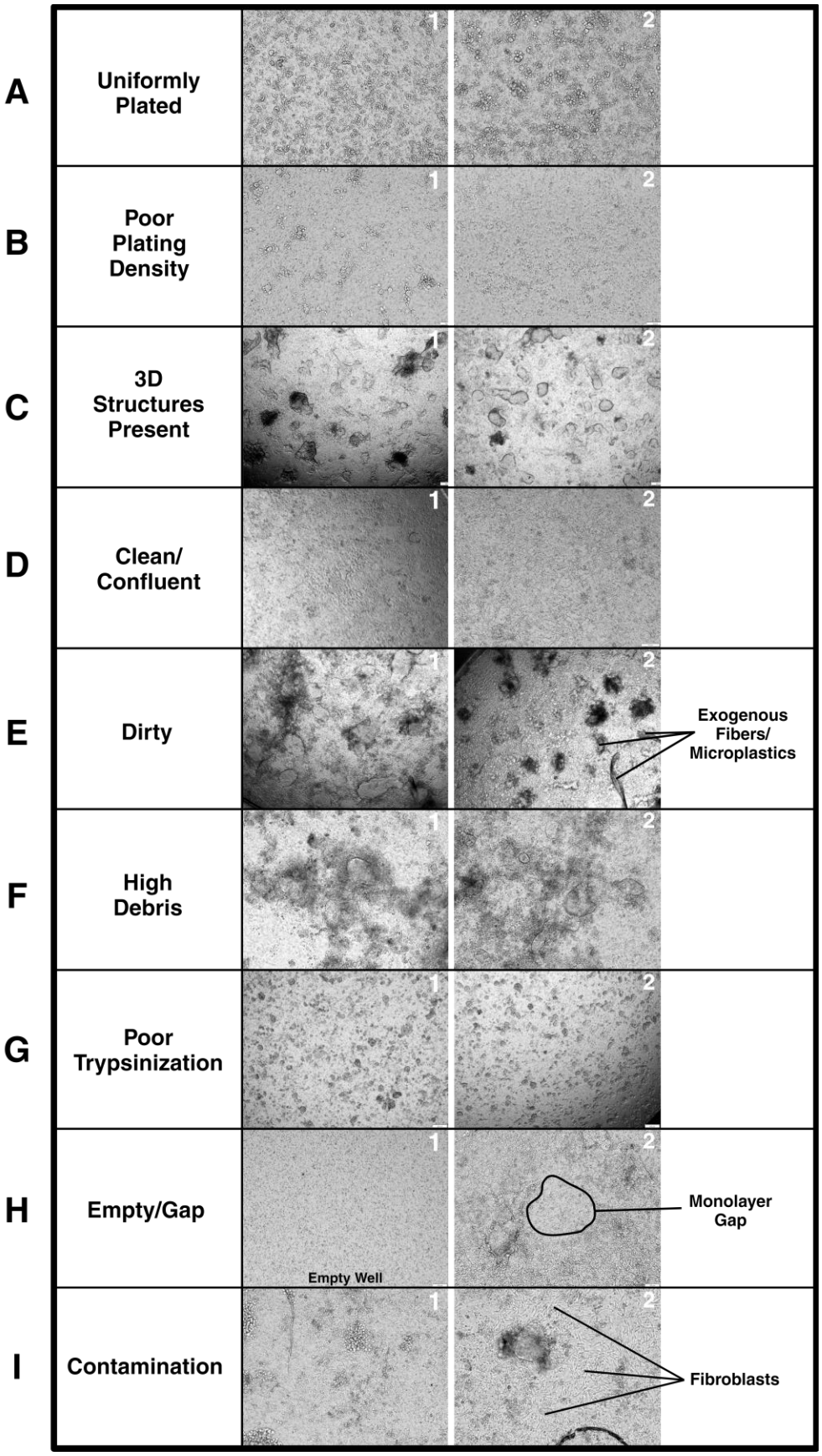
A
Uniformly Plated
B
Poor Plating Density
C
3D Structures Present
D
Clean/ Confluent
E
Dirty
Exogenous Fibers/ Microplastics
F
High Debris
G
Poor Trypsinization
H
Empty/Gap
Monolayer Gap
Empty Well
I
Contamination
Fibroblasts
1
2

**Figure 4.6** Bright-field microscopy images exhibiting different characteristics of colonoid monolayer culture, illustrating a range of culture conditions and monolayer morphology. (A) Freshly plated dissociated colonoids with uniform plating distribution. (B) Poorly plated monolayers, with low density of single cells. (C) Presence of 3D structures in monolayers. (D) Ideal monolayer characteristics, clean and confluent with no 3D structures present. (E) Dirty culture conditions with exogenous fibers/microplastics present. (F) High accumulation of cellular debris. (G) Poor dissociation of colonoids before monolayer plating with high prevalence of clumped cells. (H) Images illustrating the difficulty of determining confluency through bright-field microscopy. The porous membrane of trans-well inserts produces visual noise making it hard to distinguish the presence of gaps in growing monolayers. (I) Presence of biological contaminates in monolayer culture. These images display desirable and undesirable traits critical for assessing monolayer quality and determining readiness for experimentation. Each panel represents various passages and stages of growth. *Created with BioRender.com*

## 4.4 Validation of Primary Mouse Colonoid Monolayer Model and Identification of Suitable MPA Concentrations

### 4.4.1 Assessment of Colonoid Monolayer Confluency and Barrier Integrity

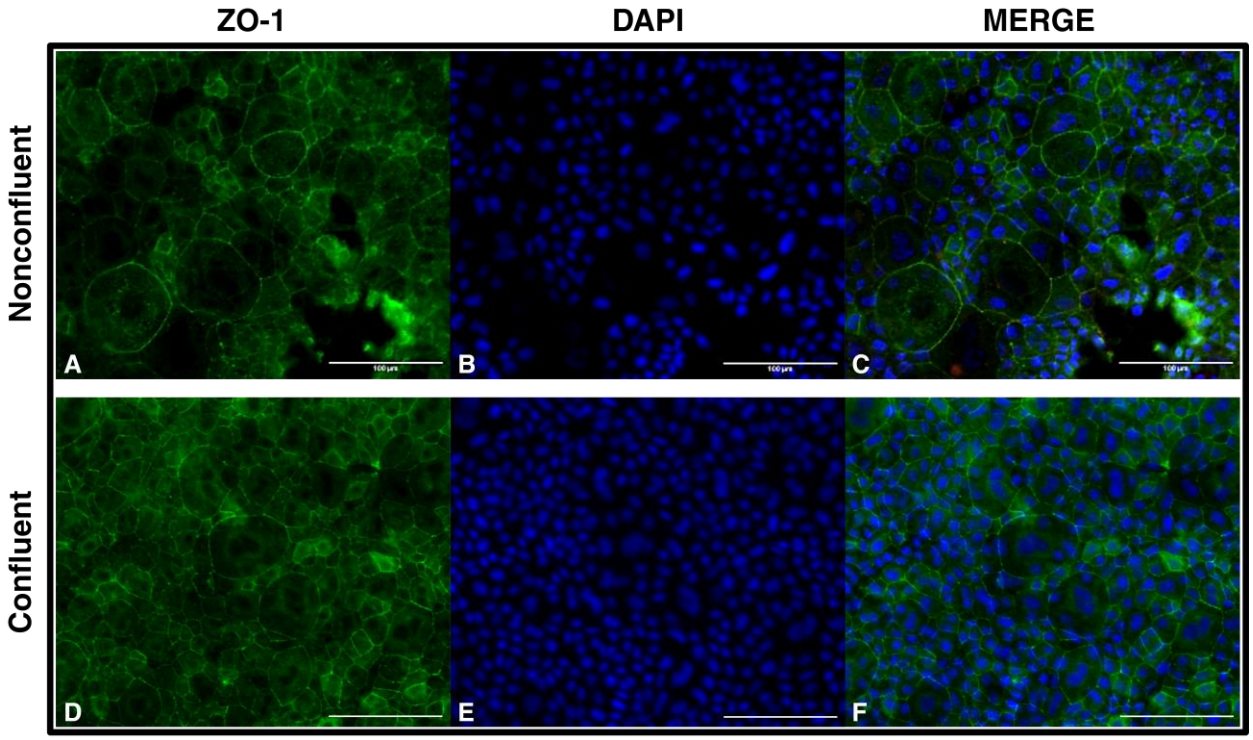


**Figure 4.7** Primary mouse colonoid monolayers fixed and stained for ZO-1 (green) and DAPI (blue) to visualize monolayer morphology and confluency. (A) ZO-1 stain of a non-confluent monolayer. (B) DAPI stain of a non-confluent monolayer. (C) Channel merge of ZO-1 and DAPI in non-confluent monolayer. (D) ZO-1 stain of a confluent monolayer. (E) DAPI stain of a confluent monolayer. (F) Channel merge of ZO-1 and DAPI in a confluent monolayer. Images were processed and merged using ImageJ. White scale bars represent 100 µm. *Created with BioRender.com*

To evaluate the established monolayer model, confocal microscopy was utilized to visually assess primary mouse colonoid monolayers. Categorization of the monolayers as non-confluent or confluent was established before imaging. Classifying monolayers as confluent/non-confluent was informed through TER measurements, and by the monolayers ability to prevent movement of liquid from the apical chamber to the basolateral chamber. Monolayers were deemed

confluent at TER values greater than 235 $\Omega \cdot cm^2$ and non-confluent at TER values below 235 $\Omega \cdot cm^2$. Confocal images illustrating confluent and non-confluent characteristics were saved to establish baseline references for future analyses.

ZO-1 staining in the non-confluent monolayer (Figure 4.7 A) demonstrates incomplete tight junction formation, with some regions displaying pronounced ZO-1 accumulation (green intensity). Noticeable gaps, particularly in the bottom right region of panel A indicate a lack of continuous cell-cell adhesion. DAPI staining in panel B depicts uneven distribution of cell nuclei with areas of increased sparsity, suggesting incomplete cell coverage. Notable in panel B is the absence of cell nuclei in specific regions correlating with the gaps observed in the ZO-1 staining. When merged (Figure 4.7 C), the ZO-1 and DAPI channels show that regions missing complete tight junction formation also lack corresponding nuclei in adjacent regions, reinforcing incomplete cell distribution. Together these results formed the reference characteristics for non-confluent monolayers.

Comparatively, in Figure 4.7 panel D, cell borders are clearly defined, with uniform ZO-1 organization along the cell periphery. The absence of fragmentation and irregularities indicates effective cell-cell adhesion, fully developed with intact tight junction integrity. DAPI staining in panel E further supports the notion that the cells have proliferated to form a continuous cell layer. High density and consistency of the nuclei correspond strongly with the ZO-1 staining, revealing the absence of gaps in the observed monolayer. When merged (Figure 4.7 panel F), the ZO-1 and DAPI channels show a well-structured continuous epithelial cell layer. Together these results formed the reference characteristics for confluent monolayers. These results indicate that TER measurements and the ability to hold back liquid represent valuable tools for determining monolayer confluency and suitability for barrier function analyses.

### 4.4.2 Investigating Various Mycophenolic Acid Concentrations on Transepithelial Resistance of Primary Mouse Colonoid Monolayers

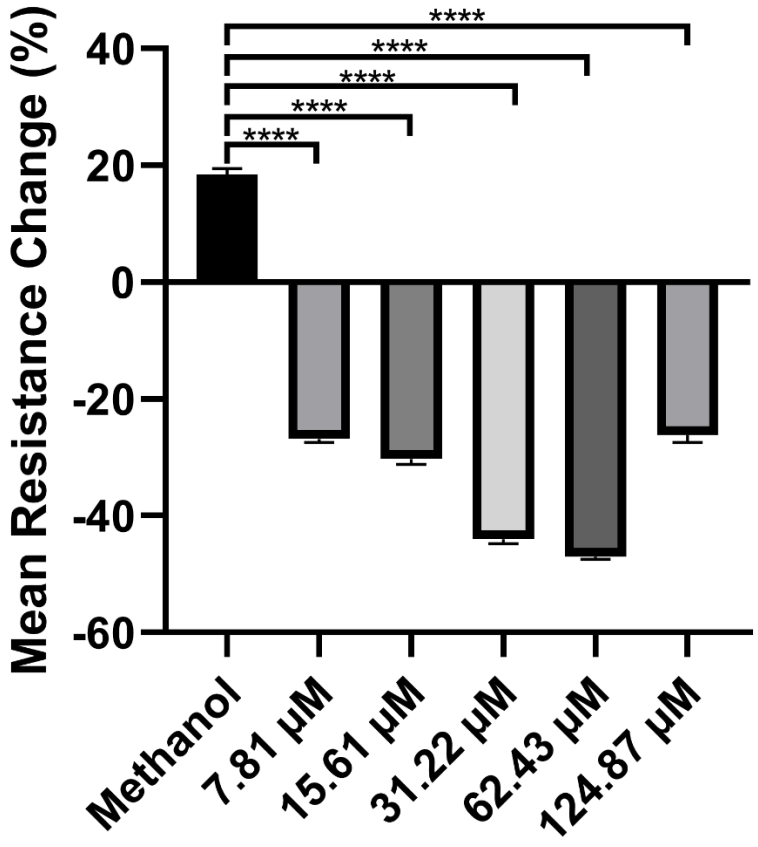


**Figure 4.8** Measurement of transepithelial resistance in primary mouse colonoid monolayers exposed to increasing concentrations of MPA and a vehicle control (methanol) over a 24-hour period. The y-axis corresponds to the mean percentage change in resistance compared to baseline measurements taken at time 0. Values represent mean ± SEM. Data passed Shapiro-Wilk test of normality and was assessed using a one-way ANOVA followed by Tukey's post-hoc test. All MPA treatments induced significant changes in monolayer resistance (**** $P < 0.0001$) compared to the control ($n = 3$).

The purpose of this study was twofold: to validate the applicability of the established colonoid monolayer model system and to identify physiological concentrations of MPA that would elicit strong, measurable effects on monolayer barrier function for further assessment. The study aimed to establish a baseline understanding of how various concentrations of MPA may affect intestinal

barrier function, thereby guiding future interpretations of the mechanisms underlying MPA-induced GI toxicity.

TER data was analyzed using an ordinary one-way ANOVA followed by Tukey's multiple comparisons. The above data (Figure 4.8) reveals a significant reduction in TER values following MPA exposure across all tested concentrations when compared to the methanol control group ($P < 0.0001$). Comparisons among the different concentrations in Figure 4.8 reveal that 7.81 µM MPA vs 31.22 and 62.43 µM MPA show significant differences ($P < 0.0001$). 15.61 µM MPA vs 31.22 and 62.43 µM MPA was also evaluated to show significance ($P < 0.0001$). Similarly, 31.22 µM MPA vs 124.87 µM MPA displayed statistical significance, ($P < 0.0001$). 62.43 µM MPA vs 124.87 µM MPA also exhibited significance ($P < 0.0001$). In contrast, 7.81 µM MPA vs 15.61 and 124.87 µM MPA showed no statistical significance ($P = 0.1220$ and 0.9922). Comparison between 15.61 µM MPA vs 124.87 µM MPA, did show weak statistical difference between groups ($P = 0.0490$). Analysis of 31.22 µM MPA vs 62.43 µM MPA showed no statistically significant difference ($P = 0.2252$).

These results validated the proposed colonoid monolayer model as a suitable system for studying the effects of MPA on intestinal barrier integrity. The outcome of this study informed the decision to focus on MPA concentrations 7.81 µM, 15.61 µM and 31.22 µM for future assessments.

## 4.5 Effects of MPA Exposure on Primary Mouse Colonoid Monolayers

### 4.5.1 MPA Exposure Induces Morphological Changes and Modulates Tight Junction Integrity

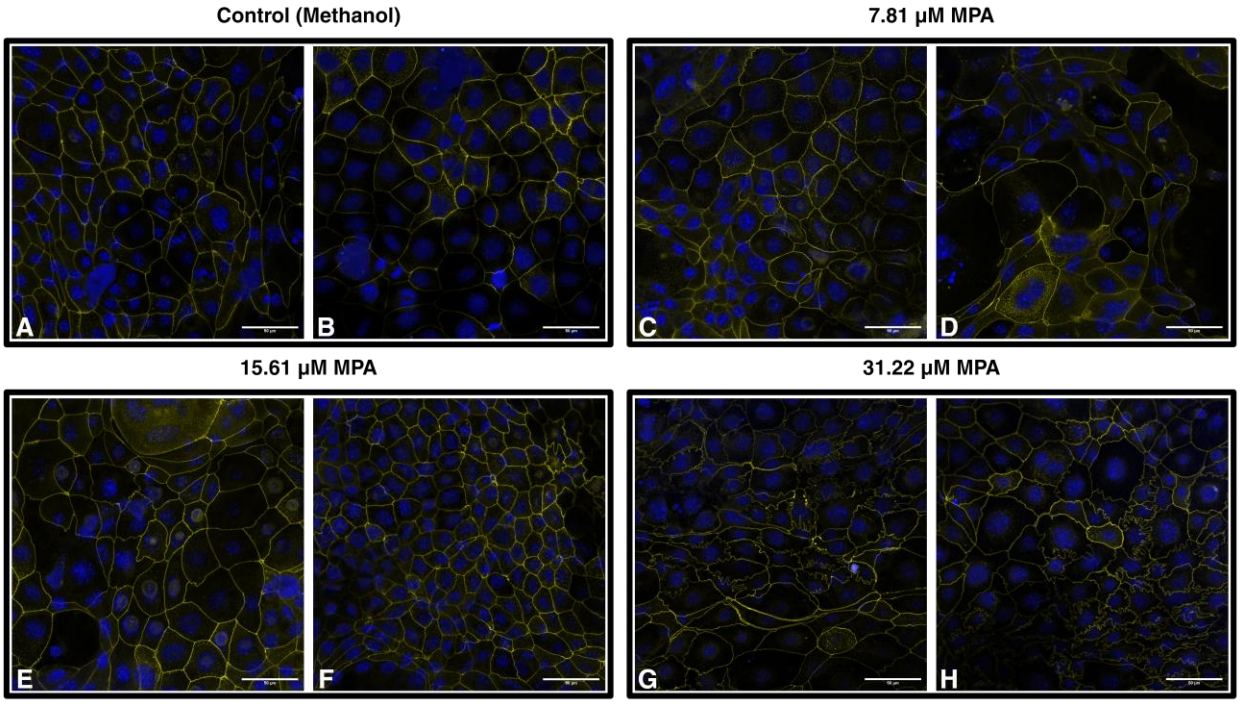


**Figure 4.9** Primary mouse colonoid monolayers fixed and stained for ZO-1 (yellow) and DAPI (blue) to visualize monolayer morphology and confluency after treatment with MPA and a vehicle control over a 24-hour period. Each treatment condition includes two representative images to highlight variability noted within each treatment. Images were processed and merged using ImageJ. White scale bars represent 50 µm. *Created with BioRender.com*

The purpose of this investigation was to examine the morphological changes and modulation of tight junction integrity in primary mouse colon organoid monolayers following exposure to MPA. The control group was treated with methanol. Monolayers were fixed and stained with fluorescently conjugated ZO-1 antibodies (yellow) to visualize tight junctions and DAPI (blue) to identify cell nuclei.

The control monolayers (Figure 4.9 panels A and B) displayed uniform, intact morphologies with well-defined, continuous ZO-1 staining along cell borders. Yellow puncta are

visible, showcasing tight junction dynamics within the cells. Notably, panel A does highlight the presence of slight elongation and irregularity which is not distinguished in panel B. DAPI staining in panels A and B show evenly distributed nuclei, indicating confluency with minimal disruption.

At the 7.81µM concentration (Figure 4.9 panels C and D) the monolayers appear to exhibit signs of early disruption. ZO-1 staining, while still continuous demonstrates increased irregularities and thinning in comparison to the control images, indicating slight tight junction modulation. Additionally, there is a marked increase in the presence of yellow puncta, further suggesting tight junction disruption and potential changes to tight junction dynamics within the cells. The increased presence of puncta is most notable in the bottom half of panel D. Overall morphology appears intact in panel C with an increased prevalence of "jagged" lines along cell borders. Panel D demonstrates states of elongation and deformations along the cell boundaries. DAPI staining remains evenly distributed, indicating that cell nuclei are still well organized despite morphological changes. Though, the lack of nuclei in panel D suggests that gaps exist in the monolayer.

Exposure to 15.61 µM MPA resulted in similarly pronounced morphological changes as 7.81 µM MPA (Figure 4.9 panels E and F). ZO-1 staining shows increased irregularity and distortion in comparison to the control, especially with the prevalence of "jagged" lines along cell borders. Most notable is the increased presence of yellow intensities encapsulating the cell nuclei, suggesting accumulation of ZO-1 proteins around the cell nucleus. DAPI staining appears less consistent, showing additional irregularities and gaps in comparison to the control.

The highest concentration tested, 31.22 µM MPA (Figure 4.9 panels G and H) exhibits substantial morphological disruption. ZO-1 staining shows severe irregularities and distortion along cell borders. Though the increase in puncta noted in the lower concentrations does not appear to be as prevalent when compared to the control. Interestingly, DAPI staining remains relatively consistent and evenly distributed, and there is little evidence to suggest the presence of gaps as noted in prior treatment groups. Though the prevalence and severity of distortion along cell boundaries does suggest increased modulation of tight junction organization and cell morphology compared to the lower concentrations of MPA.

### 4.5.2 MPA Exposure Decreases Primary Mouse Colonoid Monolayer Transepithelial Resistance

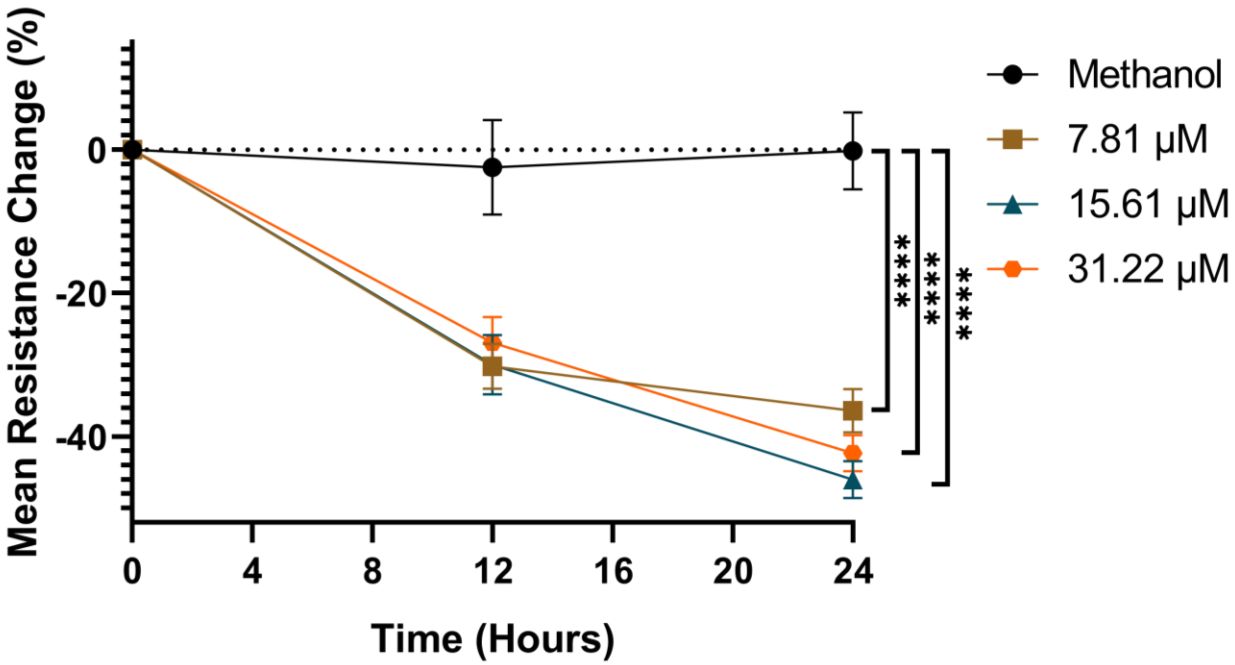


**Figure 4.10** Measurement of transepithelial resistance in primary mouse colonoid monolayers exposed to physiological concentrations of MPA and the vehicle control (methanol) over a 24-hour period. The y-axis corresponds to the mean percentage change in resistance compared to baseline measurements at time 0. Values represent mean ± SEM. Data passed Shapiro-Wilk test of normality and was assessed using a one-way ANOVA followed by Tukey's post-hoc test. All MPA treatments induced significant changes in monolayer resistance (**** $P < 0.0001$) compared to the control (n = 15).

To improve statistical power, and to generate more reliable and generalizable results, we conducted additional TER experiments using the previously selected MPA concentrations (7.81 µM, 15.61 µM and 31.22 µM).

The above data (Figure 4.10) illustrates a significant reduction in TER across all tested concentrations of MPA. Data was assessed using an ordinary one-way ANOVA followed by Tukey's multiple comparison test. The control treatment remained relatively stable over the 24-hour period, with a mean resistance change of -2.45 ± 6.59% at 12 hours and -0.13 ± 5.40 % at 24 hours. Exposure to 7.81 µM MPA resulted in a significant reduction in TER compared to the control group ($P < 0.0001$), with a mean resistance change of -30.2 ± 3.14 % at 12 hours and -36.4 ± 3.01 % at 24 hours. Although reduction in TER from 7.81 µM MPA appears to be less than the 15.61 µM treatment, comparison between groups shows no significant difference ($P = 0.2097$). Similarly, comparison between the 7.81 µM MPA treatment and the 31.22 µM MPA treatment shows no statistically significant difference ($P = 0.6008$). Exposure to 15.61 µM MPA showed a mean resistance change of -29.99 ± 4.16 % at 12 hours and a mean change of -45.99 ± 2.58 % at 24 hours. The 15.61 µM MPA treatment also led to a significant decrease in the overall resistance of the measured monolayers relative to the control group ($P < 0.0001$). Comparison between 15.61 µM MPA and 31.22 µM MPA treatments showed no significance ($P = 0.8753$). The highest concentration tested (31.22 µM) displayed a mean resistance change of -26.91 ± 3.56 % at 12 hours and -42.34 ± 2.54 % at 24 hours. Comparable to the other concentrations tested, the 31.22 µM MPA treatment led to a statistically significant reduction in TER when compared to the control ($P < 0.0001$).

### 4.5.3 MPA Exposure Increases Permeability in Primary Mouse Colonoid Monolayers: A FITC-Dextran Permeability Assay Analysis

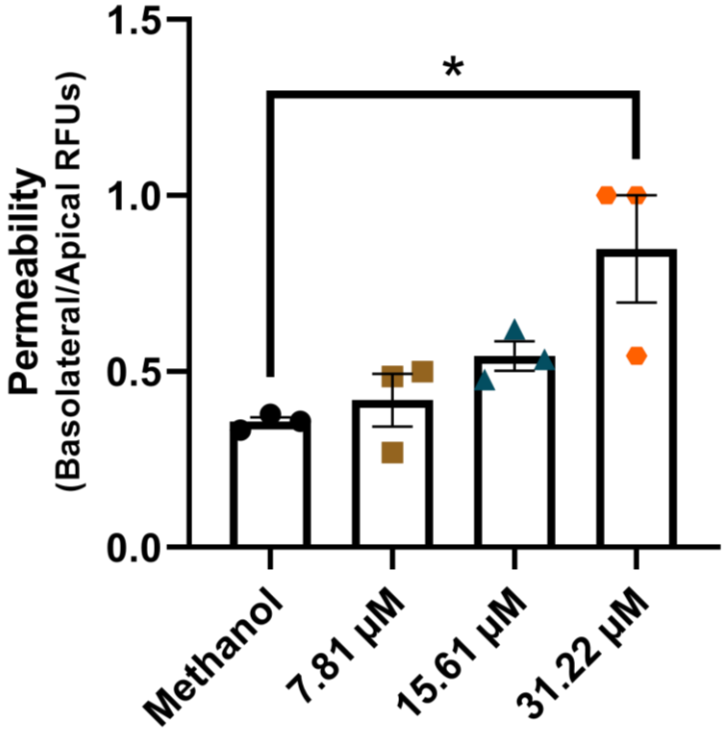


**Figure 4.11** 4 kDa FITC-Dextran permeability assay conducted on primary mouse colonoid monolayers exposed to physiological concentrations of MPA and a vehicle control (methanol) over 24 hours. The y-axis represents monolayer permeability which is determined by the ratio of basolateral to apical RFUs (basolateral/apical RFUs). Values are presented as means ± SEM. Data passed Shapiro-Wilk test of normality and was assessed using a one-way ANOVA followed by Tukey's post-hoc test. A scatterplot is superimposed to highlight individual permeability values. Only the 31.22 µM MPA treatment demonstrated significance (* P = 0.0172) compared to the control (n = 3).

To further assess barrier function, FITC-Dextran permeability assays were conducted to evaluate the flux of FITC-Dextran molecules across monolayers treated with MPA (7.81, 15.61, 31.22 µM) and a vehicle control (methanol). The resulting data highlights changes in monolayer permeability when exposed to MPA. Mean RFUs and SEM were used to quantify permeability of the monolayers. Data was analyzed using an ordinary one-way ANOVA followed by Tukey's multiple comparisons test.

The permeability data (Figure 4.11) indicates that exposure to the highest MPA concentration increases the flux rates of FITC-Dextran across the monolayers, reflecting modulation in overall barrier function. In this assessment, a permeability value of 0 represents no flow of molecules across the monolayer, while a value of 1 indicates complete permeability, allowing the maximum number of fluorescent molecules to pass through. The control treatment displayed the lowest flux of FITC-Dextran over the 24-hour period, with a permeability mean of $0.36 \pm 0.01$. Exposure to 7.81 µM MPA showed a moderate increase in permeability with a mean value of $0.42 \pm 0.07$; however, comparison to the vehicle control does not show significance ($P = 0.9568$). When treated with 15.61 µM MPA, monolayers displayed a mean permeability value of $0.54 \pm 0.04$. Although the 15.61 µM MPA treatment presents a larger increase in permeability in comparison to the 7.81 µM MPA treatment, statistical assessment shows that the intermediate MPA concentration does not demonstrate statistical significance compared to the control group ($P = 0.4708$). At the highest concentration (31.22 µM), the mean permeability value was calculated to be $0.85 \pm 0.15$. Compared to the control, 31.22 µM MPA shows a statistically significant increase in monolayer permeability ($P = 0.0172$).

### 4.5.4 Concentration Analysis of Cytokines and Chemokines in Primary Mouse Colonoid Monolayers Treated with MPA

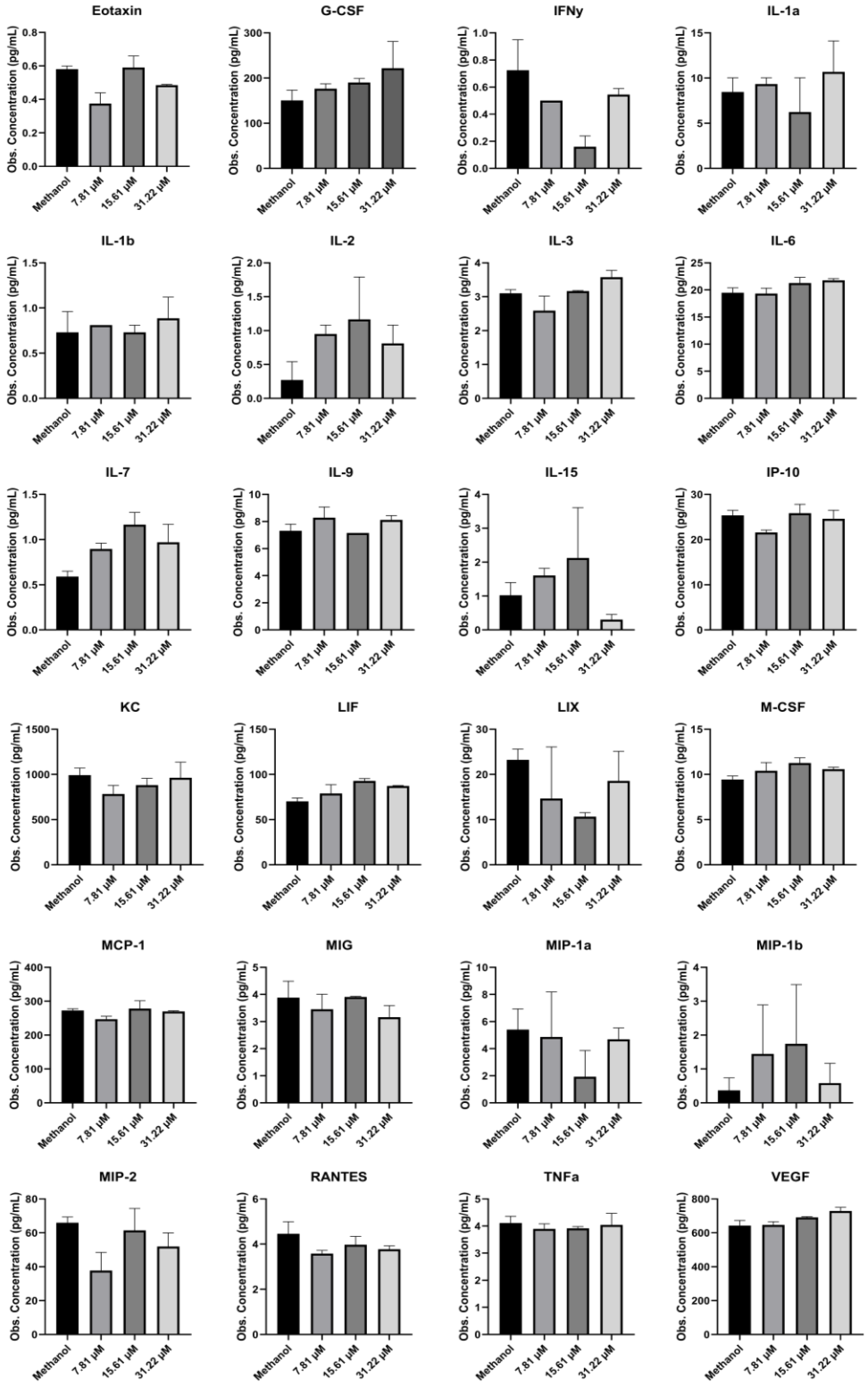

**Figure 4.12** Concentration changes in 24 different cytokines and chemokines in colonoid monolayers treated with MPA (7.81 µM, 15.61 µM, 31.22 µM) and a vehicle control (methanol) after 24 hours. Each graph represents the mean observed concentration ± SEM (n = 6) of the labelled cytokines/chemokines in control and MPA-treated conditions. Concentrations are expressed in pg/mL. Significant differences between vehicle control and MPA exposed groups were assessed using a non-parametric Kruskal-Wallis test, followed by Dunn's multiple comparisons test. No significant differences were observed ($P > 0.05$).

A comprehensive analysis of cytokine and chemokine concentrations was conducted to better characterize and understand the effects of MPA exposure on the intestinal epithelium. This study (Figure 4.12) sought to further elucidate how MPA modulates cellular signaling. To analyze changes in cytokines and chemokines, primary mouse colon organoid monolayers were exposed to various concentrations of MPA (7.81, 15.61, 31.22 µM) over a 24-hour period. After 24 hours, 2D-MCM from monolayer inserts was collected and pooled for sample submission to Eve Technologies in Calgary, Alberta. A multiplex assay of 32 different chemokines and cytokines was conducted. Only 24 of the 32 cytokines and chemokines had concentrations high enough to be detected.

Despite observing variability in concentration levels across treatment groups, none of the measured molecules demonstrated statistical significance between the MPA-treated and vehicle control conditions. Significance was determined using a Kruskal-Wallis test, followed by Dunn's multiple comparison test. No cytokine or chemokine met the threshold for significance ($P > 0.05$).

## 4.6 Deciphering MPA Toxicity: Transcriptomic Data from Primary Mouse Colon Colonoid Monolayers Exposed to MPA.

To gain insight into the potential mechanisms underlying MPA-induced GI toxicity, we performed total RNA-seq analysis comparing MPA-treated monolayers to a vehicle control. The aim was to identify DEGs and their associated molecular pathways. Our goal was to utilize these DEGs to identify key pathways, and to evaluate the potential of targeting these pathways to mitigate MPA-induced GI toxicity.

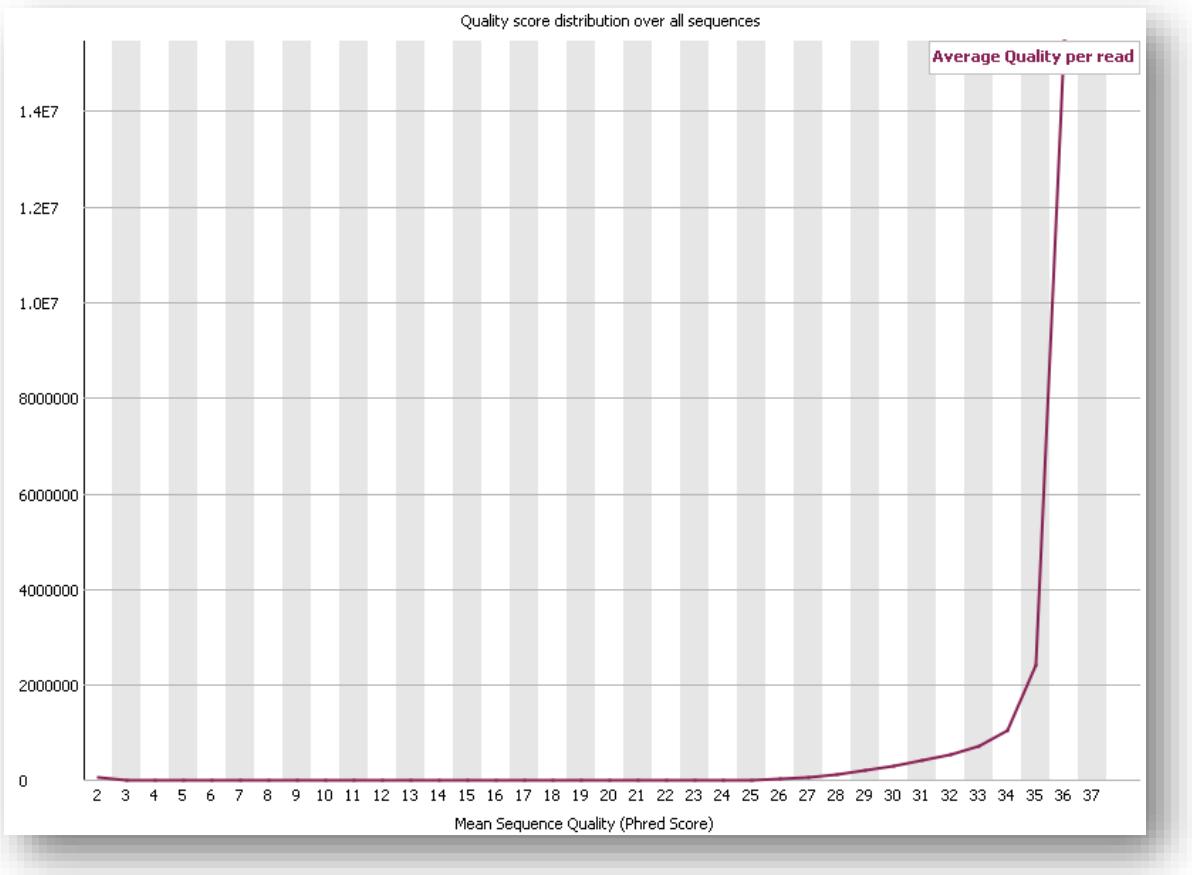


**Figure 4.13** FastQC report plot showing quality score distribution across all sequenced reads. The x-axis represents the mean sequence quality (Phred score) ranging from 2 to 37, and the y-axis represents the number of sequences at each quality score. Scores above 30 indicate high-quality reads. The sharp increase past 30 indicates that the data meets quality expectations for downstream analyses.

Total RNA was extracted from pooled colonoid monolayers following exposure to various concentrations of MPA (7.81, 15.61, 31.22 µM) and a vehicle control (methanol). RNA concentrations for each treatment group, measured using a Nanodrop 2000, were as follows: Methanol vehicle control at 129.50 ng/µL, 7.81 µM MPA at 95.60 ng/µL, 15.61 µM MPA at 68.20 ng/µL, and 31.22 µM MPA at 94.70 ng/µL. Sequencing was conducted by the CHGI at the University of Calgary. Raw RNA-seq data was assessed using FastQC. The "Per Sequence Quality Scores" FastQC plot (Figure 4.13) indicated high overall sequencing quality, with most sequences scoring above 30. Following quality control, RNA-seq data was processed through the usegalaxy.eu platform. Reads were aligned to mouse comprehensive gene annotation M35 (GRCm39) from GENCODE. Differential expression analysis was conducted using DESeq2 to obtain a total of 2510 DEGs.

### 4.6.1 Visualization of Gene Expression Changes Post-MPA Exposure: Heatmap and Volcano Plot Analysis

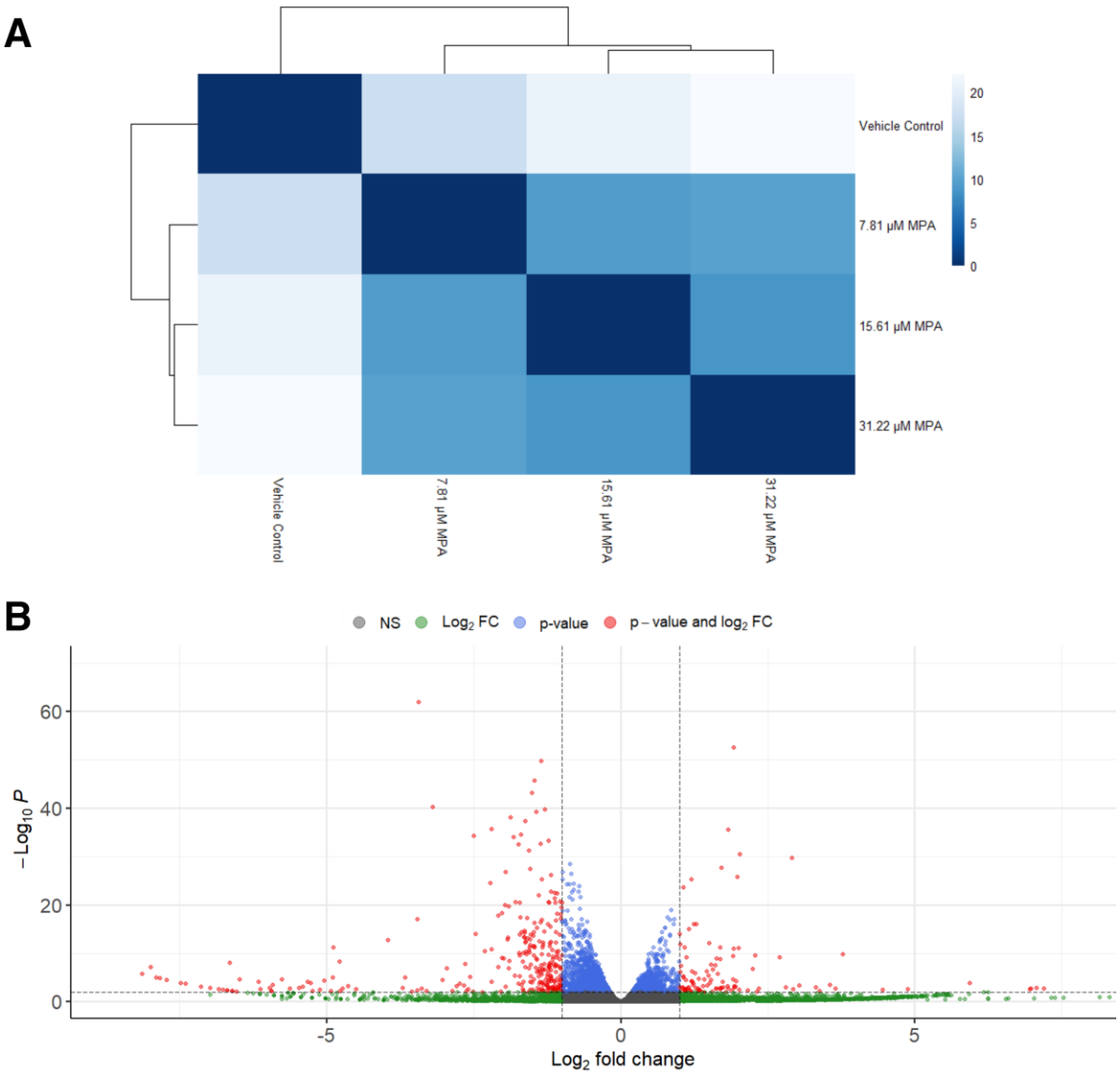


**Figure 4.14** Graphical representations of differential expression analysis conducted through Rstudio. (A) Expression profile heatmap illustrating expression differences across different MPA treatment groups (7.81, 15.61, 31.22 µM MPA) and a vehicle control. Each row and column represent the various treatment conditions. The heatmap represents rlog-transformed normalized count values (rlog values). Rlog values indicate the degree of transcript expression, with higher values corresponding to greater differences relative to the conditions being compared. An rlog value of 0 is represented in blue, indicating no difference between the groups being compared. Fading of the blue intensity corresponds to higher rlog values (greater difference). (B) Volcano plot demonstrating the relationship between $Log_2$ fold change (x-axis) and statistical significance (y-axis) of gene expression differences between MPA treatment and vehicle control. The volcano

plot does not distinguish between different MPA concentrations and is an averaged representation of treatment vs control.

The heatmap presented in Figure 4.14 was generated using the ‘pheatmap’ package in Rstudio. The visualized data illustrates the hierarchical clustering of gene expression profiles from primary mouse colonoid monolayers treated with MPA (7.81, 15.61, 31.22 µM) compared to a vehicle control (methanol). Visualization of the dataset demonstrates a distinguishable trend in expression differences between the different concentrations of MPA treatment and the vehicle control, suggesting the presence of progressive biological responses to increasing MPA concentrations. Though the differences between MPA conditions appear to be minute.

Assessment of the plot reveals that the vehicle control exhibits the most distinct gene expression profile when compared to each condition. The largest difference in expression occurs between the vehicle control and the 31.22 µM MPA group with an rlog value of 22.12 (Figure 4.14 A). As the concentration of MPA decreases, the expression profiles trend towards increased similarity with the control group. This is evident with rlog values of 20.68 for the 15.61 µM treatment and 17.33 for the 7.81 µM treatment (Figure 4.14 A). Comparison of the MPA treatments reveals that the 31.22 µM MPA expression profile is closest to the 15.61 µM MPA treatment with an rlog value of 8.70, followed by the 7.81 µM MPA treatment at a value of 9.86 (Figure 4.14 A). Differences between the 7.81 µM MPA treatment and the 15.61 µM MPA treatment show a similar result, with an rlog value of 9.34 between groups (Figure 4.14 A).

Volcano plot analysis (Figure 4.14 B) categorized 35,627 identified genes into four groups based on their statistical significance and magnitude of change in expression. 21,699 of these genes were categorized as non-significant, labelled as NS in grey (Figure 4.14 B). Non-significance indicates that these genes did not meet the threshold for statistical significance in

either $Log_2$ fold change ($\geq |1|$) or p-value ($< 0.05$). Among these, 12,624 genes were upregulated, while 9,075 were downregulated. A smaller subset of genes displayed significant changes in $Log_2$ fold change but did not meet p-value significance and were categorized as $Log_2$ FC in green (Figure 4.14 B). The $Log_2$ FC group contained 179 genes, with 93 genes upregulated and 86 genes downregulated. 2,210 genes labeled in blue were categorized as significant by p-value alone, however these did not meet the $Log_2$ fold change threshold (Figure 4.14 B). Among these genes, 799 were upregulated and 1,411 were downregulated. A total of 320 genes labelled in red were categorized to meet both the $Log_2$ fold change threshold and p-value threshold (Figure 4.14 B). Of the 320 genes identified, 91 were upregulated, and 229 were downregulated. These 320 genes represented key targets for downstream analyses.

### 4.6.2 IPA Software Analysis: Exploring MPA-Induced Gene Expression Changes

To evaluate molecular changes induced by MPA treatment, a meta-condition analysis of the DEGs was conducted using IPA software. This approach was chosen to address several key objectives such as, identification of common molecular responses, enhanced statistical power, simplified analysis for broader insights, and to focus on universally affected pathways. While assessing each MPA concentration may provide insight on the variance between MPA treatments, this approach was intended to generate a thorough list of candidate genes and pathways that could be involved in MPA's mechanism of GI toxicity.

All 2,510 identified DEGs were uploaded to IPA. When filtered for a FDR $\leq 0.05$ and a $Log_2$ fold change $\geq |1|$, only 320 DEGs were observed. In line with the results of the volcano plot analysis, IPA identified 91 upregulated genes and 229 downregulated genes. A summary of the top 10 upregulated and top 10 downregulated genes is presented in Tables 4.1 and 4.2.

**Table 4.1** Top 10 upregulated genes as identified by IPA software.

| Gene | $Log_2$ Fold Change | FDR |
|---|---|---|
| Gm12669 | 3.775 | 7.25e-09 |
| Lce1f | 3.553 | 3.02e-03 |
| XIRP2 | 3.032 | 3.74e-03 |
| SIGLEC 10 | 2.907 | 1.22e-27 |
| NDOR1 | 2.802 | 8.02e-03 |
| Gm2792/Gm2808 | 2.707 | 2.81e-08 |
| DERL3 | 2.348 | 1.52e-02 |
| Mcpt8 | 2.287 | 1.51e-08 |
| SLC25A53 | 2.241 | 5.10e-06 |
| DZANK1 | 2.163 | 2.64e-02 |

**Table 4.2** Top 10 downregulated genes as identified by IPA software.

| Gene | $Log_2$ Fold Change | FDR |
|---|---|---|
| Gm4340 | -5.475 | 1.13e-02 |
| Zscan4c | -4.886 | 3.76e-10 |
| Gm21939 | -4.786 | 1.78e-07 |
| Cwc22rt3 | -3.962 | 1.48e-11 |
| RSAD2 | -3.461 | 1.66e-15 |
| DMBT1 | -3.439 | 1.50e-58 |
| H2BC9 | -3.201 | 1.22e-37 |
| SP110 | -3.036 | 5.04e-04 |
| ARHGAP8 | -2.737 | 2.12e-03 |
| CDX1 | -2.665 | 3.74e-03 |

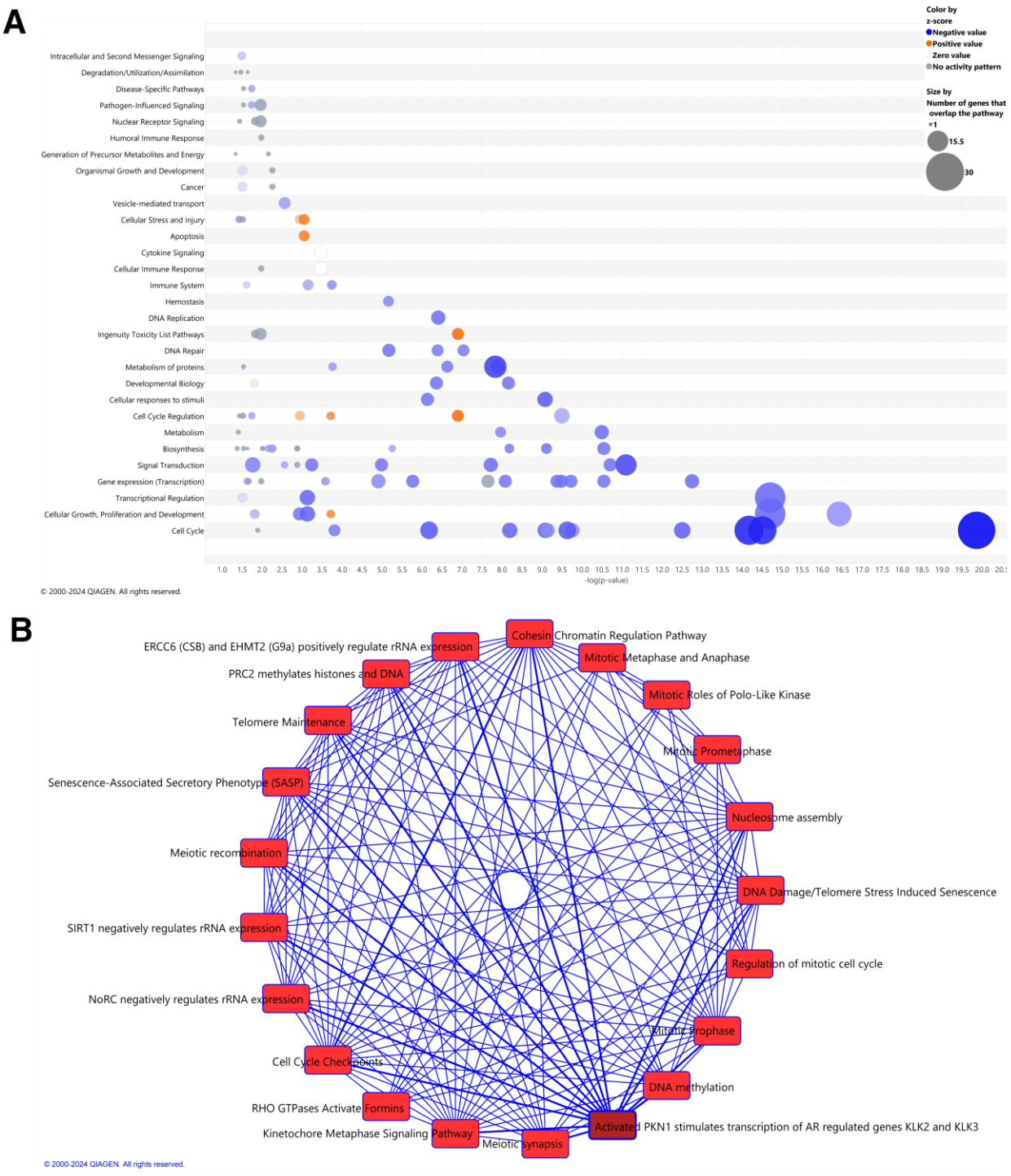


**Figure 4.15** Pathway analysis of MPA-induced gene expression changes. (A) Canonical pathway bubble chart revealing pathways significantly affected by MPA treatment. Each bubble corresponds to a distinct pathway, with the size of the bubble representing the number of genes affected in that pathway. The color indicates z-score, with blue representing a negative score (downregulated), orange representing a positive score (upregulated), and grey representing no

activity pattern. The x-axis corresponds to the -log(p-value), which indicates significance of the pathway enrichment, with larger values suggesting higher significance. The y-axis categorizes each pathway by their biological function. (B) Overlapping pathway network map displaying the connections between the significantly affected pathways from panel A. Each node represents a pathway, with lines connecting nodes signifying shared genes or functional relationships.

**Table 4.3** Summary of seven different pathways identified from the canonical pathway analysis in Figure 4.14. A sample of pathways corresponding to a high z-score and significance is depicted, with representation for both inhibited and activated pathways.

| Pathway | p-value | Overlap | z-score |
|---|---|---|---|
| Cell Cycle Checkpoints | 1.37e-20 | 11% 30/272 | -5.477 (inhibited) |
| Kinetochore Metaphase Signaling Pathway | 3.76e-17 | 17.3% 19/110 | -2.357 (inhibited) |
| Mitotic Metaphase and Anaphase | 6.68e-15 | 9.8% 23/235 | -4.796 (inhibited) |
| Cohesin Chromatin Regulation Pathway | 1.99e-15 | 9.7 % 24/247 | -3.273 (inhibited) |
| RHO GTPases Activate Formins | 8.00e-12 | 11.5% 16/139 | -4.000 (inhibited) |
| Cell Cycle: G2/M DNA Damage Checkpoint Regulation | 1.28e-07 | 15.7% 8/51 | 2.828 (activated) |
| DNA damage-induced 14-3-3σ Signaling | 1.93e-04 | 10.9% 5/46 | 2.236 (activated) |

**Table 4.4** Summary of the most significant molecular and cellular functions identified by IPA based on the DEGs dataset. The listed biological processes were predicted to be the most affected by MPA treatment.

| Molecular/Cellular Function | p-value range | Number of molecules |
|---|---|---|
| Cell Cycle | 5.73e-03 - 1.68e-23 | 86 |
| Cellular Assembly and Organization | 5.73e-03 - 2.63e-23 | 112 |
| DNA Replication, Recombination, and Repair | 4.14e-03 - 2.63e-23 | 89 |
| Cell Morphology | 5.73e-03 - 2.40e-18 | 63 |
| Cellular Function and Maintenance | 5.73e-03 - 4.93e-15 | 105 |

**Table 4.5** Summary of key upstream regulators that may be responsible for observed changes in gene expression in primary mouse colonoid monolayers treated with MPA. These five regulators provide a sample of the overall data, demonstrating some of the highest overall significance and z-score, with representation for both inhibited and activated regulators. The p-value of overlap indicates the significance of overlap between the genes regulated by the upstream regulator and the DEGs present in the dataset. Activation z-score predicts whether the regulator is activated or inhibited in the context of the sequencing data.

| Upstream regulator | p-value of overlap | Activation z-score |
|---|---|---|
| Eldr | 1.99e-56 | -5.965 (inhibited) |
| TBX3 | 1.20e-37 | -6.395 (inhibited) |
| FOXM1 | 8.30e-25 | -4.786 (inhibited) |
| NUPR1 | 1.43e-22 | 5.060 (activated) |
| TP53 | 5.74e-22 | 3.800 (activated) |

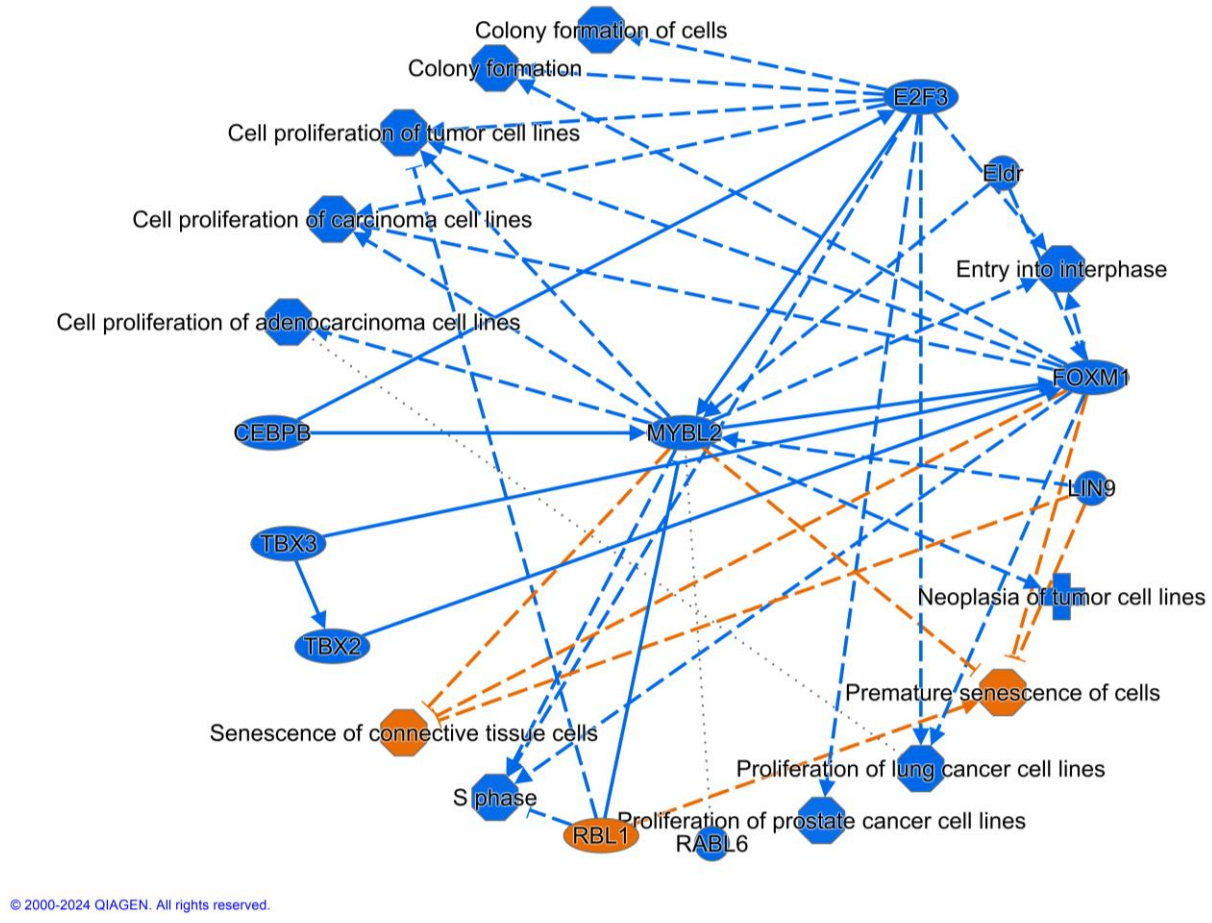


**Figure 4.16** Graphical summary of the sequencing dataset generated by IPA. The diagram illustrates the complex web of molecular networks and pathways affected by MPA treatment in primary mouse colonoid monolayers. Each node represents a specific function (octagon), transcriptional regulator (oval), disease (plus sign) or other (circle). Blue lines indicate inhibition

and orange lines indicate activation, with solid lines representing direct interactions and dashed lines representing indirect interactions. The color of each node reflects the activation (orange) or inhibition (blue) of that specific node.

IPA revealed 121 canonical pathways significantly altered by MPA treatment, with particular emphasis on pathways related to cell cycle regulation, DNA replication and repair, proliferation, morphology, and cellular assembly (Figure 4.15 and Table 4.4). The most significantly impacted pathway was Cell Cycle Checkpoints (p-value of 1.37e-20), with a z-score of -5.477 indicating strong prediction of inhibition (Table 4.3). Other notable pathways included Kinetochore Metaphase Signaling Pathway (p-value: 3.76e-17, z-score: -2.357), Mitotic Metaphase and Anaphase (p-value: 6.68e-15, z-score: -4.796), and Cohesin Chromatin Regulation Pathway (p-value: 1.99e-15, z-score: -3.273) (Table 4.3). Similarly, the RHO GTPases Activate Formins pathway was also significantly altered with a strong prediction of inhibition (p-value: 8.00e-12, z-score: -4.000) (Table 4.3). In contrast, the Cell Cycle: G2/M DNA Damage Checkpoint Regulation pathway (p-value: 1.28e-07, z-score: 2828), and the DNA Damage-induced 14-3-3σ Signaling pathway (p-value: 1.93e-04, z-score: 2.236) were predicted to be activated in response to MPA treatment.

Analysis also identified key upstream regulators potentially driving the observed expression changes. For example, Eldr, FOXM1, and TBX3 were all strongly predicted to have inhibited regulatory activity (Table 4.5). While analysis of NUPR1 and TP53 showed predictions of activated regulatory activity (Table 4.5). The visual summary generated by IPA (Figure 4.16) further illustrates the molecular interactions and functions that were impacted by MPA. Key regulators in this network, such as MYBL2, CEBPB, FOXM1, TBX3 and E2F3, exhibited predictions of inhibition. These regulators are graphically linked to activities such as cell cycle progression, and proliferation, with some also having a role in suppression of cellular

senescence. Predicted inhibition of these regulators is illustrated to inhibit S phase progression, entry into interphase, and to promote premature senescence (Figure 4.16). Also notable is the predicted activation of RBL1, leading to inhibited proliferation and induction of premature cellular senescence (Figure 4.16). Similar interactions are noted in Figure 4.15 B, with prominent crosstalk between pathways involved in chromatin regulation, mitotic processes, cell cycle regulation, and DNA damage/repair.

## 4.7 Effects of Guanosine Supplementation on Primary Mouse Colonoid Monolayers and 3D Colonoids Exposed to MPA

### 4.7.1 Guanosine Supplementation Rescues Primary Mouse Colonoid Monolayers from MPA-Induced Changes in Transepithelial Resistance

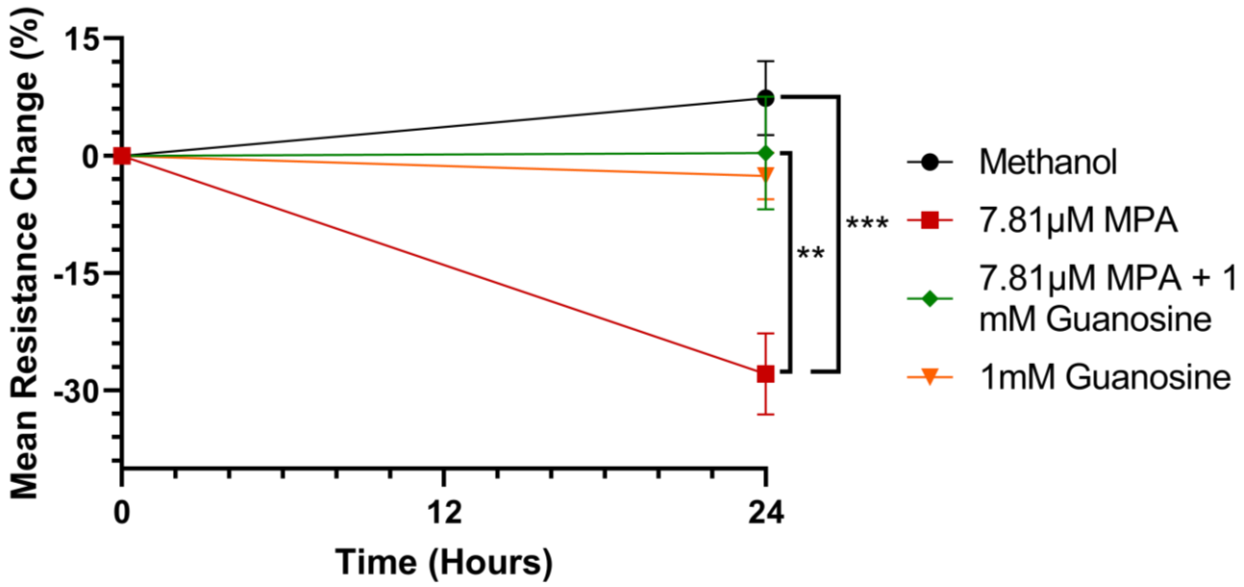


**Figure 4.17** Transepithelial resistance of primary mouse colonoid monolayers after 24 hours of exposure to 4 different treatments: Vehicle control (methanol), 7.81 µM MPA, 7.81 µM MPA + 1 mM Guanosine, and 1 mM Guanosine. The y-axis corresponds to the mean percent change in TER compared to baseline measurements taken at time 0. Values represent mean ± SEM. Data passed Shapiro-Wilk test of normality and was assessed using a one-way ANOVA followed by Tukey's post-hoc test. Co-treatment with guanosine significantly restored TER (*** P = 0.0002, ** P = 0.0032) when compared to 7.81 µM MPA treatment (n = 9).

Based on the results of our RNA sequencing analysis, we hypothesized that the mechanism of MPA-induced GI toxicity is related to a depletion in guanine nucleotides due to inhibition of *de novo* nucleotide metabolism. This study (Figure 4.17) aimed to establish whether guanosine supplementation would be sufficient in rescuing monolayer barrier function during exposure to MPA. A concentration of 7.81 µM MPA was selected as it represented the lowest tested concentration. Utilizing the lowest concentration was precautionary as to minimize the presence of cytotoxicity that may or may not be present at higher MPA concentrations.

As shown in Figure 4.17, there was a slight measurable increase in the TER of the control group monolayers with a mean change of 7.35 ± 4.75 % after 24 hours. When exposed to 7.81 µM MPA, the monolayers exhibited a decrease in TER with a mean change of -27.89 ± 5.18 % at the 24-hour mark. When compared to the control, this reduction in TER was calculated to be statistically significant ($P = 0.0002$), in agreement with our previously presented data (Figure 4.10). When exposed to 7.81µM MPA and supplemented with 1mM Guanosine, TER remained stable with a mean resistance change of 0.36 ± 7.20 % after 24 hours. Comparison to the 7.81 µM MPA treatment without guanosine reveals that the presence of exogenous guanosine significantly mitigates the effects of MPA on monolayer barrier function ($P = 0.0032$). Exposure to 7.81 µM MPA + 1 mM guanosine shows no significance when compared to the vehicle control group ($P = 0.7823$), further supporting the protective effects of guanosine supplementation in the presence of MPA. 1mM Guanosine supplementation alone did not significantly alter TER compared to the control ($P = 0.5466$), with a mean resistance change of -2.57 ± 2.97 % at the 24-hour time point. Guanosine supplementation alone when compared to the 7.81 µM MPA treatment, shows statistical significance ($P = 0.0091$).

### 4.7.2 Guanosine Supplementation Restores Primary Mouse Colonoid Growth from MPA-Induced Inhibition

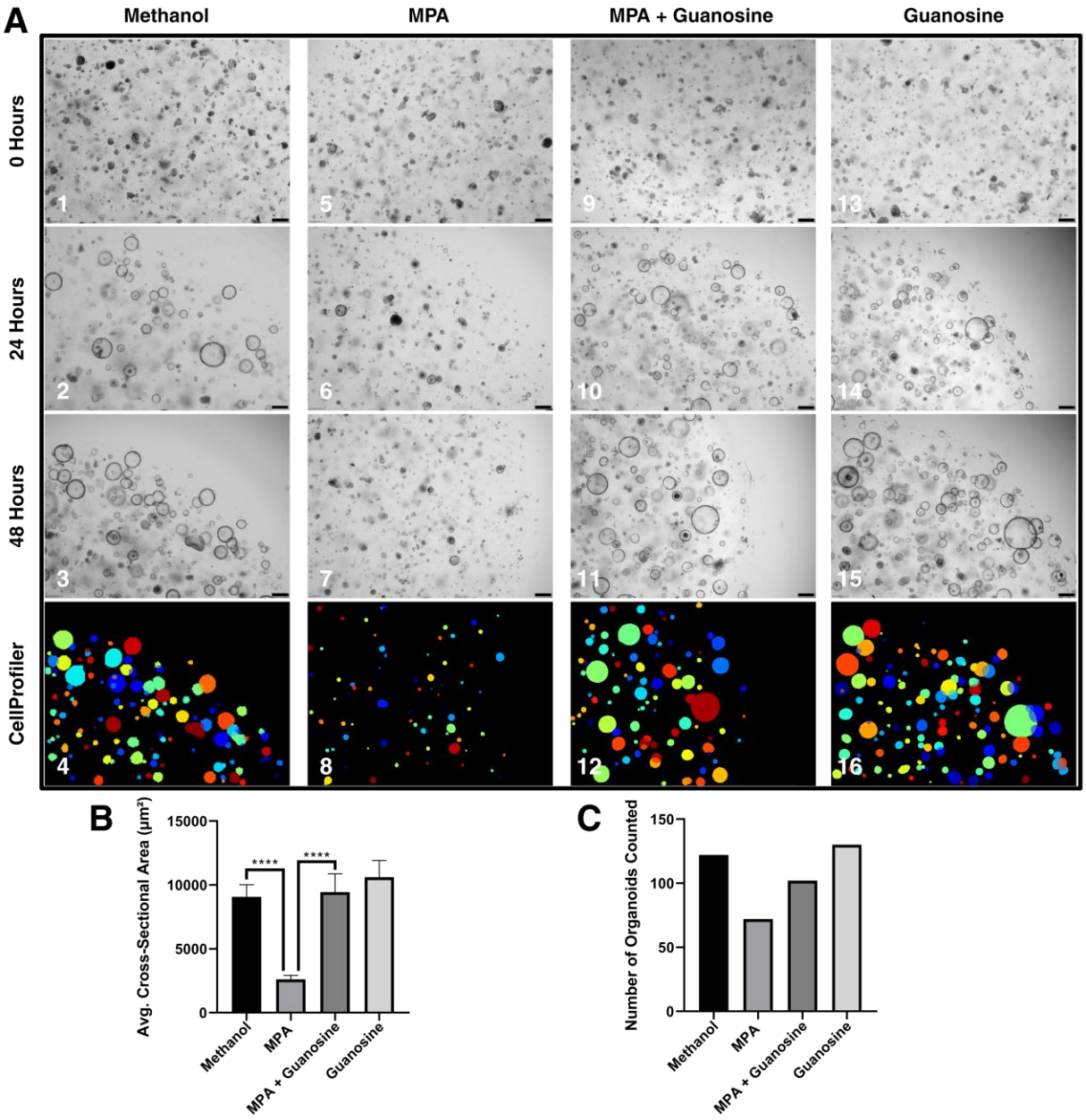


**Figure 4.18** Assessment of 3D colonoid growth after 48 hours of exposure to 4 different treatments: Vehicle control (methanol), 7.81 µM MPA, 7.81 µM MPA + 1 mM guanosine, and 1 mM guanosine. (A) Time-lapse bright-field microscopy imaging of colonoid cultures over a 48-hour period. The first three rows depict colonoid growth at different time points (0 hours, 24 hours, 48 hours). The final row consists of representative images from CellProfiler software analysis. Bright-field microscopy images taken at the 48-hour timepoint were processed through CellProfiler for quantification of organoid growth and count. (B) Graphical representation of the

CellProfiler analysis, illustrating the average cross-sectional area of the organoids. The average cross-sectional area was calculated for each treatment condition at the 48-hour time point to evaluate changes in growth. (C) Number of organoids detected by CellProfiler for each treatment at the 48-hour time point. Data was assessed using a Kruskal Wallis test followed by Dunn's post hoc test. Values are presented as means ± SEM. (**** $P < 0.0001$). *Created with BioRender.com*

Newly passaged colonoids were treated under four distinct conditions: Vehicle control (methanol), 7.81 µM MPA, 7.81 µM MPA + 1 mM guanosine, and 1mM guanosine. Colonoids were observed at 0 hours (immediately after plating), 24 hours, and 48 hours with bright-field microscopy. Images and videos were digitally recorded at each timepoint. Time lapse imaging was conducted to monitor growth of the colonoids under these four different conditions.

Colonoids in the vehicle control group displayed normal growth patterns with increasing size and density over time (Figure 4.18 A panels 1, 2, and 3). At time 0 (Panel 1), small clusters of cells from freshly split colonoids were uniformly distributed throughout the Matrigel matrix. By 24 hours (Panel 2), the formation of organized colonoid structures is clearly visible. After 48 hours (Panel 3), there is a noticeable increase in the overall size and density of the organoids, indicating healthy proliferation and development under control conditions. Treatment with 7.81 µM MPA resulted in evident inhibition of growth when compared to the control condition (Figure 4.18 A panels 5, 6 and 7). At time 0 (Panel 5), the small clusters of cells appear similar in presentation to the control; however, by 24 hours (Panel 6), there was a marked reduction in organoid development, clearly distinguishable by the lack of larger more mature colonoid structures. By 48 hours (Panel 7), visible colonoids were considerably smaller and less numerous when compared to the control images, indicating modulation of growth and development by MPA treatment. When 1mM guanosine was co-administered with 7.81 µM MPA, inhibition of growth appeared to be mitigated almost completely (Figure 4.18 A panels 9, 10 and 11). At 0

hours (Panel 9), the presence of small clusters is presented similarly to that of the previously mentioned conditions. By 24 hours (Panel 10), there is evidence of moderate growth and development, consistent with the pattern observed in the control column (Panel 2). At the 48-hour time point (Panel 11), the colonoids exhibited increased growth and density, comparable to the observations found in the control group. Colonoids treated with 1mM guanosine displayed growth patterns similar to the control group (Figure 4.18 A panels 13, 14 and 15). Initial imaging at time 0 (Panel 13) shows uniform distribution of small cell clusters in line with previous observations. At 24 hours (Panel 14) and 48 hours (Panel 15) considerable colonoid development is evident, with increases in density comparable to the control condition. Similarity with the control treatment, suggests that guanosine supplementation alone does not noticeably alter colonoid growth dynamics. Representative images from the CellProfiler software analysis provides an even clearer demonstration of the observations made at 48 hours, with improved visibility of the colonoid structures and reduced visual clutter from the background (Figure 4.18 A panels 4, 8 ,12 and 16).

Quantitative analysis of the average cross-sectional area of the colonoids at 48 hours further supports the aforementioned observations (Figure 4.18 B). Colonoids in the vehicle control group exhibited a mean cross-sectional area of 9,067 $\mu m^2 \pm 952.6 \mu m^2$. Area ranged from 519.2 $\mu m^2$ to a maximum of 51,005 $\mu m^2$. The 7.81 µM MPA colonoid cultures exhibited reduced mean cross-sectional area when compared to the control with a mean area of 2,611 $\mu m^2 \pm 312.3 \mu m^2$. Area measurements in this condition ranged from 404.2 $\mu m^2$ to 14,744 $\mu m^2$. Analysis of the data using a Kruskal-Wallis test followed by Dunn's multiple comparisons test indicates that the difference in cross-sectional area between the 7.81 µM MPA treatment and the control was statistically significant ($p < 0.0001$). Co-treatment with 7.81 µM MPA and 1mM guanosine

resulted in recovery of growth, with a mean cross-sectional area of 9,445 μm² ± 1,425 μm². Visible colonoids in this group presented a range in cross-sectional area from 660.4 μm² to 103,775 μm². When compared to the control group, co-administration of 1mM guanosine with 7.81 μM MPA was calculated to be statistically insignificant ($p > 0.9999$). Comparison to 7.81 μM MPA treatment indicates that guanosine supplementation significantly mitigates MPA growth inhibition ($p > 0.0001$). Colonoids treated with 1mM guanosine alone demonstrated the largest mean cross-sectional area, measuring at 10,529 μm² ± 1,296 μm². The cross-sectional area of the measured colonoids ranged from 506.7 μm² to 130,687 μm². Comparison to the control showed no statistical significance ($p > 0.9999$), suggesting that guanosine supplementation alone does not significantly alter colonoid growth over 48 hours.

# 5.1 DISCUSSION AND FUTURE DIRECTIONS

## 5.2 Brief Summary of Purpose

MMF is a widely prescribed immunosuppressant that demonstrates important clinical relevance. Unfortunately, adverse GI side effects often limit its use, and can diminish patient quality of life. Given the significance of MMF in modern medicine, it is imperative that further research is conducted to understand the processes behind MMF-induced GI toxicity. The aim of this thesis was to establish a suitable model of GI physiology for investigation of the mechanisms behind MMF-induced GI toxicity. We sought to elucidate the effects of MPA (the active component of MMF) on the intestinal epithelium to identify key molecular pathways for potential therapeutic targeting.

## 5.3 Key Findings

Our studies yielded several significant findings that contribute to elucidating the mechanisms underlying MPA-induced GI toxicity. First, we observed that MPA exposure led to a substantial decrease in monolayer TER, indicating that MPA may have a role in modulating barrier function in the intestines. This reduction in TER was accompanied by notable changes in overall cell morphology, specifically concerning alterations in tight junction organization and integrity. In addition to this, MPA was found to significantly alter monolayer permeability, allowing increased flux of 4 kDa FITC-dextran molecules.

Analysis of cytokines and chemokines revealed no statistically significant changes. Although trends were observed none of them can be used conclusively. A total of 2,510 DEGs were identified through total RNA sequencing, with pathway analysis highlighting alterations in

several key molecular pathways. Notably, pathways related to cell cycle regulation, DNA replication and repair, proliferation, morphology, cellular assembly, and maintenance were significantly affected. Transcriptomic analysis also revealed that MPA-induced toxicity may be facilitated through its primary mechanism of action leading to guanosine nucleotide depletion. This discovery led us to investigate guanosine supplementation as an effective strategy to mitigate MPA-induced inhibition.

Guanosine supplementation was found to significantly reduce the effects of MPA in both colonoid models (3D culture and monolayers). Co-treatment with guanosine effectively maintained TER in MPA-treated monolayers, while MPA exposure alone led to a significant reduction. Guanosine supplementation was observed to have no overall effect on the barrier function of the colonoid monolayers. In addition to stabilizing TER, guanosine supplementation also promoted the recovery of 3D colonoid growth, which was otherwise inhibited by MPA exposure. Organoids exposed to MPA demonstrated a significant reduction in overall development and growth, which was significantly mitigated in the presence of guanosine. Guanosine supplementation alone resulted in growth patterns similar to those observed in the control conditions, suggesting that guanosine alone does not modulate colonoid growth.

## 5.4 Colonoid Model System

First, we successfully developed primary mouse colon organoids as a relevant model of GI physiology. This system was established as a tissue specific model for studying the response of the intestinal epithelium to MPA exposure. Consistent monitoring, maintenance, and characterization of established colonoid cultures proved vital for maintaining high-quality conditions for downstream processing. Colonoid cultures of sufficient quality were successfully

handled and plated into colonoid monolayers for barrier function analyses. Generation of monolayers was carefully monitored, and characteristics were recorded throughout the process to ensure they exhibited the desired characteristics necessary for experimentation. The established colonoid cultures and monolayers displayed growth patterns, morphology, and characteristics that were consistent with published literature[77,82], confirming the effectiveness of the adapted protocols. The colonoids developed distinct structural features, typical of mouse colonic organoids, including clear luminal structures, surrounding epithelial layers, and budding. Colonoid monolayers reached confluency within expected timeframes, exhibiting TER values in line with previously established literature[77]. These observations demonstrate the successful establishment of the proposed organoid model and reinforce the utility of bright-field microscopy for the routine assessment and monitoring of colonoids. Alignment with published literature highlights the reliability of the established model.

Confocal microscopy visualizing monolayer morphology and tight junction integrity aided in the establishment of a baseline reference to ensure quality and consistency for experimental confidence in downstream analyses. Our confluent reference monolayer demonstrated clearly defined, continuous ZO-1 staining along cell periphery, with uniform cell distribution. There were no indications of fragmentation or morphological irregularities when compared to published literature[1]. The presence of cell nuclei corresponded strongly to the ZO-1 staining, with no gaps visible between adjacent cells. No puncta accumulation was observed, indicating proper distribution and organization of ZO-1 proteins. Together these results provided a reference characterization for normal tight junction protein localization and intact barrier integrity. In contrast, our reference non-confluent monolayer demonstrated inconsistent ZO-1 staining, presenting pronounced areas of intensity, with some regions lacking visualization all

together. Accumulations of intensity suggested areas where cells may be working to establish junctions. Incomplete cell nuclei distribution illustrated the presence of gaps with non-uniform cell distribution. Analysis of the confocal imaging was in line with our preliminary predictions that were generated through TER measurements, with the confluent monolayer demonstrating a TER value greater than 235 $\Omega \cdot cm^2$ and the non-confluent monolayer exhibiting a TER value lower than 235 $\Omega \cdot cm^2$.

TER is widely recognized as an effective tool for measurement of monolayer barrier function, providing accurate quantification for changes in barrier integrity and strength. Our preliminary MPA exposure experiment using TER measurements to quantify barrier integrity identified that all the tested MPA concentrations (7.81, 15.61, 31.22, 62.43, 124.87 µM) led to a significant reduction in TER. This reduction suggested that MPA exposure, even at the lowest concentration of 7.81 µM, significantly modulated barrier integrity. At first glance, concentrations 7.81, 15.61, 31.22, 62.43 µM appeared to demonstrate a weak dose-dependent relationship. Analysis of the data using a one-way ANOVA followed by Tukey's multiple comparisons test debunked the existence of a linear dose-dependent response. Breakdown of the multiple comparisons showed that the observed effects did not display a straightforward dose-dependent relationship, but some significant differences were present between groups. The highest reductions in TER were observed at MPA concentrations of 31.22 µM and 62.43 µM, whereas the highest concentration tested (124.87 µM) resulted in TER reductions similar to 15.61 µM MPA. While unexpected, this data indicated a complex interaction between MPA concentration and its effects on barrier integrity, suggesting a non-linear response at higher concentrations. These results validated the proposed colonoid monolayer model as a suitable system for studying the effects of MPA on intestinal barrier function. The outcome of this study

informed the decision to focus on MPA concentrations 7.81 µM, 15.61 µM and 31.22 µM for future assessments. Specifically, these concentrations were selected based on their ability to induce measurable effects and their correspondence with physiological levels of MPA reported in previously published literature[26].

## 5.5 MPA-Induced Barrier Disruption

To improve statistical power, and to generate more reliable and generalizable results, we conducted additional TER experiments using the previously selected MPA concentrations (7.81 µM, 15.61 µM and 31.22 µM). All tested concentrations of MPA caused statistically significant reductions in TER, supporting some of the preliminary MPA exposure results. Interestingly, when compared to the initial MPA exposure experiments, these results do not support any of the previously observed non-linear dose-dependent relationships, suggesting that disruption of barrier function reaches a similar level across these three different physiological concentrations of MPA. However, these results do further demonstrate that MPA exposure modulates intestinal barrier function *in vitro*.

The observed decreases in TER were followed by investigation of monolayer permeability using a 4 kDa FITC-dextran permeability assay. Assessment of FITC-dextran flux from the apical to the basolateral compartment of the monolayers showed that MPA exposure led to a significant increase in permeability. On first pass, the data appears to show that MPA exposure increases monolayer permeability in a concentration-dependent manner; however, statistical analysis indicates that the highest concentration of MPA tested (31.22 µM) was the only treatment to exhibit statistical significance in increasing monolayer permeability. The lower concentration treatments (7.81 µM and 15.61 µM MPA) also exhibited increased permeability,

albeit without reaching statistical significance when compared to the control. Interestingly, this data does not fully corroborate the TER data as expected. Though, the observed differences may be attributed to the distinct functions of the pore and leak pathways in regulating barrier function. For example, the pore pathway primarily regulates the passage of small ions (water included), which is directly reflected in TER measurements[83]. This pathway is largely controlled by claudin proteins within tight junctions[84]. The observed reduction in TER across all MPA concentrations suggests that even the lowest MPA concentration (7.81 μM) is enough to measurably disrupt the junctions controlling the pore pathway. In contrast, the leak pathway is responsible for paracellular transport of larger molecules, such as 4 kDa FITC-dextran[83]. This pathway is regulated by the cytoskeleton and epithelial long myosin light chain kinase (MLCK)[84]. The significant increase in FITC flux observed only at the highest MPA concentration suggests that the leak pathway requires higher concentrations of MPA for measurable disruption. Though it is important to note the existence of the unrestricted pathway, which demonstrates no selectivity for molecule movement due to epithelial damage and complete compromise of barrier function[84]. While it is plausible that the pore pathway is more sensitive to MPA exposure in comparison to the leak pathway, our permeability data does not discern whether increases in flux resulted from epithelial damage (unrestricted pathway) or modulation of the leak pathway. Although our data cannot confirm the presence of a dose-dependent difference between pathways, it does underscore the importance of considering all permeability pathways when assessing MPA-induced changes in barrier function. This also suggests that TER alone may not fully capture the extent of barrier dysfunction, particularly regarding the movement of larger molecules.

ZO-1 is a scaffolding protein with a crucial role in the assembly and maintenance of tight junctions, essential for barrier integrity. Confocal visualization of ZO-1 proteins revealed that

MPA causes progressive disruption of tight junctions in what appears to be a concentration dependent manner. In control monolayers, ZO-1 staining was continuous and well-defined, indicating intact barrier integrity. Puncta localization was visible and in line with our previously observed reference monolayers, reflecting normal tight junction dynamics. At 7.81 µM MPA, early signs of disruption were evident, with ZO-1 staining showing increased irregularities, along with more prominent puncta accumulation, suggesting initial tight junction destabilization. Morphological changes, such as "jagged" lines and cell elongation, were also observed. As MPA concentration increased these disruptions became more pronounced, with ZO-1 staining showing even greater irregularity and distortion, along with ZO-1 accumulation around cell nuclei, indicating altered tight junction protein localization. DAPI staining at 15.61 µM MPA revealed gaps, suggesting compromised barrier function. At the highest concentration, 31.22 µM MPA, severe morphological alterations were observed, with ZO-1 staining presenting an evident increase in tight junction abnormalities along cell borders. Interestingly, the increase in puncta seen at lower concentrations was less evident here, indicating differences in tight junction dynamics at this concentration. Despite the morphological changes, DAPI staining remained relatively consistent, suggesting the absence of monolayer gaps. Overall, these findings demonstrate that MPA modulates tight junction integrity and cell morphology, contributing to changes in barrier function, with concentration-dependent effects on ZO-1 and monolayer structure. Though differences in puncta between conditions makes it difficult to identify how increasing MPA concentrations impact tight junction protein dynamics such as trafficking and recycling.

The results of these studies align with literature indicating that MMF therapy causes significant disruption of intestinal barrier function in mice[85]. Prior studies using Caco-2 monolayers have

also reported similar findings, with MPA treatment leading to increased permeability and tight junction alterations[52]. Considering these results in comparison to clinical presentations of MMF-induced GI toxicity suggests that the effects of MPA on tight junctions plays a primary role in the development of symptoms such as diarrhea.

## 5.6 Cytokines and Chemokines

Cytokine and chemokine analysis was intended to assess the potential immunomodulatory effects of MPA. Despite observing variability in concentration levels across treatment groups, none of the measured molecules demonstrated statistical significance between the MPA-treated and vehicle control conditions. These results suggest that MPA exposure does not significantly alter cytokine and chemokine concentrations in our *in vitro* model of the intestinal epithelium. Given that MPA is known for its immunosuppressive effects, the absence of a pronounced outcome is notable; however, this may be attributed to isolated nature of our colonoid model since it lacks the presence of fundamental immune components. Macrophages, dendritic cells, T cells, and B cells, all play significant roles in mediating cytokine production during an inflammatory response[86]. Without these components it is likely that changes in inflammatory signaling is muted or absent in our model. It is also important to note that the submitted samples possessed low cytokine and chemokine concentrations, with only 24 of the 32 tested molecules being detected. Therefore, within the parameters of our study, the data indicates that MPA exposure does not exert a strong immunomodulatory effect on the epithelium at the molecular level. These results differ from *in vivo* studies where MMF treatment was shown to increase levels of G-CSF (granulocyte colony-stimulating factor), IL-15 (interleukin-15), MIP-2 (macrophage inflammatory protein 2), LIF (leukemia inhibitory factor) and TNFα (tumor necrosis factor–α)[26].

## 5.7 Total RNA-Sequencing

Based on analysis of previously published literature and observations from our prior experiments, we hypothesized that MPA would alter expression of pathways related to cellular stress, morphology, and barrier integrity. To evaluate changes in gene expression, we conducted total-RNA sequencing of colonoid monolayers exposed to physiological concentrations of MPA. The resulting transcriptomic data identified a range of genes and pathways affected by local MPA exposure. The highest concentration of MPA (31.22 µM) induced the most significant changes, with a markedly different expression profile compared to the control group. Slight differences between MPA conditions suggested the presence of a dose-dependent response; however, the focus of our analysis was to identify a thorough list of candidate genes and pathways that could be involved in MPA's mechanism of GI toxicity, rather than compare the different MPA concentrations. As such, a combined differential expression analysis was used and uploaded to the IPA software.

Analysis of the transcriptomic dataset showed significant modulation of pathways involved in cell cycle regulation and DNA replication, particularly those governing the S-phase and mitotic processes. Since MPA is known to inhibit the synthesis of guanine nucleotides in lymphocytes, this may indicate a similar process is occurring in our colonoid model. Previous work has shown that depletion of guanine nucleotides results in replicative stress[87], triggering cell cycle arrest and senescence[88]. Similar implications were illustrated in our dataset with predicted inhibition of S phase progression and activation of premature senescence (Figure 4.16). Inhibition of S phase progression suggests the accumulation of cells halted in S phase, which is consistent with observed inhibition of pathways related to DNA synthesis and repair. Beyond S phase, MPA's effects also extended into the regulation of mitosis. Predicted inhibition of the

Kinetochore Metaphase Signaling Pathway, Mitotic Metaphase and Anaphase, and Cohesin Chromatin Regulation Pathway suggests that MPA modulates processes required for proper chromosomal segregation and mitotic progression. Inhibition of these pathways demonstrates that MPA may cause chromosomal instability. Furthermore, the activation of pathways associated with DNA damage responses, such as Cell Cycle: G2/M DNA Damage Checkpoint Regulation and DNA Damage Induced 14-3-3σ Signaling, emphasizes the presence of cellular responses to genotoxic stress. Activation of these pathways illustrates the cellular attempt to arrest the cell cycle and repair damaged DNA. Concurrent inhibition of FOXM1 and TBX3, key regulators of DNA repair, proliferation, and stem cell maintenance[89–91], suggests that MPA's effects may overwhelm these protective mechanisms, leading to an accumulation of DNA damage, reduced proliferation, and loss of self-renewal.

In addition to disruption of DNA replication, MPA was found to significantly modulate the RhoGTPase Signaling Pathway. This pathway is important for regulation of the actin cytoskeleton, cell shape and motility[92]. Predicted inhibition of this pathway indicates that MPA interferes with cellular morphology and cytoskeleton dynamics, corroborating our previous confocal imaging observations. Given the role of RhoGTPase signaling in cytoskeleton organization, it is likely that MPA-induced inhibition of this pathway leads to compromised integrity of the epithelial barrier[93]. This aligns with our observations of reduced barrier function in the presence of MPA. Predicted activation of stress response pathways, such as those controlled by NUPR1 and TP53, suggest that MPA exposure may push cells towards a senescent state. TP53, in particular is known for its role in activating DNA damage responses, cell cycle arrest, and inducing senescence[94].

Previous studies investigating the interactions between MPA and lymphocytes have shown that MPA blocks the progression of the cell cycle, specifically by arresting lymphocytes in the S phase[95]. S phase arrest in lymphocytes was found to induce DNA damage and contributed to upregulation of apoptosis[95,96]. Inhibition of guanine nucleotide synthesis by MPA was also found to modulate morphological changes in lymphocytes[96]. Alignment of these findings with observations in our colonoid model led us to hypothesize that MPA inhibition of IMPDH facilitates GI toxicity. As such, we decided to explore the potential application of exogenous guanosine supplementation.

## 5.8 Guanosine Supplementation

Given that exogenous guanosine can be internalized into intestinal cells via the salvage pathway[97] (Figure 1.1), supplementation was hypothesized to replenish guanine nucleotide pools to ultimately protect against the adverse effects of MPA inhibition. Co-administration of guanosine with MPA resulted in preservation of TER. When compared to the control, there was no statistical difference, indicating that exogenous guanosine significantly mitigated the effects of MPA on monolayer barrier function. In contrast, the MPA treatment alone significantly reduced TER compared to both the control and co-administration conditions. These results were in line with our earlier data, supporting the outcomes of this study. Guanosine supplementation alone did not show any significant differences compared to the control. Together these results indicate that guanosine supplementation does not affect monolayer barrier function, but when added in conjunction with MPA significantly ameliorates the substantial reduction in TER.

Next, we wanted to evaluate whether guanosine supplementation would be sufficient in restoring cell cycle progression and preventing induction of cellular senescence. As a

preliminary approach, we decided to indirectly investigate the modulation of these processes through observations of colonoid proliferation. Colonoids exposed to 7.81 µM demonstrated significant inhibition of development and growth compared to the control. This finding was consistent with the expectations set from our pathway analyses. The results of guanosine co-administration were compelling. Colonoids treated with both MPA, and guanosine showed a significant restoration in growth, with metrics such as average cross-sectional area and colonoid density returning to levels comparable to the control group. These observations suggest that supplementation of exogenous guanosine effectively counteracts nucleotide depletion caused by MPA, allowing cells to resume DNA replication and cell cycle progression. While this data is only preliminary and not conclusive across all effects that MPA-induces, it does underscore the possibility for guanosine supplementation to extend beyond nucleotide replenishment. For example, by restoring cell cycle progression, guanosine may also mitigate the activation of DNA damage responses and subsequent induction of cellular senescence and apoptosis, both of which are consequences of prolonged replicative stress[98].

This data contradicts previous literature, which characterizes MPA as a "selective" inhibitor of lymphocyte proliferation[30,99–104]. Our guanosine studies indicate that MPA's inhibition of nucleotide metabolism is not selective for lymphocytes but is broader than originally described. This observation may be attributed to the highly proliferative state of the intestinal epithelium. It is widely stated that MPA demonstrates more potent inhibition of IMPDH isoform II (IMPDH2), compared with that of isoform I (IMPDH1)[105–107]. IMPDH1 is expressed in many cell types, while IMPDH2 is expressed predominately in highly proliferative cell lines, such as activated lymphocytes[104,108,109]. It is through preferential inhibition of IMPDH2 that MPA is considered "selective" for lymphocyte populations. Interestingly, previous research

shows that the intestinal epithelium expresses significant levels of IMPDH2[110]. The prevalence of IMPDH2 in the intestinal epithelium is further evidenced by its well-known reputation for the highest proliferation rates in the human body[111]. Therefore, it is plausible that MPA-induced GI toxicity is facilitated by reliance on IMPDH2, similar to that of activated lymphocytes. This may provide an explanation as to why clinical presentations of MMF-induced toxicity occur predominately in the GI tract. Furthermore, the extended presence of MPA, driven by continuous recycling through GUS enzymes, implies that the intestinal epithelium is exposed to active MPA more consistently than other tissues. Given the high proliferative demands of the intestinal epithelium, this prolonged exposure is likely more detrimental and evident in the intestines compared to other tissues.

## 5.9 Limitations and Future Directions

While the use of primary mouse colonoids and monolayers provides a relevant model for studying the intestinal epithelium, it does not fully recapitulate the complex *in vivo* environment of the GI tract. Our model lacks the environmental diversity of the intestines, including immune cells, vasculature, and microbiota, all of which may have a significant role in mediating the effects of MPA. Furthermore, extrapolating our findings to human physiology should be met with caution. Differences in metabolism, immune responses, gene expression, and cell dynamics between mice and humans could lead to unexpected variations[62]. As such, future studies should utilize more physiologically relevant models such as human-derived organoids or human *in vivo* studies. It is also important to mention that our colonoids were derived from male C57BL/6 mice and as such, our data does not discern sex-related differences. Investigating these differences would be valuable given that previous literature has described the presence of variation between males and females regarding MMF toxicity[35].

Our TER and FITC-dextran data was limited in fully characterizing barrier function. Discrepancy between our results suggests that individually, these methods did not capture the full extent of barrier dysfunction. Additionally, our 4 kDa FITC-dextran data did not discern whether the observed changes were due to modulation of the leak pathway or the unrestricted pathway. Future studies should employ the use of larger fluorescent molecules such as 150 kDa FITC-dextran, to distinguish differences between the leak pathway and unrestricted pathway. The exclusive use of ZO-1 and DAPI staining also limited our observations of barrier integrity since other critical tight junction proteins and cytoskeletal components were not visualized. As such, our confocal imaging does not capture the full story of cellular and junctional dynamics. Considering the nuances that may be present, it would be beneficial to include additional tight junction proteins such as claudins and occludins, as well as cytoskeletal staining with phalloidin.

While transcriptomic analysis revealed valuable information regarding the molecular mechanisms behind MPA-induced toxicity, it is important to acknowledge that the data represents a static snapshot of gene expression changes. This data also fails to capture the full spectrum of proteomic or metabolomic alterations that may also contribute to MPA's effects. Future studies should aim to integrate a multi-omics approach to gain a more holistic understanding of the mechanisms driving MPA-induced GI toxicity. Additionally, the effects of MPA were measured at specific time points and as such, the temporal dynamics of MPA-induced toxicity and guanosine supplementation are largely unrepresented. Utilizing tools such as live-cell imaging would improve this aspect. Furthermore, our study did not directly assess cell viability, nucleotide levels, or DNA replication dynamics. Investigating these would provide a more conclusive understanding of MPA-induced effects.

Based on our findings, it would be interesting to evaluate the potential of guanosine supplementation as a therapeutic intervention for patients experiencing significant adverse side effects. At first glance, this approach may seem counterintuitive, given that MPA's efficacy is primarily attributed to guanine nucleotide depletion in lymphocytes. However, available literature provides a nuanced understanding of lymphocyte metabolism, suggesting that lymphocytes rely exclusively on de novo purine biosynthesis, bypassing the salvage pathway[112–116]. The presence of the salvage pathway in the intestinal epithelium but not lymphocytes may represent an effective strategy for mitigation of side effects. Nevertheless, some studies suggest that under certain conditions, lymphocytes may engage the salvage pathway which could potentially interfere with MPA's immunosuppressive effects[117–119]. Given dichotomy of the literature, investigating whether guanosine supplementation can alleviate MPA-induced GI side effects without compromising immunosuppression is both necessary and promising. It is important to note that the safety of guanosine supplementation in humans has not been extensively studied. Most available data is based on animal and *in vitro* models; however, the findings of these studies are encouraging. For instance, guanosine supplementation has been positively implicated in treatment of neuropathic pain, Parkinson's disease, traumatic brain injury, renal ischemic injury, and depression[120–124]. Furthermore, research in mice has shown that chronic guanosine administration does not produce significant toxicity[125]. Based on this data, guanosine appears to be non-toxic while demonstrating a range of potential therapeutic benefits. However, additional studies are necessary to validate safety in humans. Depending on the applicability of guanosine supplementation, a diet of foods rich in nucleic acids, such as mushrooms[126], may provide an interesting avenue for future investigation.

# 6.1 CONCLUSION

This thesis aimed to investigate the mechanisms underlying MPA-induced GI toxicity, marking one of the first investigations of MPA using a colon organoid model. The outcome of this work showcases some significant findings that contribute to our understanding of how MPA induces adverse side effects. In this thesis, a relevant *in vitro* model of GI physiology using primary mouse colonoids was successfully established. The proposed model proved to be effective for studying the impact of MPA on the intestinal epithelium. Our findings demonstrated that MPA exposure leads to significant decreases in TER, indicating modulation of intestinal barrier function. This reduction in TER was corroborated with alterations in tight junction organization, particularly disruption of ZO-1 proteins, and changes in overall epithelial morphology. Furthermore, we identified significant increases in barrier permeability induced by MPA. The presence of dose-dependent relationships was not consistently reflected across all our observations, suggesting complex underlying mechanisms that our data was unable to conclusively measure. Cytokine and chemokine analysis, while not yielding any statistically significant results, provided awareness of the limited immunomodulatory effects of MPA in our employed model. Transcriptomic data further elucidated the molecular pathways affected by MPA, including those involved in cell cycle regulation, DNA replication, and cytoskeleton dynamics. Notably, the inhibition of *de novo* nucleotide metabolism was identified as a key factor in MPA-induced GI toxicity. This led to the conclusion that MPA may provoke a genotoxic effect related to replicative stress, cell cycle arrest, and possible induction of senescence. We also conducted preliminary investigations of guanosine supplementation as a therapeutic intervention to mitigate MPA-induced inhibition. Our results were promising, with

guanosine supplementation effectively preserving TER and promoting recovery of colonoid growth. Together our results suggest that exogenous guanosine may counteract some of the deleterious effects of MPA on the intestinal epithelium. Our conclusions optimistically offer a means to alleviate GI side effects without compromising the immunosuppressive efficacy of MMF. However, the presence of limitations in this thesis provides an opportunity for future exploration of guanosine supplementation in a more clinical setting. A particularly interesting facet of further exploration is the prospect of using a guanosine rich diet for amelioration of MPA-induced GI toxicity. In conclusion, the findings of this thesis demonstrate preliminary avenues for improving patient outcomes and overall tolerability of MMF immunosuppressive therapy.

# 7.1 REFERENCES


1. Altay, G. *et al.* Self-organized intestinal epithelial monolayers in crypt and villus-like domains show effective barrier function. *Sci Rep* **9**, 10140 (2019).
2. Ravi, M., Miller, A. H. & Michopoulos, V. The Immunology of Stress and the Impact of Inflammation on the Brain and Behavior. *BJPsych Adv* **27**, 158–165 (2021).
3. Meneghini, M., Bestard, O. & Grinyo, J. M. Immunosuppressive drugs modes of action. *Best Practice & Research Clinical Gastroenterology* **54–55**, 101757 (2021).
4. Pouliquen, E. *et al.* Recent advances in renal transplantation: antibody-mediated rejection takes center stage. *F1000Prime Rep* **7**, 51 (2015).
5. Larsen, C. P. *et al.* CD40-gp39 INTERACTIONS PLAY A CRITICAL ROLE DURING ALLOGRAFT REJECTION: Suppression of Allograft Rejection by Blockade of the CD40-gp39 Pathway: 1. *Transplantation* **61**, 4 (1996).
6. Duncan, M. D. & Wilkes, D. S. Transplant-related Immunosuppression. *Proc Am Thorac Soc* **2**, 449–455 (2005).
7. Handley, G. & Hand, J. Adverse Effects of Immunosuppression: Infections. in *Pharmacology of Immunosuppression* (ed. Eisen, H. J.) 287–314 (Springer International Publishing, Cham, 2022). doi:10.1007/164_2021_550.
8. Vial, T., Choquet-Kastylevsky, G. & Descotes, J. Adverse effects of immunotherapeutics involving the immune system. *Toxicology* **174**, 3–11 (2002).
9. Noble, J., Terrec, F., Malvezzi, P. & Rostaing, L. Adverse effects of immunosuppression after liver transplantation. *Best Practice & Research Clinical Gastroenterology* **54–55**, 101762 (2021).

10. Opałka, B., Żołnierczuk, M. & Grabowska, M. Immunosuppressive Agents—Effects on the Cardiovascular System and Selected Metabolic Aspects: A Review. *Journal of Clinical Medicine* **12**, 6935 (2023).

11. Rossi, S. J., Schroeder, T. J., Hariharan, S. & Roy First, M. Prevention and Management of the Adverse Effects Associated with Immunosuppressive Therapy. *Drug-Safety* **9**, 104–131 (1993).

12. Szumilas, K. *et al.* Current Status Regarding Immunosuppressive Treatment in Patients after Renal Transplantation. *Int J Mol Sci* **24**, 10301 (2023).

13. Justiz Vaillant, A. A., Misra, S. & Fitzgerald, B. M. Acute Transplantation Rejection. in *StatPearls* (StatPearls Publishing, Treasure Island (FL), 2024).

14. Autoimmune Diseases. *National Institute of Environmental Health Sciences* https://www.niehs.nih.gov/health/topics/conditions/autoimmune.

15. Dorresteijn, E. M. *et al.* Mycophenolate mofetil versus cyclosporine for remission maintenance in nephrotic syndrome. *Pediatr Nephrol* **23**, 2013–2020 (2008).

16. Yashima, Y. & Ohgane, T. [Pharmacological profiles of mycophenolate mofetil (CellCept), a new immunosuppressive agent]. *Nihon Yakurigaku Zasshi* **117**, 131–137 (2001).

17. Allison, A. C. Mechanisms of action of mycophenolate mofetil. *Lupus* (2005) doi:10.1191/0961203305LU2109OA.

18. Behrend, M. Mycophenolate mofetil (Cellcept). *Expert Opinion on Investigational Drugs* **7**, 1509–1519 (1998).

19. Bunnapradist, S. *et al.* Mycophenolate mofetil dose reductions and discontinuations after gastrointestinal complications are associated with renal transplant graft failure. *Transplantation* **82**, 102–107 (2006).

20. Calmet, F. H., Yarur, A. J., Pukazhendhi, G., Ahmad, J. & Bhamidimarri, K. R. Endoscopic and histological features of mycophenolate mofetil colitis in patients after solid organ transplantation. *Ann Gastroenterol* **28**, 366–373 (2015).

21. Liu, T. C., Moore, T. C. & Farraye, F. A. MYCOPHENOLATE MOFETIL (CELLCEPT®) ASSOCIATED ENTEROCOLITIS: 596. *Official journal of the American College of Gastroenterology | ACG* **99**, S193 (2004).

22. Farooqi, R., Kamal, A. & Burke, C. Mycophenolate-induced Colitis: A Case Report with Focused Review of Literature. *Cureus* **12**, e6774.

23. Ducloux, D. *et al.* Mycophenolate mofetil-induced villous atrophy. *Transplantation* **66**, 1115–1116 (1998).

24. Maes, B. D. *et al.* Erosive enterocolitis in mycophenolate mofetil-treated renal-transplant recipients with persistent afebrile diarrhea. *Transplantation* **75**, 665–672 (2003).

25. Boswell, A., Rigg, K. & Shehata, M. Conversion from Mycophenolate Mofetil to Enteric-Coated Mycophenolate Sodium in Patients with Gastrointestinal Side Effects: Case Studies. *Progress in Transplantation* (2006) doi:10.1177/152692480601600208.

26. Taylor, M. R. *et al.* Vancomycin relieves mycophenolate mofetil–induced gastrointestinal toxicity by eliminating gut bacterial β-glucuronidase activity. *Science Advances* **5**, eaax2358 (2019).

27. Flannigan, K. L. *et al.* An intact microbiota is required for the gastrointestinal toxicity of the immunosuppressant mycophenolate mofetil. *The Journal of Heart and Lung Transplantation* **37**, 1047–1059 (2018).

28. Lo, B., Field, M. J. & Institute of Medicine (US) Committee on Conflict of Interest in Medical Research, E. The Pathway from Idea to Regulatory Approval: Examples for Drug Development. in *Conflict of Interest in Medical Research, Education, and Practice* (National Academies Press (US), 2009).

29. Arns, W. Noninfectious Gastrointestinal (GI) Complications of Mycophenolic Acid Therapy: A Consequence of Local GI Toxicity? *Transplantation Proceedings* **39**, 88–93 (2007).

30. Lamba, V. *et al.* PharmGKB summary: mycophenolic acid pathway. *Pharmacogenet Genomics* **24**, 73–79 (2014).

31. Pellock, S. J. & Redinbo, M. R. Glucuronides in the gut: Sugar-driven symbioses between microbe and host. *Journal of Biological Chemistry* **292**, 8569–8576 (2017).

32. Bernard, O. & Guillemette, C. The main role of UGT1A9 in the hepatic metabolism of mycophenolic acid and the effects of naturally occurring variants. *Drug Metab Dispos* **32**, 775–778 (2004).

33. Roberts, M. S., Magnusson, B. M., Burczynski, F. J. & Weiss, M. Enterohepatic Circulation. *Clin Pharmacokinet* **41**, 751–790 (2002).

34. Simpson, J. B. *et al.* Metagenomics combined with activity-based proteomics point to gut bacterial enzymes that reactivate mycophenolate. *Gut Microbes* (2022).

35. Stern, S. T. *et al.* Gender-Related Differences in Mycophenolate Mofetil-Induced Gastrointestinal Toxicity in Rats. *Drug Metab Dispos* **35**, 449–454 (2007).

36. Smith, M. R. & Cooper, S. C. Mycophenolate mofetil therapy in the management of inflammatory bowel disease — A retrospective case series and review. *Journal of Crohn's and Colitis* **8**, 890–897 (2014).

37. Bull, M. J. & Plummer, N. T. Part 1: The Human Gut Microbiome in Health and Disease. *Integr Med (Encinitas)* **13**, 17–22 (2014).

38. Behrend, M. & Braun, F. Enteric-coated mycophenolate sodium: tolerability profile compared with mycophenolate mofetil. *Drugs* **65**, 1037–1050 (2005).

39. Kobashigawa, J. A. *et al.* Twelve months results of Enteric-Coated Mycophenolate Sodium (EC-MPS) in de novo heart transplant patients showed excellent efficacy and safety. *The Journal of heart*

*and lung transplantation : the official publication of the International Society for Heart Transplantation* **24**, (2005).

40. Morris, C. C., Gregoire, S. A., Juneman, E. B., Golconda, U. & Stroud, S. C. Orthotopic Heart Transplant Recipient with Enteric-coated Mycophenolate Sodium (Myfortic) Induced Colitis. *The American Journal of Case Reports* **21**, (2020).

41. Knoll, G. A., MacDonald, I., Khan, A. & van Walraven, C. Mycophenolate Mofetil Dose Reduction and the Risk of Acute Rejection after Renal Transplantation. *Journal of the American Society of Nephrology* **14**, 2381 (2003).

42. Dalal, P., Shah, G., Chhabra, D. & Gallon, L. Role of tacrolimus combination therapy with mycophenolate mofetil in the prevention of organ rejection in kidney transplant patients. *Int J Nephrol Renovasc Dis* **3**, 107–115 (2010).

43. Klawitter, J. *et al.* Mycophenolate Mofetil Enhances the Negative Effects of Sirolimus and Tacrolimus on Rat Kidney Cell Metabolism. *PLOS ONE* **9**, e86202 (2014).

44. van Gelder, T. *et al.* Therapeutic Drug Monitoring of Mycophenolate Mofetil in Transplantation. *Therapeutic Drug Monitoring* **28**, 145 (2006).

45. Meur, Y. L. *et al.* Individualized Mycophenolate Mofetil Dosing Based on Drug Exposure Significantly Improves Patient Outcomes After Renal Transplantation. *American Journal of Transplantation* **7**, 2496–2503 (2007).

46. Arns, W. *et al.* Therapeutic Drug Monitoring of Mycophenolic Acid in Solid Organ Transplant Patients Treated With Mycophenolate Mofetil: Review of the Literature. *TRANSPLANTATION* **82**, (2006).

47. Kaplan, B. Mycophenolic acid trough level monitoring in solid organ transplant recipients treated with mycophenolate mofetil: association with clinical outcome. *Current medical research and opinion* **22**, (2006).

48. Paulo, A. Z., Amancio, O. M. S., de Morais, M. B. & Tabacow, K. M. M. D. Low-dietary fiber intake as a risk factor for recurrent abdominal pain in children. *Eur J Clin Nutr* **60**, 823–827 (2006).

49. Bosaeus, I. Fibre effects on intestinal functions (diarrhoea, constipation and irritable bowel syndrome). *Clinical Nutrition Supplements* **1**, 33–38 (2004).

50. Zhu, L. *et al.* Probiotic yogurt regulates gut microbiota homeostasis and alleviates hepatic steatosis and liver injury induced by high-fat diet in golden hamsters. *Food Science & Nutrition* **12**, 2488–2501 (2024).

51. Marks, W. H., Spinelli, T. Y. & Olmstead, S. F. REDUCTION OF IMMUNOSUPPRESSION-ASSOCIATED DIARRHEA BY PROBIOTICS FOLLOWING RENAL TRANSPLANTATION: 1226. *Transplantation* **90**, 441 (2010).

52. Khan, N., Binder, L., Pantakani, D. V. K. & Asif, A. R. MPA Modulates Tight Junctions' Permeability via Midkine/PI3K Pathway in Caco-2 Cells: A Possible Mechanism of Leak-Flux Diarrhea in Organ Transplanted Patients. *Front. Physiol.* **8**, (2017).

53. Qasim, M., Rahman, H., Ahmed, R., Oellerich, M. & Asif, A. R. Mycophenolic acid mediated disruption of the intestinal epithelial tight junctions. *Experimental Cell Research* **322**, 277–289 (2014).

54. Deng, Y. *et al.* Mycophenolic Acid Induces the Intestinal Epithelial Barrier Damage through Mitochondrial ROS. *Oxid Med Cell Longev* **2022**, 4195699 (2022).

55. Natoli, M., Leoni, B. D., D'Agnano, I., Zucco, F. & Felsani, A. Good Caco-2 cell culture practices. *Toxicology in Vitro* **26**, 1243–1246 (2012).

56. Frontiers Editorial Office. Retraction: Immunosuppressant MPA Modulates Tight Junction through Epigenetic Activation of MLCK/MLC-2 Pathway via p38MAPK. *Front. Physiol.* **8**, (2017).

57. Lopez-Escalera, S. & Wellejus, A. Evaluation of Caco-2 and human intestinal epithelial cells as in vitro models of colonic and small intestinal integrity. *Biochem Biophys Rep* **31**, 101314 (2022).

58. Lea, T. Caco-2 Cell Line. in *The Impact of Food Bioactives on Health: in vitro and ex vivo models* (eds. Verhoeckx, K. et al.) (Springer, Cham (CH), 2015).

59. Sollinger, H. W. From mice to man: the preclinical history of mycophenolate mofetil. *Clin Transplant* **10**, 85–92 (1996).

60. Alby-Laurent, F. *et al.* Low-dose mycophenolate mofetil improves survival in a murine model of Staphylococcus aureus sepsis by increasing bacterial clearance and phagocyte function. *Front. Immunol.* **13**, (2022).

61. Huang, S.-W. *et al.* Mycophenolate Mofetil Protects Septic Mice via the Dual Inhibition of Inflammatory Cytokines and PD-1. *Inflammation* **41**, 1008–1020 (2018).

62. Lampreht Tratar, U., Horvat, S. & Cemazar, M. Transgenic Mouse Models in Cancer Research. *Front. Oncol.* **8**, (2018).

63. Heischmann, S., Dzieciatkowska, M., Hansen, K., Leibfritz, D. & Christians, U. The Immunosuppressant Mycophenolic Acid Alters Nucleotide and Lipid Metabolism in an Intestinal Cell Model. *Sci Rep* **7**, 45088 (2017).

64. Edmondson, R., Broglie, J. J., Adcock, A. F. & Yang, L. Three-Dimensional Cell Culture Systems and Their Applications in Drug Discovery and Cell-Based Biosensors. *Assay Drug Dev Technol* **12**, 207–218 (2014).

65. Duval, K. *et al.* Modeling Physiological Events in 2D vs. 3D Cell Culture. *Physiology (Bethesda)* **32**, 266–277 (2017).

66. Simian, M. & Bissell, M. J. Organoids: A historical perspective of thinking in three dimensions. *J Cell Biol* **216**, 31–40 (2017).

67. Li, Y., Tang, P., Cai, S., Peng, J. & Hua, G. Organoid based personalized medicine: from bench to bedside. *Cell Regen* **9**, 21 (2020).

68. Barker, N. *et al.* Identification of stem cells in small intestine and colon by marker gene Lgr5. *Nature* **449**, 1003–1007 (2007).

69. Sato, T. *et al.* Long-term Expansion of Epithelial Organoids From Human Colon, Adenoma, Adenocarcinoma, and Barrett's Epithelium. *Gastroenterology* **141**, 1762–1772 (2011).

70. Yoo, J.-H. & Donowitz, M. Intestinal enteroids/organoids: A novel platform for drug discovery in inflammatory bowel diseases. *World J Gastroenterol* **25**, 4125–4147 (2019).

71. In, J. G., Foulke-Abel, J., Clarke, E. & Kovbasnjuk, O. Human Colonoid Monolayers to Study Interactions Between Pathogens, Commensals, and Host Intestinal Epithelium. *J Vis Exp* 10.3791/59357 (2019) doi:10.3791/59357.

72. Leslie, J. L. *et al.* Persistence and Toxin Production by Clostridium difficile within Human Intestinal Organoids Result in Disruption of Epithelial Paracellular Barrier Function. *Infect Immun* **83**, 138–145 (2015).

73. Foulke-Abel, J. *et al.* Human Enteroids as a Model of Upper Small Intestinal Ion Transport Physiology and Pathophysiology. *Gastroenterology* **150**, 638-649.e8 (2016).

74. Wang, Y. *et al.* Self-renewing Monolayer of Primary Colonic or Rectal Epithelial Cells. *Cell Mol Gastroenterol Hepatol* **4**, 165-182.e7 (2017).

75. Varani, J., McClintock, S. D. & Aslam, M. N. Organoid culture to study epithelial cell differentiation and barrier formation in the colon: bridging the gap between monolayer cell culture and human subject research. *In Vitro Cell Dev Biol Anim* **57**, 174–190 (2021).

76. Barnett, A. M., Mullaney, J. A., McNabb, W. C. & Roy, N. C. Culture media and format alter cellular composition and barrier integrity of porcine colonoid-derived monolayers. *Tissue Barriers* **12**, 2222632 (2024).

77. Fernando, E. H. *et al.* A simple, cost-effective method for generating murine colonic 3D enteroids and 2D monolayers for studies of primary epithelial cell function. *Am J Physiol Gastrointest Liver Physiol* **313**, G467–G475 (2017).

78. Corrò, C., Novellasdemunt, L. & Li, V. S. W. A brief history of organoids. *Am J Physiol Cell Physiol* **319**, C151–C165 (2020).

79. van Dooremalen, W. T. M. *et al.* Organoid-Derived Epithelial Monolayer: A Clinically Relevant In Vitro Model for Intestinal Barrier Function. *J Vis Exp* (2021) doi:10.3791/62074.

80. Almeqdadi, M., Mana, M. D., Roper, J. & Yilmaz, Ö. H. Gut organoids: mini-tissues in culture to study intestinal physiology and disease. *Am J Physiol Cell Physiol* **317**, C405–C419 (2019).

81. Babraham Bioinformatics - FastQC A Quality Control tool for High Throughput Sequence Data. https://www.bioinformatics.babraham.ac.uk/projects/fastqc/.

82. Wilson, S. S. *et al.* Optimized Culture Conditions for Improved Growth and Functional Differentiation of Mouse and Human Colon Organoids. *Front. Immunol.* **11**, (2021).

83. Shen, L., Weber, C. R., Raleigh, D. R., Yu, D. & Turner, J. R. Tight Junction Pore and Leak Pathways: A Dynamic Duo. *Annu Rev Physiol* **73**, 283–309 (2011).

84. Horowitz, A., Chanez-Paredes, S. D., Haest, X. & Turner, J. R. Paracellular permeability and tight junction regulation in gut health and disease. *Nat Rev Gastroenterol Hepatol* **20**, 417–432 (2023).

85. Song, Y. *et al.* Keratinocyte growth factor ameliorates mycophenolate mofetil-induced intestinal barrier disruption in mice. *Molecular Immunology* **124**, 61–69 (2020).

86. Arango Duque, G. & Descoteaux, A. Macrophage Cytokines: Involvement in Immunity and Infectious Diseases. *Front Immunol* **5**, 491 (2014).

87. Do, B. T. *et al.* Nucleotide depletion promotes cell fate transitions by inducing DNA replication stress. *Developmental Cell* (2024) doi:10.1016/j.devcel.2024.05.010.

88. Herr, L. M., Schaffer, E. D., Fuchs, K. F., Datta, A. & Brosh, R. M. Replication stress as a driver of cellular senescence and aging. *Commun Biol* **7**, 1–19 (2024).

89. Dong, L., Lyu, X., Faleti, O. D. & He, M.-L. The special stemness functions of Tbx3 in stem cells and cancer development. *Seminars in Cancer Biology* **57**, 105–110 (2019).

90. Zona, S., Bella, L., Burton, M. J., Nestal de Moraes, G. & Lam, E. W.-F. FOXM1: an emerging master regulator of DNA damage response and genotoxic agent resistance. *Biochim Biophys Acta* **1839**, 1316–1322 (2014).

91. Hou, Y. *et al.* The transcription factor Foxm1 is essential for the quiescence and maintenance of hematopoietic stem cells. *Nat Immunol* **16**, 810–818 (2015).

92. Lu, Q., Longo, F. M., Zhou, H., Massa, S. M. & Chen, Y.-H. Signaling Through Rho GTPase Pathway as Viable Drug Target. *Curr Med Chem* **16**, 1355–1365 (2009).

93. López-Posadas, R., Stürzl, M., Atreya, I., Neurath, M. F. & Britzen-Laurent, N. Interplay of GTPases and Cytoskeleton in Cellular Barrier Defects during Gut Inflammation. *Front. Immunol.* **8**, (2017).

94. Mijit, M., Caracciolo, V., Melillo, A., Amicarelli, F. & Giordano, A. Role of p53 in the Regulation of Cellular Senescence. *Biomolecules* **10**, 420 (2020).

95. Drullion, C. *et al.* Mycophenolic Acid Overcomes Imatinib and Nilotinib Resistance of Chronic Myeloid Leukemia Cells by Apoptosis or a Senescent-Like Cell Cycle Arrest. *Leukemia Research and Treatment* **2012**, 861301 (2012).

96. Cohn, R. G. *et al.* MYCOPHENOLIC ACID INCREASES APOPTOSIS, LYSOSOMES AND LIPID DROPLETS IN HUMAN LYMPHOID AND MONOCYTIC CELL LINES. *Transplantation* **68**, 411 (1999).

97. Tran, D. H. *et al.* De novo and salvage purine synthesis pathways across tissues and tumors. *Cell* **187**, 3602-3618.e20 (2024).

98. Lukášová, E. *et al.* Distinct cellular responses to replication stress leading to apoptosis or senescence. *FEBS Open Bio* **9**, 870–890 (2019).

99. Eugui, E. M., Mirkovich, A. & Allison, A. C. Lymphocyte-selective antiproliferative and immunosuppressive effects of mycophenolic acid in mice. *Scand J Immunol* **33**, 175–183 (1991).

100. Allison, A. C. & Eugui, E. M. Mycophenolate mofetil and its mechanisms of action. *Immunopharmacology* **47**, 85–118 (2000).

101. Prémaud, A. *et al.* Inhibition of T-cell activation and proliferation by mycophenolic acid in patients awaiting liver transplantation: PK/PD relationships. *Pharmacological Research* **63**, 432–438 (2011).

102. Heinschink, A., Raab, M., Daxecker, H., Griesmacher, A. & Müller, M. M. In vitro effects of mycophenolic acid on cell cycle and activation of human lymphocytes. *Clinica Chimica Acta* **300**, 23–28 (2000).

103. Yam, P. *et al.* Ex vivo selection and expansion of cells based on expression of a mutated inosine monophosphate dehydrogenase 2 after HIV vector transduction: effects on lymphocytes, monocytes, and CD34+ stem cells. *Mol Ther* **14**, 236–244 (2006).

104. Collins, K. S. *et al.* Interindividual Variability in Lymphocyte Stimulation and Transcriptomic Response Predicts Mycophenolic Acid Sensitivity in Healthy Volunteers. *Clinical and Translational Science* **13**, 1137–1149 (2020).

105. Winnicki, W. *et al.* An inosine 5'-monophosphate dehydrogenase 2 single-nucleotide polymorphism impairs the effect of mycophenolic acid. *Pharmacogenomics J* **10**, 70–76 (2010).

106. Bremer, S. *et al.* Expression of IMPDH1 and IMPDH2 After Transplantation and Initiation of Immunosuppression. *Transplantation* **85**, 55 (2008).

107. Carr, S. F., Papp, E., Wu, J. C. & Natsumeda, Y. Characterization of human type I and type II IMP dehydrogenases. *J Biol Chem* **268**, 27286–27290 (1993).

108. Hedstrom, L. IMP Dehydrogenase: Structure, Mechanism and Inhibition. *Chem Rev* **109**, 2903–2928 (2009).

109. Chaiyawat, P. *et al.* IMPDH2 and HPRT expression and a prognostic significance in preoperative and postoperative patients with osteosarcoma. *Sci Rep* **11**, 10887 (2021).

110. Senda, M. & Natsumeda, Y. Tissue-differential expression of two distinct genes for human IMP dehydrogenase (E.C.1.1.1.205). *Life Sciences* **54**, 1917–1926 (1994).

111. Kaunitz, J. D. & Akiba, Y. Control of Intestinal Epithelial Proliferation and Differentiation: The Microbiome, Enteroendocrine L Cells, Telocytes, Enteric Nerves, and GLP, Too. *Dig Dis Sci* **64**, 2709–2716 (2019).

112. Karnell, J. L. *et al.* Mycophenolic Acid Differentially Impacts B Cell Function Depending on the Stage of Differentiation. *J Immunol* **187**, 3603–3612 (2011).

113. Hussain, Y. & Khan, H. Immunosuppressive Drugs. *Encyclopedia of Infection and Immunity* 726–740 (2022) doi:10.1016/B978-0-12-818731-9.00068-9.

114. Allison, A. C., Hovi, T., Watts, R. W. & Webster, A. D. The role of de novo purine synthesis in lymphocyte transformation. *Ciba Found Symp* 207–224 (1977) doi:10.1002/9780470720301.ch13.

115. Sintchak, M. D. *et al.* Structure and Mechanism of Inosine Monophosphate Dehydrogenase in Complex with the Immunosuppressant Mycophenolic Acid. *Cell* **85**, 921–930 (1996).

116. Rath, T., Küpper, M., Rath, T. & Küpper, M. Pharmacokinetics and Pharmacodynamics of Mycophenolate in Patients After Renal Transplantation. in *Renal Transplantation - Updates and Advances* (IntechOpen, 2012). doi:10.5772/26647.

117. Toy, G. *et al.* Requirement for deoxycytidine kinase in T and B lymphocyte development. *Proceedings of the National Academy of Sciences* **107**, 5551–5556 (2010).

118. Choi, O. *et al.* A Deficiency in Nucleoside Salvage Impairs Murine Lymphocyte Development, Homeostasis, and Survival. *The Journal of Immunology* **188**, 3920–3927 (2012).

119. Cohen, A., Barankiewicz, J., Lederman, H. M. & Gelfand, E. W. Purine metabolism in human T lymphocytes: role of the purine nucleoside cycle. *Can. J. Biochem. Cell Biol.* **62**, 577–583 (1984).

120. Bettio, L. E. B., Gil-Mohapel, J. & Rodrigues, A. L. S. Current perspectives on the antidepressant-like effects of guanosine. *Neural Regen Res* **11**, 1411–1413 (2016).

121. Schmidt, A. P. *et al.* Guanosine Prevents Thermal Hyperalgesia in a Rat Model of Peripheral Mononeuropathy. *The Journal of Pain* **11**, 131–141 (2010).

122. Massari, C. M. *et al.* Antiparkinsonian Efficacy of Guanosine in Rodent Models of Movement Disorder. *Front. Pharmacol.* **8**, (2017).

123. Gerbatin, R. da R. *et al.* Guanosine Protects Against Traumatic Brain Injury-Induced Functional Impairments and Neuronal Loss by Modulating Excitotoxicity, Mitochondrial Dysfunction, and Inflammation. *Mol Neurobiol* **54**, 7585–7596 (2017).

124. Kelly, K. J., Plotkin, Z. & Dagher, P. C. Guanosine supplementation reduces apoptosis and protects renal function in the setting of ischemic injury. *J Clin Invest* **108**, 1291–1298 (2001).

125. Regina Vinadé, E. *et al.* Chronically administered guanosine is anticonvulsant, amnesic and anxiolytic in mice. *Brain Research* **977**, 97–102 (2003).

126. Phan, C.-W. *et al.* A review on the nucleic acid constituents in mushrooms: nucleobases, nucleosides and nucleotides. *Crit Rev Biotechnol* **38**, 762–777 (2018).